

UNIVERSITÀ DEGLI STUDI DI TRENTO



DEPARTMENT OF PHYSICS
Ph.D. Thesis in Physics

**Spin polarization effects
in neutron stars**

Supervisor:
Prof. Francesco Pederiva

Candidate:
Luca Riz
XXXII Cycle

March 9, 2020

The important thing is not to stop questioning.
Curiosity has its own reason for existence.

— Albert Einstein —

CONTENTS

LIST OF FIGURES	vii
INTRODUCTION	1
1 NEUTRON STARS AND MAGNETARS	5
1.1 Neutron stars structure	6
1.2 Neutron stars: observations and phenomenology	8
1.3 Magnetars	21
2 NUCLEON-NUCLEON INTERACTION	25
2.1 Phenomenological potential	26
2.1.1 Three-body forces	28
2.2 Local chiral effective field theory potential	30
3 COMPUTATIONAL METHODS	39
3.1 Quantum Monte Carlo methods	40
3.1.1 Variational Monte Carlo (VMC)	41
3.1.2 Auxiliary field diffusion Monte Carlo (AFDMC)	43
3.2 Infinite matter and boundary conditions	46
3.3 Time dependent local spin density approximation	51
3.3.1 Longitudinal channel	52
3.3.2 Transverse channel	57
4 RESULTS	59
4.1 Equation of state	59
4.1.1 Effective mass	65
4.2 Response functions	67
4.3 Neutrino mean free path	73

CONTENTS

4.4	Compressibility	79
4.5	Magnetic susceptibility	83
4.5.1	Spin-symmetry energy	95
5	CONCLUSIONS	97
	BIBLIOGRAPHY	99

LIST OF FIGURES

Figure 1.1	Neutron star structure and composition.	7
Figure 1.2	Measured NS masses.	9
Figure 1.3	Schematic EOS and M-R relation.	11
Figure 1.4	M-R curves for different EOS	13
Figure 1.5	QMC $npe\mu$ model.	14
Figure 1.6	PNM with hyperons.	15
Figure 1.7	Symmetry energy E_{sym} and slope L_0	16
Figure 1.8	Tidal deformability $\tilde{\Lambda}$ as a function of R	18
Figure 1.9	Tidal deformability $\tilde{\Lambda}$ as a function of L_0 and E_{sym}	20
Figure 1.10	Magnetars distribution in magnetic field.	22
Figure 1.11	Magnetic fields models.	23
Figure 1.12	Intensity of outer core magnetic fields.	24
Figure 2.1	AV8' phase shifts	27
Figure 2.2	NNN Feynman diagrams	29
Figure 2.3	EOS for PNM: phenomenological potentials	30
Figure 2.4	Chiral EFT Feynman diagrams	32
Figure 2.5	Local chiral EFT phase shifts	35
Figure 2.6	EOS for PNM: local chiral EFT potentials	36
Figure 2.7	EOS for PNM: phenomenological and local chiral EFT po- tentials	37
Figure 3.1	Unconstrained AFDMC	45
Figure 3.2	Momentum distribution for 2D spinless fermionic system . .	47
Figure 3.3	Energy contribution of twist angle for a 2D spin 1/2 non- interacting fermionic system	48
Figure 3.4	Energy per particle for 3D non interacting fermionic system: PBC vs TABC	49

List of Figures

Figure 3.5	Energy per particle for PNM with TABC	50
Figure 4.1	EOS for PNM and SPPNM	60
Figure 4.2	Estimate of theoretical uncertainties for chiral EFT.	62
Figure 4.3	Diffusion coefficients of DMC	66
Figure 4.4	Longitudinal response function for $\xi = 0.2$	69
Figure 4.5	Longitudinal response function for PNM ($\xi = 0.0$)	70
Figure 4.6	Transverse response function at low spin polarization ($z = 6$)	71
Figure 4.7	Integration region of q and ω	74
Figure 4.8	Neutrino mean free path ratio with respect to the free Fermi gas	75
Figure 4.9	Neutrino mean free path ratio with respect to the free Fermi gas: comparison with literature's results.	76
Figure 4.14	Free Fermi gas energy per particle as a function of the ex- ternal magnetic field b	83
Figure 4.15	Ground state energy with $b = 0$ MeV as a function of ξ	86
Figure 4.16	Ground state energy at fixed J_z as a function of b	86
Figure 4.17	Ground state energy with $b = 20$ MeV as a function of ξ	87
Figure 4.18	Ground state spin polarization as a function of external magnetic field - non-interacting system	89
Figure 4.19	χ/χ_F at saturation density	90
Figure 4.20	Ground state spin polarization as a function of external magnetic field - interacting system	91
Figure 4.21	Magnetic susceptibility as a function of the density: ap- proach (i) vs. approach (ii)	92
Figure 4.22	Magnetic susceptibility as a function of the density: ap- proach (ii) vs. Fermi gas	93
Figure 4.23	Magnetic susceptibility ratio with respect to the free Fermi gas: comparison with literature's results	94
Figure 4.24	Spin-symmetry energy	95

Figure 4.25 Magnetic susceptibility as a function of the density: approach (ii) vs. spin-symmetry energy 96

ABSTRACT

This thesis is concerned with effects of spin polarization in neutron stars. In particular, we focus on static and dynamic properties of dense neutron matter. We use two different kind of potential to perform our studies: the phenomenological two-body Argonne V8' potential plus the three-body Urbana IX force and a modern local version of chiral effective potential up to next-to-next-to-leading order (N²LO).

Estimates are calculated for the neutrino mean free path in partially spin-polarized neutron matter starting from Quantum Monte Carlo (QMC) simulations and using mean-field approaches to compute the response function in the longitudinal and transverse channel. We also compute magnetic susceptibility of dense neutron matter from accurate QMC calculations of partially spin-polarized systems. Twist-averaged boundary conditions (TABC) have been implemented to reduce finite-size effects. In the results, we also account for the theoretical uncertainty coming from the chiral expansion scheme.

These results may play a role in studying high-energy phenomena such as neutron star mergers and supernova explosions, although they have been computed only at $T=0$ K.

INTRODUCTION

Matter under extreme conditions has always been a challenge to test theories in physics. To this extent, neutron stars are unique laboratories to test physics from gravitational to nuclear theories, but also weak processes. Neutron stars (NS) have a radius of $\sim 10 - 13$ km, and masses varying from $1.2 - 2.2$ solar masses (M_{\odot}).

The equation of state (EOS) is the relation between pressure and density, and it is the key ingredient to describe neutron stars. In fact, for a given EOS, Tolman-Oppenheimer-Volkov (TOV) equations, describing the structure of a non-rotating star, can be solved. The results are mass-radius (M-R) relations, which can be directly compared to neutron stars observations. Different models of nuclear interactions and theoretical approaches give different EOS. One strict constraint on the EOS is that they need to reproduce the maximum measured mass of NS. The maximum measured mass is $2.14^{+0.10}_{-0.09} M_{\odot}$ [1]. Direct and indirect mass measurements are quite accurate, while radii can not be precisely measured (both directly and indirectly). Only some interactions are ruled out in this analysis.

New interest in the field was sparked by the first detection of gravitational waves (GW) on September 14, 2015 (GW) from a black-hole merger event [2]. A. Einstein already predicted gravitational waves in the formulation of general relativity in 1916 [3], but he already understood that they would have been weak. The weakness of the signal required ~ 100 years to detect and measure GW signals. Not only black holes but also NS mergers generate sufficiently strong gravitational waves that could be detected. Indeed one binary neutron star merger has been detected on August 17, 2017 (GW170817) [4], and a second a NS merger observation has recently been announced [5]. Gravitational waves detection of NS mergers might put new constraints on the equation of state (EOS), especially at densities beyond saturation. New observations are expected, and some candidates of

binary NS have been announced in the third run of LIGO-Virgo collaboration observation, and details of one observation have recently been released.

The possibility of describing matter at densities up to $\sim 5 - 10$ times the saturation density $\rho_0 = 0.16 \text{ fm}^{-3}$ by means of non relativistic interacting hadrons is still questionable. Nuclear interactions employed in conventional nuclear physics are based on reliable experimental data on atomic nuclei and nucleon scattering. No experimental data are available at such high densities and can not be obtained from terrestrial experiments. The description of matter at such high densities is still an open question, and only different models can be proposed. Some theories hypothesize the transition to quark matter, other the onset of pion or kaon condensates or after some critical densities, the onset of strange baryons.

A last aspect is the huge surface magnetic fields that have been measured in some neutron stars. Due to their nature of neutron stars with high magnetic fields, they have been called magnetars. Magnetic effects on matter in magnetars interiors are mostly unknown, since a precise determination of the magnetic field is extremely difficult. This even more exotic state of matter is the main topic of this work.

The present work is organized as follows:

In **Chapter 1** we briefly present the structure of neutron stars, we give an overview of theoretical efforts to describe NS and the state-of-the-art experimental observations. In the last part we introduce magnetars.

In **Chapter 2** nucleon-nucleon interactions are presented. In particular phenomenological Argonne V8' (AV8') with Urbana IX (UIX) three-body force and local chiral effective field theory potentials (EFT) up to next-to-next-to-leading-order (N2LO) are discussed.

In **Chapter 3** quantum Monte Carlo (QMC) methods used to compute ground state properties are introduced. Modeling of infinite matter is discussed, focusing on the problem of boundary conditions. We introduce mean-field approximation, namely time-dependent local spin density approximation (TDLSDA), to study excited states since at the moment we can only partially treat excited states within QMC.

In **Chapter 4** we present the results of partially spin-polarized neutron mat-

ter. We computed EOS, magnetic susceptibility, and compressibility using QMC methods. The calculations of the response functions and the evaluation of the neutrino mean free path (NMFP) are performed within TDLSDA.

In **Chapter 5** the conclusions and future developments of our work are discussed.

NEUTRON STARS AND MAGNETARS

*I*n the first part of this chapter, we give a brief overview of the history of neutron stars, from prediction to discovery. Neutron stars were first hypothesized theoretically by W. Baade and F. Zwicky in 1933 [6, 7] to explain the energy release in the observations of supernova explosions. As the name suggests, neutron stars are mainly made by neutrons. Neutron was discovered just a year earlier by J. Chadwick [8, 9]. Another important step towards the understanding of these theoretical objects was independently made by R.C. Tolman [10], and J.R. Oppenheimer, and G.M. Volkov [11] in 1939. They derived general relativistic equations of hydrostatic equilibrium for a spherically symmetric distribution of matter. In the simple model of non-interacting strongly degenerate relativistic neutrons, they obtained a maximum (gravitational) mass of $0.71 M_{\odot}$ for a static neutron star. Theorists developed different models over the years to describe neutron stars, including the equation of state (EOS) for dense matter, superfluidity in neutron star crust, and neutrino emissions from neutron stars. The inclusion of nuclear forces gave rise to stiffer EOS, and the new predicted maximum mass increased up to $\sim 2.0 M_{\odot}$.

The first empirical observation of NS was due to J. Bell, a graduate student supervised by A. Hewish, who discovered a weak variable radio source in 1967. The measure of the period of the periodic pulses led to the idea of an artificial signal. Indeed their first denomination was LGM (Little Green Men) due to the incredible stability of their period. After this first discovery of rapidly pulsating source, the pulsar, many other pulsars were discovered and observed. In 1968 Gold described the origin of pulsars as rotating magnetized neutron stars, ruling out the

previous models of stellar oscillations (either neutron stars or white dwarfs). We now describe the current theoretical models of the structure of neutron stars and their relations to observations.

1.1 NEUTRON STARS STRUCTURE

Neutron stars are the densest stars in the universe. They have a radius of $\sim 10 - 13$ km, and masses varying from $1.2 - 2.2$ solar masses (M_{\odot}). Neutron stars can be divided into four main internal regions: outer crust, inner crust, outer core, and inner core, as shown in Figure 1.1.

Each region has its specific composition and properties. From the outer layer to the interior the density increases up to $\sim 5 - 10$ times nuclear saturation density ($\rho_0 = 2.67 \times 10^{14}$ g/cm³ = 0.16 fm⁻³).

Atmosphere. An external thin hot plasma layer where thermal radiation is emitted. Surface temperature, magnetic field, and chemical composition are fundamental ingredients that can be extracted from the thermal radiation. Reliable theoretical models of the thermal radiation are needed to interpret observation of the thermal component and infer radius and mass of the neutron star.

Outer crust. This layer is a few hundred meters thick, and it is composed of ionized atoms and free electrons. It extends from the atmosphere up to the neutron-drip density ($\rho = \rho_{\text{ND}} \approx 4 \times 10^{11}$ g/cm³). Beta captures are favored increasing density, and neutron-rich nuclei are formed in the deeper layers.

Inner crust. It is a 1-2 km deep and very dense layer of neutron-rich nuclei and free electrons. The densities ranges from ρ_{ND} up to $\sim 0.5\rho_0$. At these densities, we have a transition to lower dimensionality of matter from three-dimensional (3D) to one-dimensional (1D) before an eventual transition to uniform nucleonic matter. This series of transitions is known as nuclear pasta. The neutron fluid of the crust could probably form a superfluid.

Outer core. The core (inner and outer) constitutes the main part of the neutron star. It is ~ 9 km deep and constitutes up to 99% of the mass of the star. The density range of the outer part is from $0.5\rho_0$ to $2\rho_0$, and this layer is several kilometers

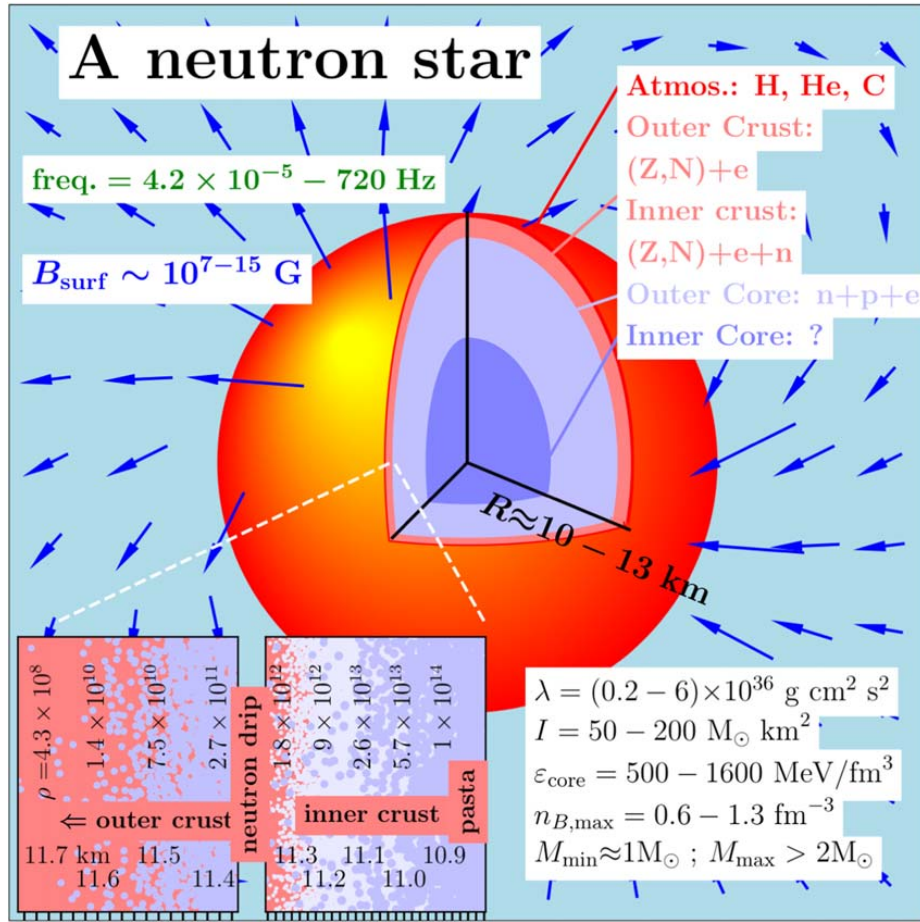


Figure 1.1: A summary of the microphysics of neutron stars. In the upper left of the figure, the observational limits on rotation frequency [12, 13] and the magnetic field [14, 15] are given. The upper right panel shows the composition of the various layers. The lower left shows a schematic representation of the crust, where the dark blue color represents nuclei, and the light blue color represents free neutrons. The limits on the radius from x-ray observations are shown near the center [16]. Limits on the tidal deformability, moment of inertia, energy density in the core, and baryon density in the core [17] are shown in the lower right panel (from Ref. [18]).

thick. Matter is composed of nucleons, electrons, and muons (the so-called $npe\mu$ composition). The fraction of protons in this region is small compared to that of neutrons ($\lesssim 10\%$).

Inner core. This region is still an open question. Central densities can reach

$\sim 5 - 10$ times nuclear saturation density. Different hypothesis have been formulated for matter at such high densities: onset of hyperons (starting with Σ^- and Λ), pion (π) or kaon (K) condensation, or a phase transition to quark matter. Another hypothetical class of compact stars is strange quark matter (SQM) stars. In this model, quark matter has just up, down, strange quarks, since charm, top, and bottom quarks are too massive to appear. Their existence relies on the conjecture that the absolute ground state of hadronic matter is quark matter.

1.2 NEUTRON STARS: OBSERVATIONS AND PHENOMENOLOGY

In the first part of this section, we review state-of-the-art mass and radii observations, while the second part is devoted to the connection between gravitational waves observations and the equation of state.

Mass measurements. Currently, precise measurements of NS masses rely on the tracking of the orbital motions. Although around 2500 pulsars are known [19], only 10% are in binary systems that can be measured, while isolated neutron stars can not. The arrival times of the pulsation are measured to precisely infer the mass of the neutron star. Within Newtonian gravity, the orbital motion is described by five Keplerian parameters. They can be obtained by fitting some models to observations of spin periods. The five Keplerian parameters, which describe orbital motion in Newtonian gravity, are not sufficient to derive the mass of the NS. Since binary pulsars are compact systems, general relativistic effects can be observed. The measure of at least two relativistic effects is needed to determine the measure of the NS mass. Only for a few systems these effects can be precisely measured. In other cases, empirical relations between binary period and mass of the companion or optical detection of the companion or other approaches to restrict the physical parameters of the pulsar are used to derive the NS mass. Figure 1.2 is a summary of NS observation up to 2012. New observations regarding the maximum measured mass of NS are discussed below.

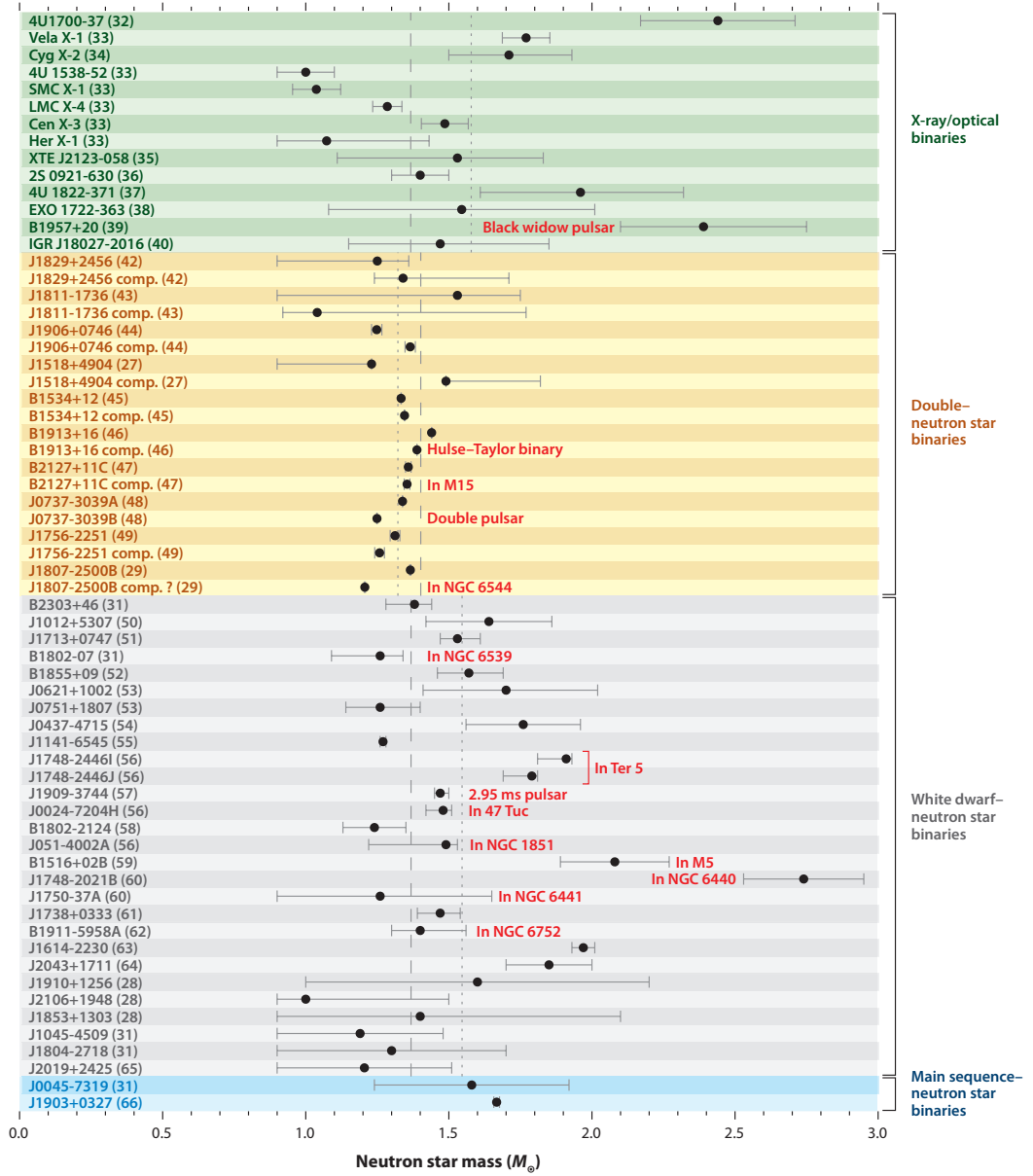


Figure 1.2: Measured neutron star masses with 1- σ errors (from Ref. [20]). References in parentheses following source names refer to the bibliography of Ref. [20].

Radius measurements. The most reliable estimates of NS radii are derived from observations of thermal emissions from the surface of the star (either spectroscopic or timing approaches). The extracted value is the so-called radiation radius $R_{\infty} = R(1 - 2GM/Rc)^{-1/2}$. Despite many efforts, uncertainties coming from these methods are quite significant.

There are no precise simultaneous measurements of mass and radius for any neutron star from experiments.

One recent result of the NICER mission provides the most precise measure of the radius of a neutron star so far. The pulsar PSR J0030+0451 has an inferred mass of $1.34_{-0.16}^{+0.15}M_{\odot}$ and an equatorial radius of $12.71_{-1.19}^{+1.14}$ km [21, 22, 23]. These uncertainties on the radius measurement are still quite significant to provide useful constraints of the EOS and on the nuclear microphysics. As we will see below, more precise measurements on the radius of the NS would provide a significant improvement on the different nuclear EOS (see Figure 1.4).

The theoretical nuclear key ingredient is the equation of state (EOS). The microphysics described in the EOS is directly linked to the macroscopic observation of mass and radius of NS via the Tolman-Oppenheimer-Volkoff (TOV) equations (Figure 1.3). The EOS can be written either in terms of energy per particle or pressure as a function of the density. The relation between pressure and energy per particle comes from the standard thermodynamical definition of pressure:

$$P = - \left(\frac{\partial E}{\partial V} \right)_N, \quad (1.1)$$

where P is the pressure, E is the total energy, and N indicates the total number of particles. The TOV equations for a spherically symmetric star [10, 11] are:

$$\frac{dP}{dr} = - \frac{G [m(r) + 4\pi r^3 P/c^2] [\epsilon + P/c^2]}{r [r - 2Gm(r)/c^2]}, \quad \frac{dm(r)}{dr} = 4\pi r^2 \epsilon, \quad (1.2)$$

where G is the gravitational constant, c is the speed of light, ϵ is the energy-density ($\epsilon = \rho(E + m_N)$, where m_N and ρ are the neutron mass and the number density respectively), $m(r)$ is the enclosed mass, and r is the radius; the particle density ρ is related to energy density ϵ and the pressure P by $P = \rho^2(\partial E/\partial \rho)$. These equations have to be integrated with proper boundary conditions to obtain the M-R relations. Illustrative results for schematic EOS and correspondence to M-R relation are reported in Figure 1.3, while results for realistic EOS within different theoretical approaches and choices of nuclear interactions are shown in Figure 1.4.

As discussed in the previous section, we have different models describing the inner core of NS. Here we report the main different interactions and approaches,

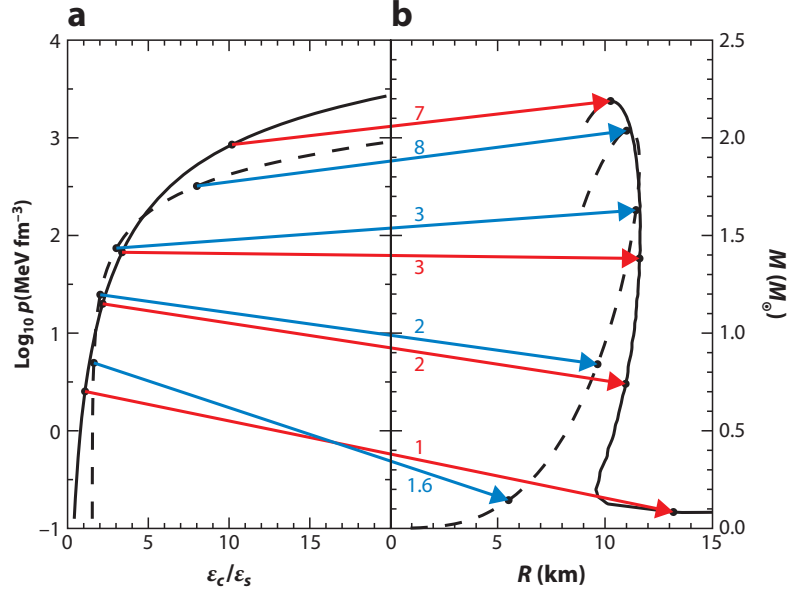


Figure 1.3: (a) Schematic hadronic (solid curves) and pure strange quark matter (dashed curves) equations of state. (b) The corresponding M – R relations. Arrows connect specific central energy density and pressure values with their corresponding (M, R) points. The numbers labeling hadronic arrows denote central baryon densities ρ_c/ρ_0 , and those labeling strange quark matter arrows indicate ϵ_c/ϵ_0 . The uppermost arrows in each case mark the maximum mass configurations (from Ref [20]).

some examples of which are summarized in Table 1.1.

For plain $npe\mu$ nuclear matter:

- potential-method EOSs (PAL1-6 [24] and SLy [25]);
- variational-method EOSs (AP1-4, aka APR1-4 [26] and WFF1-3 [27]);
- relativistic Brueckner-Hartree-Fock EOSs (ENG [28] and MPA1 [29]);
- relativistic mean-field theory EOSs (FSU [30] and MS0-2 aka MS1-2 and MS1b, which is identical to MS1 except with low symmetry energy [31].).

For models with hyperons, kaon condensation, and quarks:

- relativistic mean-field theory EOSs with hyperons (H1-7 [32] and GM1-3 [33]);

- relativistic mean-field theory EOSs with kaons (GS1-2 [34]);
- quark matter (SQM1-3 [35]).

For easier reading of the labeled EOS, we summarize the approaches and the compositions in Table 1.1.

Symbol	Approach	Composition
PAL1-6	Potential-method	np
SLy	Potential-method	np
AP1-4 (aka APR1-4)	Variational-method	np
WFF1-3	Variational-method	np
ENG	Relativistic Brueckner-Hartree-Fock	np
MPA1	Relativistic Brueckner-Hartree-Fock	np
FSU	Relativistic mean-field	np
MS0-2 (aka MS1-2/MS1b)	Relativistic mean-field	np
H1-7	Relativistic mean-field	npH
GM1-3	Relativistic mean-field	npH
GS1-2	Relativistic mean-field	npK
SQM1-3	Quark matter	$Q(u, d, s)$

Table 1.1: Symbol is the label for the EOS reported in Figure 1.4 and Figure 1.8 and approach refers to the underlying theoretical technique. Only the hadronic composition is reported with the following labels: n for neutron, p for proton, H for hyperon, K for kaon, Q for quarks ; all models include leptonic contributions. Readapted from Ref. [36].

In Figure 1.4, we present the M-R relation obtained solving the TOV equations for the collection of different interactions and approaches summarized in Table 1.1.

An interesting quantity that allows discriminating between different interactions and approaches is the maximum mass of a NS. EOSs, which not support maximum observed NS mass, are directly ruled out. In 2010 the highest value of a well-measured mass was for PSR J1614 – 2230, and it has been determined by

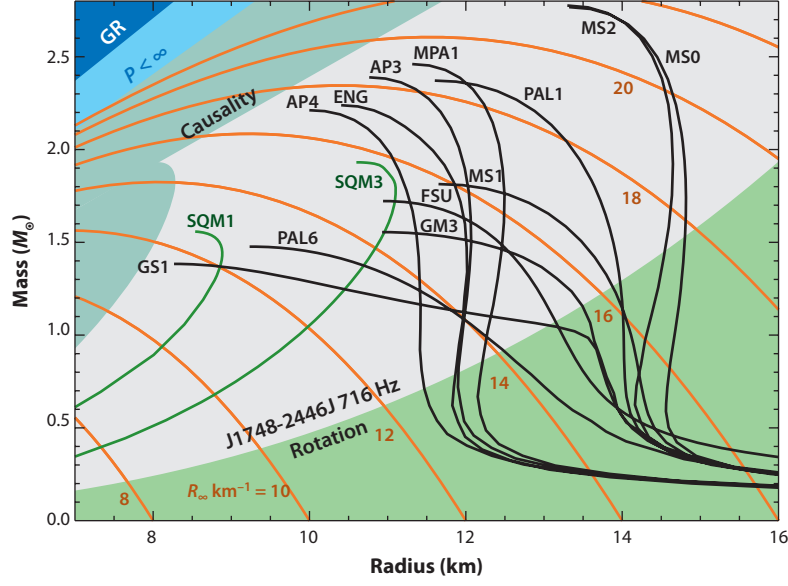


Figure 1.4: Typical M – R curves for hadronic equations of state (EOSs) (black curves) and strange quark matter (SQM) EOSs (green curves). The EOS names are given in Table 1.1. Regions of the M – R plane excluded by general relativity (GR), finite pressure, and causality are indicated. The orange curves show contours of the radiation radius R_∞ . The region marked rotation is bounded by the realistic mass-shedding limit for the highest-known pulsar frequency, 716 Hz, for PSR J1748 – 2446J [13]. Figure taken from Ref. [20].

detection of the Shapiro time delay. The reported value was initially $1.97 \pm 0.04 M_\odot$ [37]. Recent more accurate analysis (2016) updated this value to $1.928^{+0.017}_{-0.017} M_\odot$ (68.3% credibility interval [38]) and then to $1.908^{+0.016}_{-0.016} M_\odot$ in 2018 [39]. Within the same confidence level, the measured mass of PSR J0740 + 6620 is $2.14^{+0.10}_{-0.09} M_\odot$ (2019) [1], and another massive NS is PSR J0348 + 0432 with a measured mass of $2.01 \pm 0.04 M_\odot$ [40]. These recent observations confirm the prediction of the maximum mass of a NS to be $\sim 2.1 - 2.2 M_\odot$.

Our approach. Within this framework of different interactions and models, we use ab initio quantum Monte Carlo (QMC) methods as a comparison to previous results. This approach is discussed in detail in Chapter 3. QMC, in its standard formulation, requires the use of local potentials. To date, the most popular local interactions are the AVX family [41, 42, 43] and the recently developed local chiral effective field theory potentials [44, 45, 46, 47]. While three body forces

arise spontaneously in the diagrammatically expansion of chiral effective field theory, for phenomenological potentials they need to be artificially introduced. For the three-body sector either density-dependent interactions (like the DD6', fitted to reproduce experimental values of the saturation density $\rho_0 = 0.16 \text{ fm}^{-3}$, the binding energy per particle $E_0 = -16 \text{ MeV}$ and the compressibility $K \approx 240 \text{ MeV}$) or explicit three-body forces, as the ones of the Urbana group (UIX), have been used [48]. Argonne and Urbana potentials are presented in Chapter 2. At the present stage, some technical issues still prevent to produce controlled results on symmetric nuclear matter with the potentials, including spin-orbit and three-body forces with full operatorial dependence. For this reason, most calculations are limited to pure neutron matter (PNM). The use of DD interactions instead provides a way to address the full composition of a NS interior. As an example, in Figure 1.5 we report some results obtained with DD6' potential for $pne\mu$ model [48].

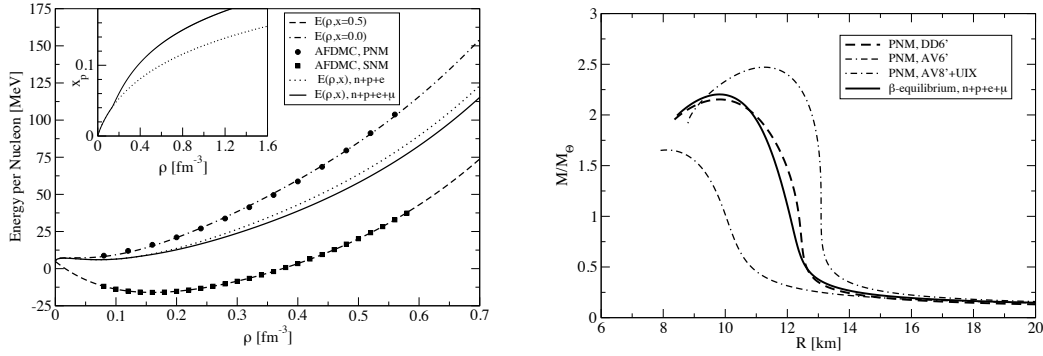


Figure 1.5: (left) The EOS for SNM (dashed line), PNM (dot-dashed line) and β -equilibrium nuclear matter with both electrons and muons (full line) and with electrons only (dotted line). In the inset the proton fraction x_p is shown. (right) M-R relation for different interactions (from Ref. [48]).

The possible onset of hyperons after some critical density has also been studied within QMC, within the PNM approximation. The presence of hyperons softens the EOS and makes it harder to reproduce observed NS masses of $\sim 2.1 M_\odot$, as shown in Figure 1.6. The main message is that information on the interaction between hyperons and nucleons, especially in the three-body sector, is scarce and not sufficient to establish the presence of hyperons in the core.

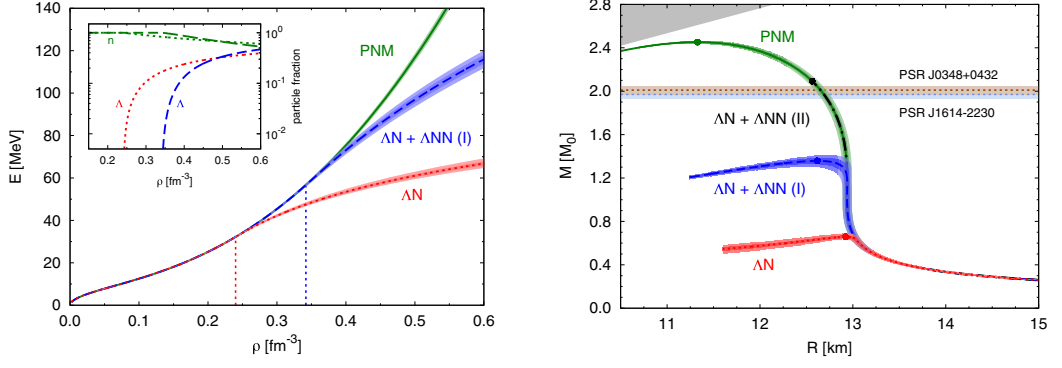


Figure 1.6: (left) The EOS for PNM (green) and two and three body hyperon potential (red and blue respectively). In the inset the Λ hyperon fraction is shown. (right) M - R relation for different interactions (from Ref. [49]).

With the detection of binary NS gravitational waves (GW170817), a new era began. Information coming from the post-merger signals also gives useful and complementary insights. On the one hand, constraints on the nuclear parameters (such as incompressibility, symmetry energy, and their slopes) can be extracted from the GW signals; on the other hand, realistic nuclear interaction can be used to infer the tidal deformability. The radius of the NS can also be derived from GW observations within some modeling. From the nuclear prospective, symmetry energy $E_{\text{sym}}(\rho)$ is defined as the difference between pure neutron matter (PNM) and the energy of symmetric nuclear matter (SNM). The energy per particle $E(\rho, x)$ of nuclear matter is usually expressed as a Taylor expansion in terms of isospin asymmetry $x = \rho_p / \rho$, where ρ_p and ρ are the proton number and baryon number densities respectively:

$$E(\rho, x) = E_0(\rho) + E_{\text{sym}}^{(2)}(\rho)(1 - 2x)^2 + E_{\text{sym}}^{(4)}(\rho)(1 - 2x)^4 + \dots, \quad (1.3)$$

where $E_0(\rho)$ is the EOS of symmetric nuclear matter ($E_0(\rho) = E(\rho, x = 0.5)$). $E_{\text{sym}}^{(4)}$ and higher order terms in the expansion are usually ignored. The symmetry energy $E_{\text{sym}}(\rho)$ is given by:

$$E_{\text{sym}}(\rho) = E(\rho, 0) - E_0(\rho), \quad (1.4)$$

where $E(\rho, 0)$ is the EOS for PNM. Note that $E_{\text{sym}}(\rho)$ is the same term which enters Equation (1.3) at quadratic order ($E_{\text{sym}}^{(2)}(\rho)$). Around saturation density the

symmetry energy can be expanded as a function of saturation density (since the pressure is zero):

$$E_{\text{sym}}(\rho)|_{\rho_0} = E_{\text{sym}} + \frac{L_0}{3} \frac{\rho - \rho_0}{\rho_0} + \dots, \quad (1.5)$$

where E_{sym} is the symmetry energy at saturation and L_0 is a parameter related to its slope. As an example, we report in Figure 1.7 the EOS for PNM and results of E_{sym} and L_0 for different models of the three-body Urbana potential.

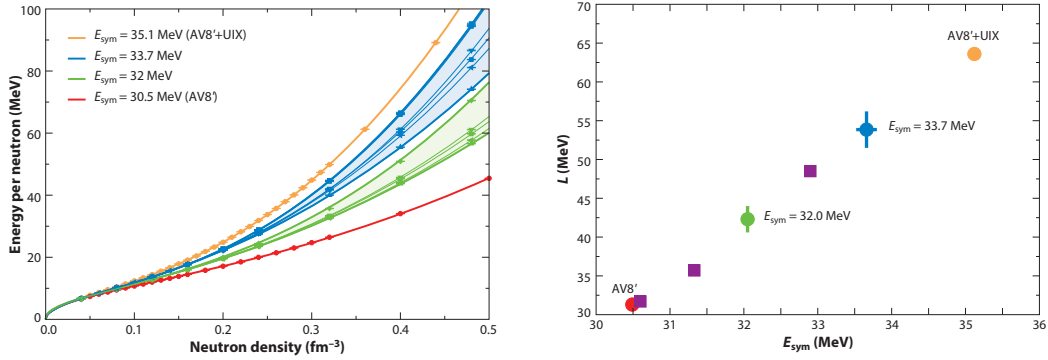


Figure 1.7: (left) The equation of state of neutron matter obtained by using various models of three-neutron force. The legend indicates the corresponding symmetry energy at saturation. (right) The value of slope L_0 (labeled as L in this plot) as a function of the symmetry energy E_{sym} obtained from various equations of state (EOSs). The square symbols correspond to results obtained by independently changing the cutoff parameters entering in V_R and in the three-pion rings of the three-neutron force (from Ref. [50]).

In general around saturation both symmetric nuclear matter and symmetry energy can be expanded in terms of $y = (\rho - \rho_0)/3\rho_0$ as:

$$\begin{aligned} E(\rho, 0) &= E_0 + \frac{K_0}{2}y^2 + \frac{Q_0}{6}y^3 + \mathcal{O}(y^4), \\ E_{\text{sym}}(\rho) &= E_{\text{sym}} + L_0y + \frac{K_{\text{sym},0}}{2}y^2 + \mathcal{O}(y^3), \end{aligned} \quad (1.6)$$

where E_0 is the binding energy of symmetric nuclear matter at saturation, K_0 is the incompressibility coefficient, Q_0 is the third derivative of symmetric matter. We already introduced E_{sym} and L_0 as the symmetry energy at saturation and the slope respectively and the final coefficient is the curvature at saturation density $K_{\text{sym},0}$. The binding energy of symmetric nuclear matter at saturation E_0 can be

extrapolated from the binding energy of heavy nuclei to the thermodynamic limit. The value is $E_0 = -16.0 \pm 0.1$ MeV [51]. A new coefficient is usually introduced, the derivative of the incompressibility, which is defined as $M_0 = Q_0 + 12K_0$. From gravitational waves detection of binary neutron stars, the parameters which can be extracted are the chirp mass \mathcal{M} and the mass-weighted average tidal deformability $\tilde{\Lambda}$. The chirp mass \mathcal{M} is defined as:

$$\mathcal{M} = \frac{(m_1 m_2)^{3/5}}{(m_1 + m_2)^{1/5}}, \quad (1.7)$$

where m_1 and m_2 are the two masses of the NS. Each NS has its tidal deformability (Λ_1 and Λ_2), but since they are strongly correlated, it is challenging to extract them independently. The mass-weighted average tidal deformability is defined as:

$$\tilde{\Lambda} = \frac{16(1 + 12q)\Lambda_1 + (12 + q)q^4\Lambda_2}{(1 + q)^5}, \quad (1.8)$$

where $q = m_2/m_1$ ($q < 1$) is the mass ratio between the two stars. The chirp mass \mathcal{M} of GW170817 has been measured with great accuracy $1.188^{+0.004}_{-0.002} M_\odot$, but the mass ratio q varies between 0.73 and 1.00 [4]. The extraction of the tidal deformability is hard and model-dependent, but an upper bound has been provided ($\tilde{\Lambda} \leq 800$).

From the nuclear EOS, tidal deformability $\tilde{\Lambda}$ can be predicted as shown in Figure 1.8.

From the observation of the tidal deformability $\tilde{\Lambda}$, it is possible to constrain nuclear parameters (within some modeling and some prior on the slope L_0 from experiments and astrophysical observations), as shown in Table 1.2.

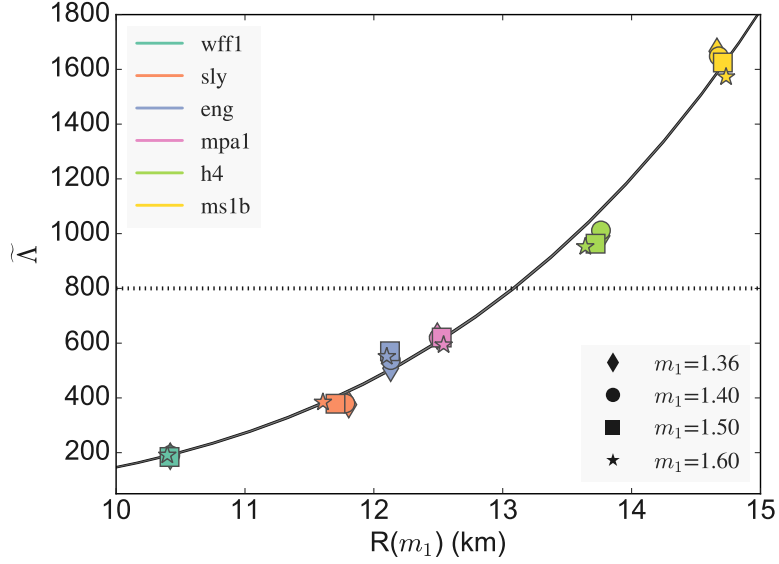


Figure 1.8: Effective tidal deformability of the binary system as a function of the radius of the primary neutron star. The tidal deformability is calculated for various primary masses (corresponding to the different symbols) using several proposed equations of state (corresponding to the different colors). The mass of the secondary neutron star is found assuming the chirp mass, $\mathcal{M} = 1.188 M_{\odot}$ from GW170817. The observed 90% confidence upper limit on $\tilde{\Lambda} \leq 800$ is shown as the dotted line. The narrow band (which is indistinguishable from a single curve) shows the range for $q = 0.7 - 1.0$. $\tilde{\Lambda}$ is relatively insensitive to m_1 but scales strongly with radius. Note that the upper limit for GW170817 implies $R \leq 13$ km (from Ref. [52]).

L_0 [MeV]	Method 2		Method 1	
	$\tilde{\Lambda}$ posterior distribution [53]	$70 \leq \tilde{\Lambda} \leq 720$ [53]	$70 \leq \tilde{\Lambda} \leq 720$ [53]	$279 \leq \tilde{\Lambda} \leq 720$ [54]
40 – 62 [55, 56, 57]	81 MeV $\leq K_0 \leq 362$ MeV 1556 MeV $\leq M_0 \leq 4971$ MeV –259 MeV $\leq K_{\text{sym},0} \leq 32$ MeV	100 MeV $\leq K_0 \leq 375$ MeV 1538 MeV $\leq M_0 \leq 5433$ MeV –358 MeV $\leq K_{\text{sym},0} \leq 23$ MeV	118 MeV $\leq K_0 \leq 388$ MeV 1849 MeV $\leq M_0 \leq 5609$ MeV –298 MeV $\leq K_{\text{sym},0} \leq 54$ MeV	
30 – 86 [58]	135 MeV $\leq K_0 \leq 340$ MeV 2069 MeV $\leq M_0 \leq 4798$ MeV –259 MeV $\leq K_{\text{sym},0} \leq 32$ MeV	45 MeV $\leq K_0 \leq 398$ MeV 955 MeV $\leq M_0 \leq 5675$ MeV –358 MeV $\leq K_{\text{sym},0} \leq 23$ MeV	63 MeV $\leq K_0 \leq 411$ MeV 1266 MeV $\leq M_0 \leq 5852$ MeV –298 MeV $\leq K_{\text{sym},0} \leq 54$ MeV	

Table 1.2: GW₁₇₀₈₁₇ constraints on the incompressibility K_0 (top row), its slope M_0 (middle row), and the symmetry energy curvature $K_{\text{sym},0}$ for four different sets of priors on L_0 [55, 56, 57, 58] and $\tilde{\Lambda}$ [53, 54]. These quantities are computed using two different methods described in the reference [59] (from Ref. [59]).

An alternative approach to determine the tidal polarizability $\tilde{\Lambda}$ assumes a polytropic equation of state:

$$P(\rho) = \frac{aL_0\rho_0}{3} \left(\frac{\rho}{\rho_0} \right)^\Gamma. \quad (1.9)$$

The tidal deformability has been estimated from the central values of the chirp mass $\mathcal{M} = 1.186 M_\odot$ and the mass ratio $q = 0.87$ from the GW170817 as reported in Figure 1.9.

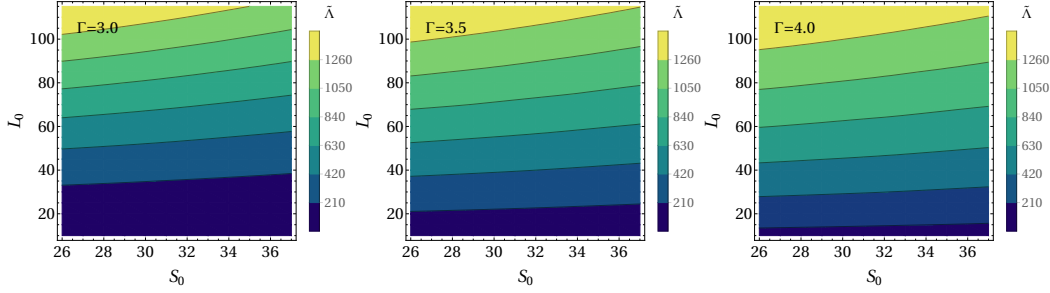


Figure 1.9: Effective tidal deformability of the binary system, as a function of E_{sym} (denoted as S_0) and L_0 . $\tilde{\Lambda}$ has been calculated using the polytropic approximation of the nuclear EOS for different values of the parameter Γ . $\tilde{\Lambda}$ is only weakly dependent on the symmetry energy S_0 , but that it is quite sensitive to L_0 . The constraints on $\tilde{\Lambda} = 300(+420/-230)$ from GW170817 [53] point to relatively small values of L_0 . (from Ref. [60]).

The GW observation of GW170817 put new insights into the physics of NS. The main issue is still to determine the radius of the NS accurately. A precise measure of the radius is the most robust constraint that can discriminate between the different choices of nuclear interactions and theoretical methods, as shown in Figure 1.4 and Figure 1.8. In Table 1.3 we report a summary of the current radius inferred from GW170817 (and some other constraints).

All the approaches point to a radius of a typical NS of $\sim 10 - 13$ km. This review is certainly not complete and exhaustive. More observation from gravitational waves might enforce actual constraints and give even more insights on the equation of state of nuclear matter, especially at nuclear densities beyond saturation.

Reference	R_i [km]		
<i>Without a phase transition</i>			
Bauswein et al. [61]	$10.68^{+0.15}_{-0.03} \leq$	$R_{1.6}$	
Fattoyev et al. [62]		$R_{1.4}$	≤ 13.76
Most et al. [63]	$12.00 \leq$	$R_{1.4}$	≤ 13.45
Lim Holt [64]	$10.36 \leq$	$R_{1.4}$	≤ 12.87
De et al. [65]	$8.9 \leq$	$R_{1.4}$	≤ 13.2
Malik et al. [66]	$11.82 \leq$	$R_{1.4}$	≤ 13.72
LIGO/Virgo [67]	$10.5 \leq$	R_{GW170817}	≤ 13.3
Tews et al. [68]	$11.3 \leq$	$R_{1.4}$	≤ 12.1
Köppel et al. [69]	$10.92 \leq$	$R_{1.4}$	
Raithel [70]	$9.8 \leq$	R_{GW170817}	≤ 13.2
<i>With a phase transition</i>			
Annala et al. [71]	$9.9 \leq$	$R_{1.4}$	≤ 13.6
Most et al. [63]	$8.53 \leq$	$R_{1.4}$	≤ 13.74
Tews et al. [68]	$9.2 \leq$	$R_{1.4}$	≤ 12.5
Montana et al. [72]	$10.1 \leq$	R_{GW170817}	≤ 13.11
<i>From multimessenger analyses</i>			
Radice Dai [73]	$11.4 \leq$	$R_{1.4}$	≤ 13.2
Coughlin et al. [54]	$11.1 \leq$	$R_{1.4}$	≤ 13.4
Kumar Landry [74]	$9.4 \leq$	$R_{1.4}$	≤ 12.8

Table 1.3: Constraints on the radius of NSs from GW170817 (and some other observations) from works that report in their text estimates for the radius $R_{1.4}$ of a $1.4 M_{\odot}$ star or the radius of the NSs in GW170817, considering EOSs without and with a phase transition and from multimessenger analyses (from Ref. [75]). Further notes on each estimate are provided in the reference.

1.3 MAGNETARS

Magnetars are a class of young neutron stars with strong measured superficial magnetic fields. This name was given in 1992 by Duncan and Thompson after

their emission powered by the decay of huge internal magnetic fields. Magnetars exhibit a strong variability on the X-ray, and soft γ -ray energies, and they are accordingly classified into anomalous X-ray pulsars (AXPs) and soft gamma repeaters (SGRs). The first observation was in 1979 by Mazets et al. [76, 77, 78], though it had not been identified as a magnetar. Currently there are informations on 29 magnetars: 15 SGRs (11 confirmed, 4 candidates), and 14 AXPs (12 confirmed, 2 candidates). Updated information can be found in the online catalog [79]. In Figure 1.10 we report the population distribution of magnetars as a function of the magnetic field B . The maximum superficial magnetic field can be as high as $\sim 10^{14} - 10^{15}$ G. The internal composition and strength of the magnetic

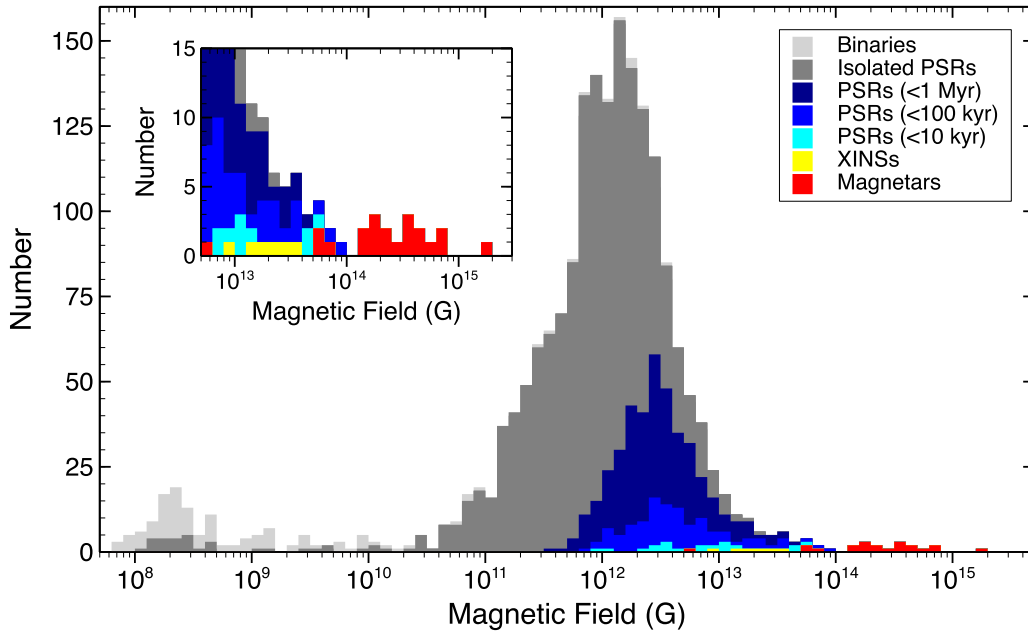


Figure 1.10: Histogram showing the distribution in magnetic field B , of all known radio pulsars (PSRs), X-ray isolated neutron stars (XINs), and magnetars. Inset: zoom-in on $B > 5 \times 10^{12}$ G to better show the distribution of the magnetars (from Ref. [79]).

fields are poorly known and only models can be made. Recent observation of PSR J0030+0451 [21, 23, 80] showed that the simple magnetic dipole model could not describe the measured hot spots. This indicates that the pulsar magnetic fields are more complex and are not understood as well as the shape and arrangements of

the hot spots. Some different models of the possible configurations of the internal magnetic fields are shown in Figure 1.11. The intensity of the toroidal magnetic field within the different models is shown in Figure 1.12.

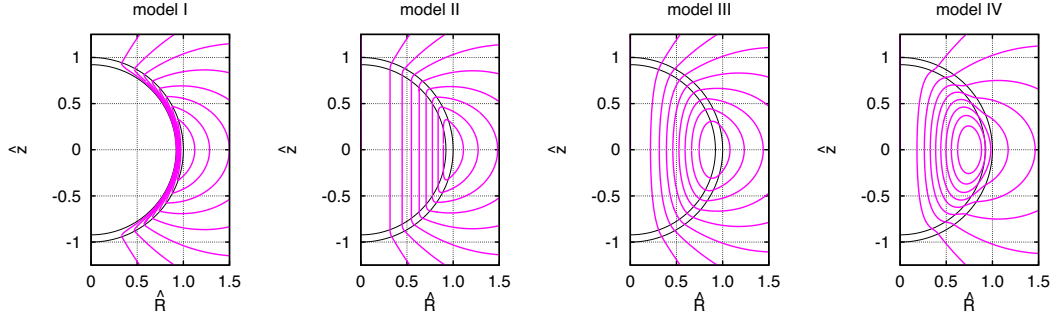


Figure 1.11: The contours of the magnetic field in different analytical models (solid magenta lines). The inner curve is the core–crust boundary, and the outer curve is the stellar surface (black). Model I: this model has purely crustal open magnetic fields. There is a negative current sheet on the core–crust boundary in order to exclude the core magnetic fields. Model II: this model has a purely crustal toroidal current. The core magnetic field is an inner vacuum solution of the crustal toroidal current. Model III: this model has both crustal and core toroidal currents. The configuration of the core magnetic field is different from Model II. Model IV: this model has opposite flowing toroidal current density. The core magnetic fields are stronger than crustal magnetic fields. The \hat{z} and \hat{R} denote normalized forms of radius R and cartesian coordinate z with respect to the stellar radius (from Ref. [81]).

Depending on the model, the intensity of the magnetic field can increase up to $\sim 10 - 20$ times with respect to the superficial intensity in the outer core.

We think that in this region, spin polarization might play a non-negligible role in the description of the neutron star. We discuss the effect of spin polarization on the compressibility and neutrino mean free path in Chapter 4 within a mean-field approximation. In the same chapter, we will present updated results for the magnetic susceptibility from QMC calculations.

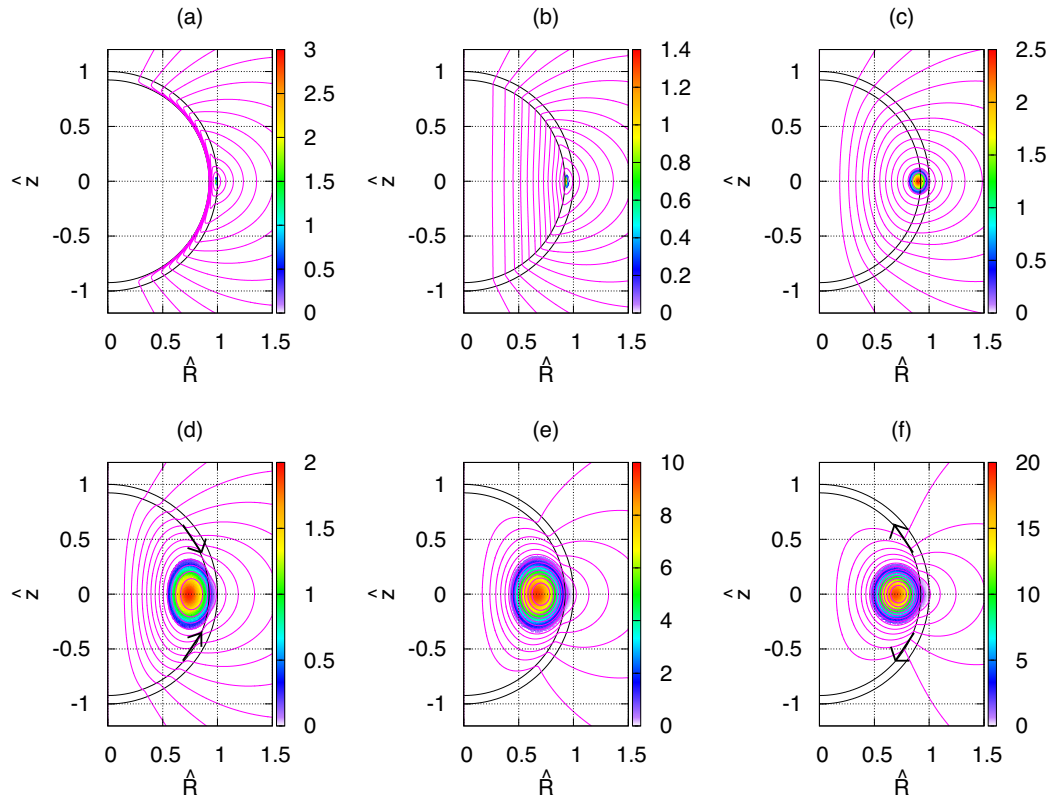


Figure 1.12: Same structure of Figure 1.11. The color maps denote the magnitude of the toroidal magnetic field normalized by the strength of the dipole component at the North Pole. (a) solution for model I type, (b) solution for model II type, (c) solution for model III type, (d), (e), (f) solutions for model IV type with different current sheets (positive, zero and negative respectively) (from Ref. [81]).

NUCLEON-NUCLEON INTERACTION

Modern nuclear interactions can be essentially divided into two main groups: on the one hand, the phenomenological potentials; on the other hand, the interactions developed from chiral effective field theory.

The general non-relativistic nuclear Hamiltonian can be written as:

$$H = T + \sum_{i < j} V_{ij}^{\text{NN}} + \sum_{i < j < k} V_{ijk}^{\text{3N}} + \dots, \quad (2.1)$$

where T is the non-relativistic kinetic energy, V_{ij}^{NN} and V_{ijk}^{3N} are the two- and three-nucleon potentials, while the ellipsis stands for contributions coming from interactions involving more than three nucleons. Many-body contribution to the potential can be neglected, as suggested by nuclear matter studies [82], since they are small compared to the current level of precision.

The approach of phenomenological interactions is to fit the two-body part of the interaction to Nijmegen nucleon-nucleon (in particular pp and np , where p and n stand for proton and neutron respectively) scattering data [83], to the nn scattering length, and to the deuteron binding energy. Potentials with χ^2 per datum of order 1 are called realistic interactions. Two-body interactions are not sufficient to describe binding energies of ${}^3\text{H}$ and ${}^3\text{He}$. Three-nucleon forces need to be introduced. They describe processes such as two-pion exchange in S-wave and P-wave and three-pion rings with one or two Δ intermediate states. Unfortunately, there is no consistent description of light nuclei and nuclear matter simultaneously. The choice of the three-body force is crucial, especially in nuclear matter calculations. Different three-body interactions lead to very different results of the EOS of pure neutron matter at high densities [84, 85, 86].

A new approach to derive nuclear interactions, which in principle gives a consistent approach to the description of both nuclei and nuclear matter, has been recently proposed. Chiral effective field theory (EFT) interactions rely on a separation of scales (between pion mass and vector meson masses) and exploit the symmetries of quantum chromo-dynamics (QCD). The separation of scales comes from the energy separation of the relevant degrees of freedom and permits to integrate out the contribution from higher energy scales. Chiral EFT can be constructed in a systematic way as an expansion in terms of p/Λ_b , where p is the typical momentum scale of the system and Λ_b the breakdown scale of the theory, according to a power counting scheme. Order by order, the theory is improved, and many-body interactions arise naturally from the diagrammatical expansion. The unresolved physics is encoded in the so-called low energy constants (LECs), which are fitted to experimental data. Chiral EFT interactions provide a consistent way to derive electroweak currents, and the predicted theoretical uncertainties are a reliable way to compare theoretical results to experiments. On the contrary, phenomenological models do not provide ways to estimate theoretical errors, and they miss a consistent derivation of electroweak currents.

2.1 PHENOMENOLOGICAL POTENTIAL

Realistic phenomenological potentials, and in particular the Argonne family [41], have been able to accurately describe light nuclei binding energies as well as nuclear matter using quantum Monte Carlo (QMC) methods (for a review [87]). The strong interaction part of the NN potential is written as a sum of a one-pion exchange and a short-range phenomenological part. The one-pion exchange (OPE) part of the potential is given by:

$$V_{ij}^{\text{NN},\pi} = \frac{f_\pi^2 m_\pi}{4\pi \cdot 3} [Y(m_\pi r) \boldsymbol{\sigma}_i \cdot \boldsymbol{\sigma}_j + T(m_\pi r) Y(m_\pi r) S_{ij}] \boldsymbol{\tau}_i \cdot \boldsymbol{\tau}_j, \quad (2.2)$$

where f_π is the nucleon-pion (N π) coupling constant ($f_\pi^2/4\pi = 0.075 \pm 0.002$ [88]) and m_π is the average pion mass. $Y(x) = \exp(-x)/x \cdot f_R(x)$ is the Yukawa function and $T(x) = (1 + 3/x + 3/x^2) \cdot f_R(x)$ the tensor function, where $f_R(x)$

is a regulator function with a short range cutoff ($f_R(x) = 1 - \exp(-cx^2)$, with cutoff parameter $c = 2.1 \text{ fm}^{-2}$). S_{ij} is the tensor operator in coordinate space $S_{ij} = 3(\sigma_i \cdot \hat{r})(\sigma_j \cdot \hat{r}) - \sigma_i \cdot \sigma_j$, and σ and τ are the Pauli matrix acting respectively on the spin and isospin of the nucleon.

The remaining phenomenological part $V_{ij}^{\text{NN},R}$ describes the intermediate and short-range part with tunable parameters. It is written as a sum of central, quadratic relative angular momentum, tensor, spin-orbit, and quadratic spin-orbit terms in different channels multiplied by radial functions. The radial functions are written as a sum of a two-pion exchange ($T^2(x)$) term and a quadratic radial expansion multiplied by a Wood-Saxon potential ($(1 + r + r^2)W(r)$). Each term is multiplied by a coefficient, and it is determined from fitting to experimental data. This potential has been fitted to Nijmegen NN scattering database up to 350 MeV, to nn scattering length, and deuteron binding energies. The phase shifts in terms of partial waves are reported in Figure 2.1. The potential can be also written as a

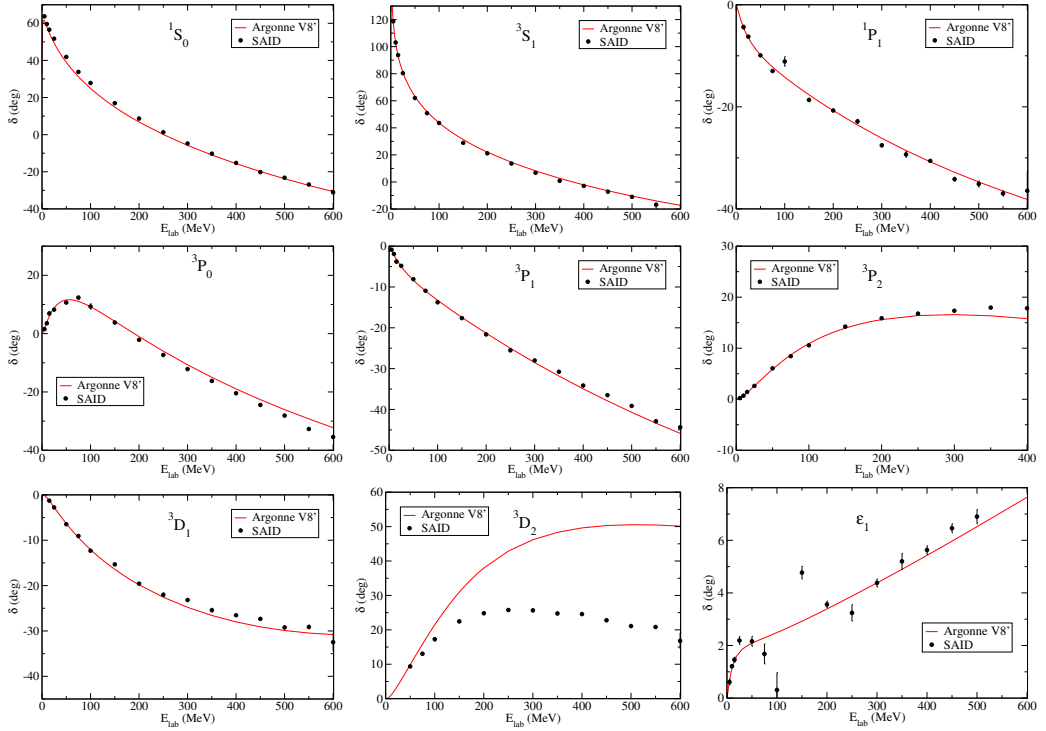


Figure 2.1: Phase shifts of AV8' nucleon-nucleon potential. Experimental phase shifts are from the SAID Partial-Wave Analysis Facility (gwdac.phys.gwu.edu).

sum of 18 operators:

$$V_{ij}^{\text{NN}} = V_{ij}^{\text{NN},\pi} + V_{ij}^{\text{NN},R} = \sum_{p=1,18} v_p(r) O_{ij}^p, \quad (2.3)$$

where $V_{ij}^{\text{NN},R}$ is the phenomenological part. The 18 operators O_{ij}^p are:

$$\begin{aligned} O_{ij}^{1-8} &= \{\mathbb{1}, \boldsymbol{\sigma}_i \cdot \boldsymbol{\sigma}_j, S_{ij}, \mathbf{L} \cdot \mathbf{S}\} \times \{\mathbb{1}, \boldsymbol{\tau}_i \cdot \boldsymbol{\tau}_j\} \\ O_{ij}^{9-14} &= \{\mathbf{L}^2, \mathbf{L}^2 \boldsymbol{\sigma}_i \cdot \boldsymbol{\sigma}_j, (\mathbf{L} \cdot \mathbf{S})^2\} \times \{\mathbb{1}, \boldsymbol{\tau}_i \cdot \boldsymbol{\tau}_j\} \\ O_{ij}^{15-18} &= \{T_{ij}, \boldsymbol{\sigma}_i \cdot \boldsymbol{\sigma}_j T_{ij}, S_{ij} T_{ij}, \tau_i^z + \tau_j^z\}, \end{aligned} \quad (2.4)$$

where \mathbf{L} is the relative angular momentum of the pair ($\mathbf{L} = -i\mathbf{r} \times (\nabla_i - \nabla_j)/2$), \mathbf{S} is the total spin, and $T_{ij} = 3\tau_i^z \tau_j^z - \boldsymbol{\tau}_i \cdot \boldsymbol{\tau}_j$ is the isotensor operator.

There are simplified versions of this potential, i.e. with fewer operators. They are denoted with the prime symbol. Instead of just truncating the number of operators, the contributions coming from the omitted operators are reprojected into the available operators. We adopt AV8' (see [42] for AV8', and [43] for a general AVX' interaction) for the nn interaction for pure neutron matter, where the number 8 indicates that the potential is written in terms of only the first eight operators. It has been shown that the difference in energies per nucleon between the full Argonne potential (AV18) and AV8' is less than 0.25% in neutron drops [89] and small for pure neutron matter (see Figure 2.3) [90]. Two body potentials are not able to reproduce binding energies of $A = 3$ nuclei and also the maximum mass of neutron stars, so we need to introduce three-body forces.

2.1.1 Three-body forces

In addition to two-body Argonne potential, two different families of three-body forces have been developed: Illinois and Urbana. The Urbana potentials give a three-body force which is a sum of a two-pion exchange term in P -wave and a short-range phenomenological term, while Illinois series also includes a two pion-exchange term in S -wave and a term which describes the most important diagrams of the three-pion rings with one or two Δ intermediate states diagrams (The diagrams showing the different terms are reported in Figure 2.2).

The most recent version of the Illinois potential series is the IL7 potential [91]. The

IL7 three-body force in combination with AV18 two-body potential gives a good the description of ground- and excited states energies, while it fails to describe pure neutron matter [92] (see Figure 2.3).

For pure neutron matter, UIX [93, 94] potential in addition to AV18 provides sufficient repulsion and consequently reasonable properties of nuclear matter (see Figure 2.3), but fails to give an accurate description of energies spectra of light nuclei.

Since we want to describe dense neutron matter, we adopt the phenomenological potential AV8'+UIX.

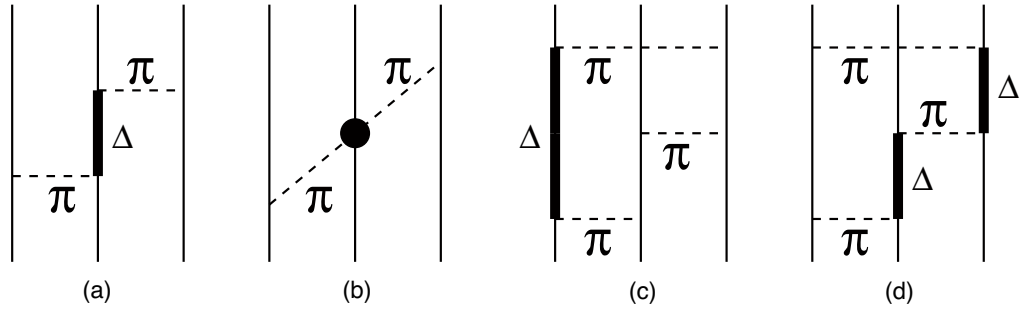


Figure 2.2: Three-body force Feynman diagrams: (a) is the Fujita-Miyazawa or two-pion P -wave, (b) is the two-pion in S -wave and (c), (d) are three-pion ring terms (From Ref. [87]).

The UIX potential can be written as:

$$V_{ijk}^{3N} = V_{ijk}^{2\pi,P} + V_{ijk}^R, \quad (2.5)$$

where $V_{ijk}^{2\pi,P}$ and V_{ijk}^R stand for the two-pion exchange term in P -wave and the short-range phenomenological term, respectively. The two pion-exchange term was first written by Fujita-Miyazawa [95] and it describes the two-pion exchange in P -wave as:

$$V_{ijk}^{2\pi,P} = \sum_{\text{cyc}} A_{2\pi}^P \{X_{ij}^\pi, X_{jk}^\pi\} \{\boldsymbol{\tau}_i \cdot \boldsymbol{\tau}_j, \boldsymbol{\tau}_j \cdot \boldsymbol{\tau}_k\} + C_{2\pi}^P [X_{ij}^\pi, X_{jk}^\pi] [\boldsymbol{\tau}_i \cdot \boldsymbol{\tau}_j, \boldsymbol{\tau}_j \cdot \boldsymbol{\tau}_k], \quad (2.6)$$

where the sum is over the three cycling exchanges of nucleons i, j, k and X_{ij}^π is defined from the AV18 model as:

$$X_{ij}^\pi = [Y(m_\pi r) \boldsymbol{\sigma}_i \cdot \boldsymbol{\sigma}_j + T(m_\pi r) S_{ij}], \quad (2.7)$$

where $Y(x)$ and $T(x)$ are the Yukawa and tensor functions respectively, as described above. In UIX model $C_{2\pi}^P = (1/4)A_{2\pi}^P$ as in the original Fujita-Miyazawa model.

The phenomenological part is given by:

$$V_{ijk}^R = \sum_{cyc} A_R T^2(m_\pi r_{ij}) T^2(m_\pi r_{jk}) , \quad (2.8)$$

where $T(x)$ is the tensor function and the sum runs on the nucleon indices i, j, k cyclically exchanging them.

The parameters of the UIX model were determined by fitting the binding energy of ${}^3\text{H}$ and the density of nuclear matter in conjunction with AV18. In Figure 2.3, we report results for PNM with different kinds of phenomenological potentials.

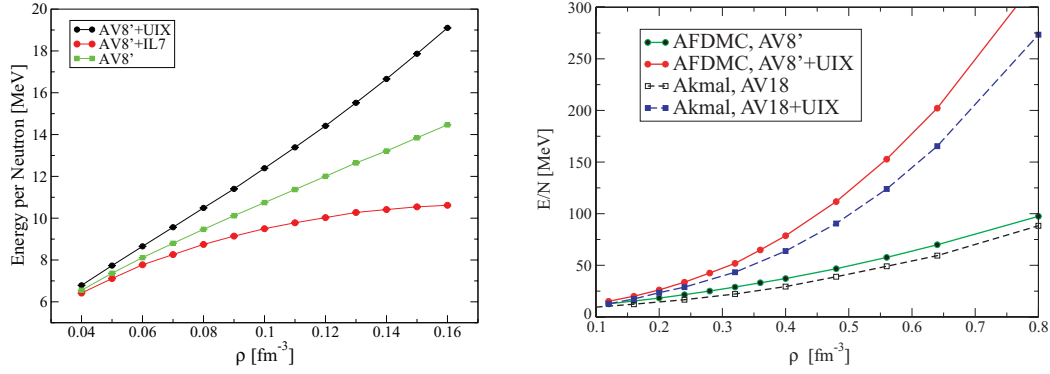


Figure 2.3: PNM EOS for the phenomenological potentials described in the text. (left panel - from Ref. [92]) AFDMC results for PNM with phenomenological AV8', AV8'+UIX and AV8'+IL7. (right panel - from Ref. [90]) AFDMC results for AV8' and AV8'+UIX compared to variational calculations using the full AV18 and AV18+UIX potentials of Ref [26].)

2.2 LOCAL CHIRAL EFFECTIVE FIELD THEORY POTENTIAL

As introduced in the first part of this chapter, another approach to describe nucleon-nucleon interaction is chiral effective field theory (EFT). This approach

relies on a separation of scales between the energy of the physics of the relevant degrees of freedom and contribution from higher energy scales. The chiral EFT potential can be written as an expansion in terms of:

$$V = \sum_{\nu=0}^{\infty} V^{\nu} (c_i^{\nu}) \left(\frac{p}{\Lambda_b} \right)^{\nu}, \quad (2.9)$$

where p is the typical momentum scale of the system and Λ_b is the breakdown scale of the theory. $V^{\nu} (c_i^{\nu})$ is the contribution at order ν and depends on the low-energy constants c_i^{ν} (LECs). Clearly the expansion is valid only when $p \ll \Lambda_b$. Feynman diagrams can be systematically evaluated and classified according to Weinberg power counting, as shown in Figure 2.4. This naturally leads to consistent three- and many-body forces. The orders of the expansion are classified as leading order (LO), next-to-leading order (NLO), next-to-next-to-leading order (N2LO), and so on. The infinite series can be truncated since the expansion is perturbative, and the contributions coming from higher-order terms decrease.

The natural formulation of the theory is in momentum space, but, as we previously mentioned, QMC methods work best with local interactions in coordinate space. Denoting \mathbf{p} and \mathbf{p}' the relative incoming and outgoing momenta of the two nucleons, and with $\mathbf{q} = \mathbf{p}' - \mathbf{p}$ and $\mathbf{k} = (\mathbf{p}' + \mathbf{p})/2$ the momentum transfer and the momentum transfer in the exchange channel, the local terms are the terms depending on \mathbf{q} , while those depending on \mathbf{k} are nonlocal. We briefly review the formulation of the EFT potential in momentum space and how to work out a local version [44, 45]. We use a local version of the chiral EFT potential up to N2LO. Note that at this order, three-nucleon forces arise, and contribution from more than three-body terms appear only at higher orders. No local version of the EFT potentials up to N3LO can be obtained since the non-locality can not be eliminated completely.

The long-range part of the NN potential is described by one- and two-pion exchange. One-pion exchange appears as the LO term, and in momentum space is written as:

$$V_{1\pi, \text{LO}}^{\text{mom}} = W_T^{(0)}(q) (\boldsymbol{\tau}_1 \cdot \boldsymbol{\tau}_2) (\boldsymbol{\sigma}_1 \cdot \mathbf{q}) (\boldsymbol{\sigma}_2 \cdot \mathbf{q}) = - \left(\frac{g_A}{2f_{\pi}} \right)^2 \frac{(\boldsymbol{\sigma}_1 \cdot \mathbf{q}) (\boldsymbol{\sigma}_2 \cdot \mathbf{q})}{\mathbf{q}^2 + m_{\pi}^2} \boldsymbol{\tau}_1 \cdot \boldsymbol{\tau}_2, \quad (2.10)$$

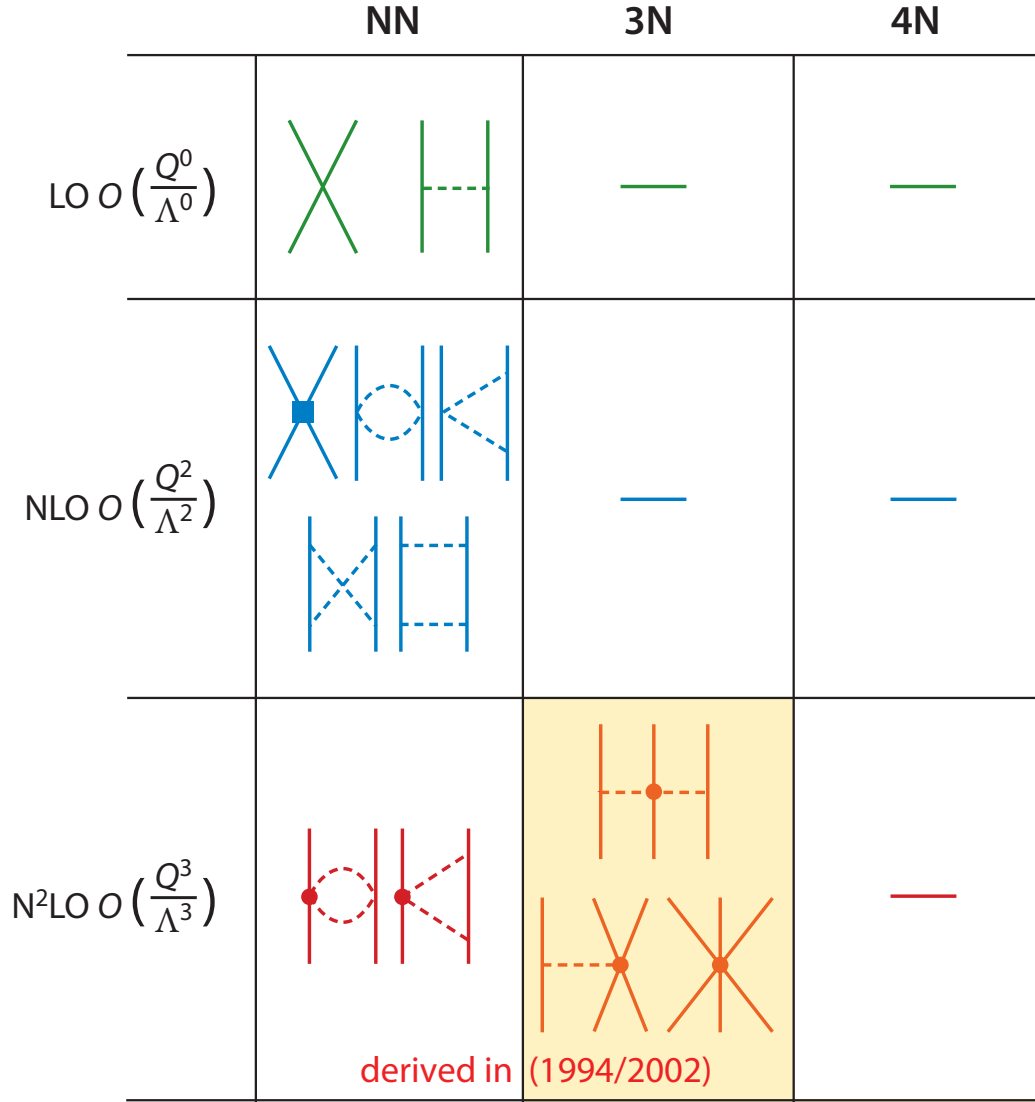


Figure 2.4: Chiral effective field theory for nuclear forces. The different contributions at successive orders are shown diagrammatically. Solid and dashed lines indicate nucleons and pions, respectively. 3N forces at N2LO, including the year they were derived, are highlighted in gold. Modified from Ref. [96].

and the two-body part of the two-pion contribution exchanges at NLO and N2LO as:

$$\begin{aligned}
 V_{2\pi, \text{NLO}}^{\text{mom}} &= W_C^{(2)}(q) (\boldsymbol{\tau}_1 \cdot \boldsymbol{\tau}_2) + V_S^{(2)}(q) (\boldsymbol{\sigma}_1 \cdot \boldsymbol{\sigma}_2) + V_T^{(2)}(q) (\boldsymbol{\sigma}_1 \cdot \mathbf{q}) (\boldsymbol{\sigma}_2 \cdot \mathbf{q}) \\
 V_{2\pi, \text{N}^2\text{LO}}^{\text{mom}} &= V_C^{(3)}(q) + W_S^{(3)}(q) (\boldsymbol{\tau}_1 \cdot \boldsymbol{\tau}_2) (\boldsymbol{\sigma}_1 \cdot \boldsymbol{\sigma}_2) + W_T^{(3)}(q) (\boldsymbol{\tau}_1 \cdot \boldsymbol{\tau}_2) (\boldsymbol{\sigma}_1 \cdot \mathbf{q}) (\boldsymbol{\sigma}_2 \cdot \mathbf{q}) ,
 \end{aligned}
 \tag{2.11}$$

where the subscripts C , S and T stand for the central, spin-spin and tensor contributions and the superscripts (0), (2) and (3) indicates the order of the expansion in ν . The functions $V^{(2,3)}$ and $W^{(2,3)}$ are spectral function representations (SFRs) with different spectral functions and ultraviolet cutoff $\tilde{\Lambda}$. In the local formulation the potential is not much sensitive to the cutoff $\tilde{\Lambda}$ and it usually varied in the range $\tilde{\Lambda} = 1.0 - 1.4$ GeV. In the SFRs three LECs (c_1 , c_3 and c_4) appear to describe subleading pion-nucleon vertices [97].

The short-range physics is described by contact interactions, which at LO are momentum independent and are written as:

$$V_{\text{cont,LO}}^{\text{mom}} = \alpha_1 \mathbb{1} + \alpha_2 \boldsymbol{\sigma}_1 \cdot \boldsymbol{\sigma}_2 + \alpha_3 \boldsymbol{\tau}_1 \cdot \boldsymbol{\tau}_2 + \alpha_4 \boldsymbol{\sigma}_1 \cdot \boldsymbol{\sigma}_2 \boldsymbol{\tau}_1 \cdot \boldsymbol{\tau}_2, \quad (2.12)$$

where α_i are LECs. Among the four contact terms at LO, only two are linearly independent. The conventional choice is [98]:

$$V_{\text{cont,LO}}^{\text{mom}} = C_S + C_T \boldsymbol{\sigma}_1 \cdot \boldsymbol{\sigma}_2, \quad (2.13)$$

where C_S and C_T are combination of α_i . The "contact" definition comes from the fact that in coordinate space, these terms lead to Dirac deltas $\delta(r)$. At NLO, 14 different contact interactions are allowed by symmetries, but only seven couplings are independent. It is possible to rearrange the terms to obtain a local interaction (eliminating the terms depending on \mathbf{k}) as:

$$\begin{aligned} V_{\text{cont}}^{(2)} = & C_1 q^2 + C_2 q^2 \boldsymbol{\tau}_1 \cdot \boldsymbol{\tau}_2 + (C_3 q^2 + C_4 q^2 \boldsymbol{\tau}_1 \cdot \boldsymbol{\tau}_2) \boldsymbol{\sigma}_1 \cdot \boldsymbol{\sigma}_2 \\ & + i \frac{C_5}{2} (\boldsymbol{\sigma}_1 + \boldsymbol{\sigma}_2) \cdot \mathbf{q} \times \mathbf{k} + C_6 (\boldsymbol{\sigma}_1 \cdot \mathbf{q}) (\boldsymbol{\sigma}_2 \cdot \mathbf{q}) + C_7 (\boldsymbol{\sigma}_1 \cdot \mathbf{q}) (\boldsymbol{\sigma}_2 \cdot \mathbf{q}) \boldsymbol{\tau}_1 \cdot \boldsymbol{\tau}_2, \end{aligned} \quad (2.14)$$

where the only non-local term is the spin orbit (C_5). Both the long- and the short-range parts of the potential need to be regularized. The long-range part is Fourier transformed and then a local regulator of the form [44]:

$$f_R^{\text{long}}(r) = \left(1 - e^{-(r/R_0)^4}\right) \quad (2.15)$$

is applied. This assures the convergence of the long-range part at distances smaller than R_0 . On the other hand the $\delta(r)$ functions which appear from the contact interactions are written as Dirac representation as:

$$f_R^{\text{short}}(r) = \alpha e^{-(r/R_0)^4}, \quad (2.16)$$

where α is the normalization constant. R_0 is usually taken ~ 1 fm, which corresponds to momentum-space cutoffs of the order of ~ 500 MeV.

The local chiral potential $V(r)$ can be decomposed into the central, central-isospin, spin, spin-isospin, spin-orbit, tensor, and tensor-isospin components as:

$$\begin{aligned}
 V(r) = & V^C(r) + V^{C\tau}(r)\boldsymbol{\tau}_1 \cdot \boldsymbol{\tau}_2 + [V^\sigma(r) + V^{\sigma\tau}(r)\boldsymbol{\tau}_1 \cdot \boldsymbol{\tau}_2]\boldsymbol{\sigma}_1 \cdot \boldsymbol{\sigma}_2 \\
 & + V^{LS}(r)\mathbf{L} \cdot \mathbf{S} + [V^T(r) + V^{T\tau}(r)\boldsymbol{\tau}_1 \cdot \boldsymbol{\tau}_2] S_{12}(r) ,
 \end{aligned} \tag{2.17}$$

where the operators have similar structures of the ones of the Argonne series. The obtained phase shifts for different partial waves are shown in Figure 2.5. The three-nucleon interactions can also be written in coordinate space as a sum of three terms: a two-pion-exchange part (TPE, denoted by V_C), a one-pion-exchange-contact interaction (V_D), and a 3N contact interaction (V_E). While V_C is determined from LECs c_1 , c_3 and c_4 , two new LECs, namely c_D and c_E , need to be fit to describe V_D and V_E respectively. The local version of V_C is given in Ref. [46], while local expression for V_D and V_E are given in Ref. [47]. When working in momentum space, different operatorial structures of V_D and V_E are allowed. The ambiguity on the operatorial expression for the contact interactions comes from the regulator artifacts in coordinate space. Some possible choices are described in detail in Ref. [47] with the corresponding values for LECs c_E and c_D . From the same Reference, we report results for PNM with different choices of V_E in Figure 2.6. The two couplings are fitted to the ${}^4\text{He}$ binding energy and low-energy $n - \alpha$ scattering P -wave phase shifts.

A comparison between PNM matter results with phenomenological and local chiral EFT potentials described in this chapter are reported in Figure 2.7. Among the different operatorial choices, we choose the one which gives closer results for PNM to the phenomenological potential, i.e. V_{E1} with a cutoff of $R_0 = 1.0$ fm.

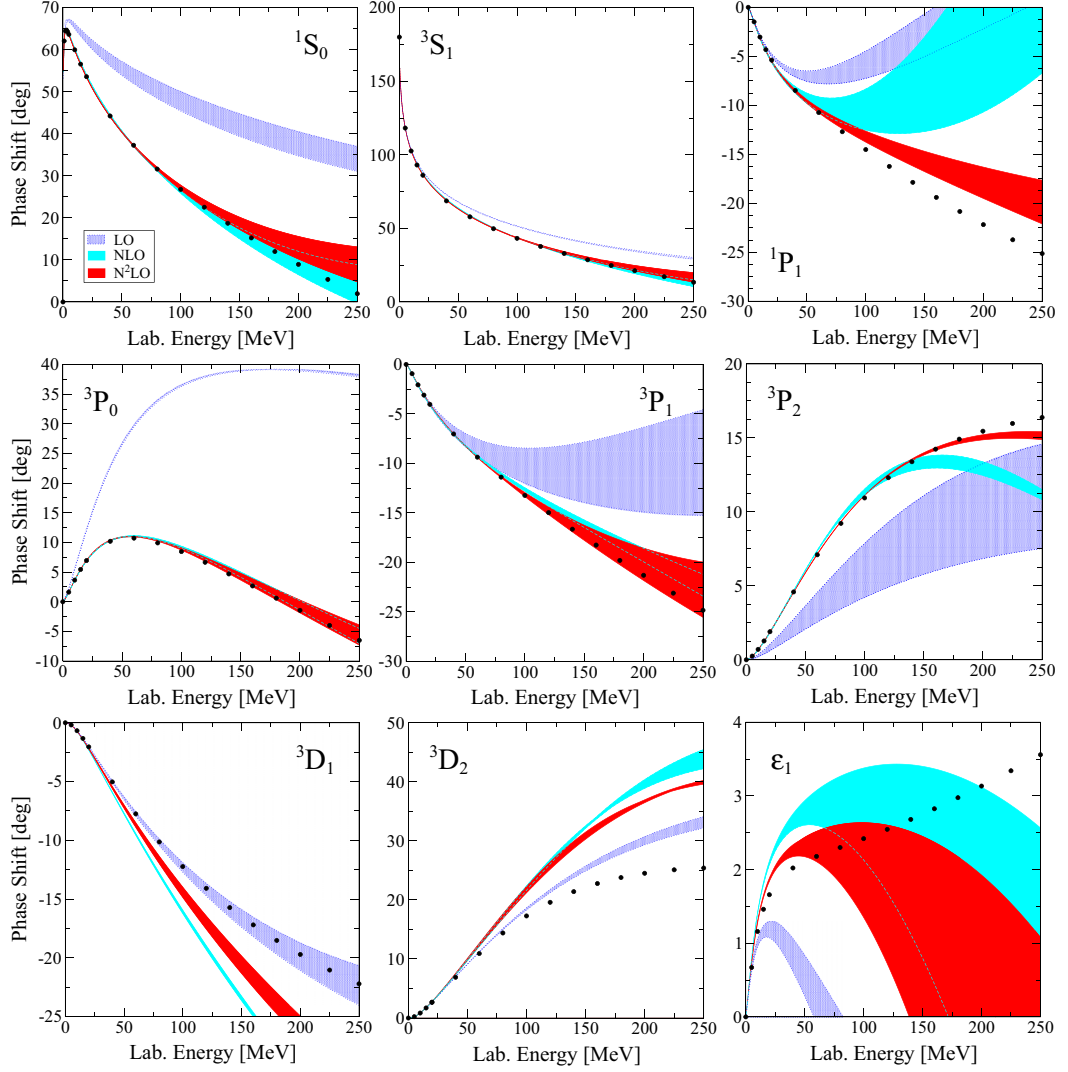


Figure 2.5: Phase shifts for the partial waves at LO, NLO, and N2LO in comparison with the Nijmegen PWA (from Ref. [83]). The bands at each order correspond to the cutoff variation of $R_0 = 1.0 - 1.2$ fm. At NLO and N2LO, we also vary the SFR cutoff from $\tilde{\Lambda} = 1.0 - 1.4$ GeV (from Ref. [45]).

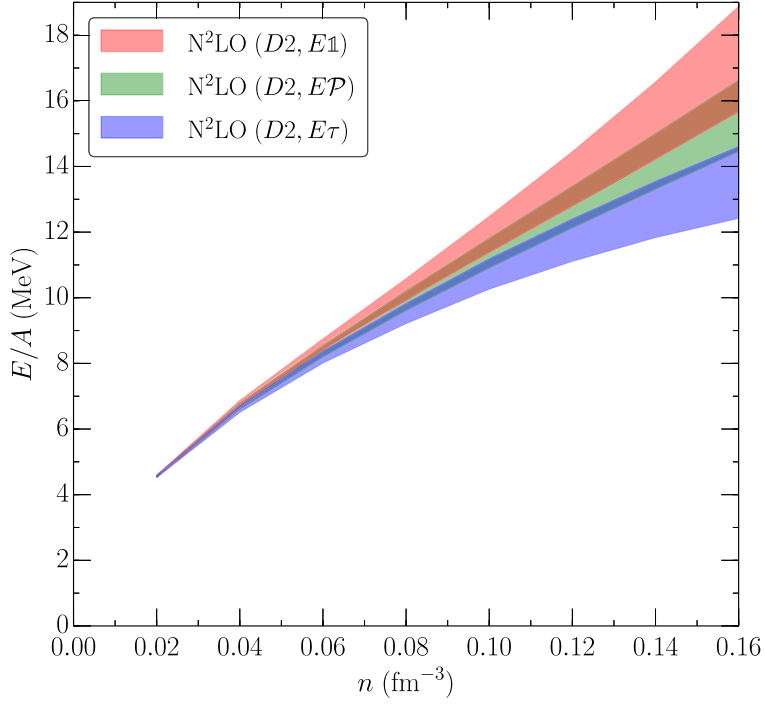


Figure 2.6: The energy per particle in neutron matter as a function of density (n) for the NN and full 3N interactions at N²LO with $R_0 = 1.0$ fm. We use different 3N contact structures: the blue band corresponds to $V_{E\tau}$, the red band to V_{E1} , and the green band to $V_{E\mathcal{P}}$. The green band coincides with the NN 2π -exchange-only (TPE) result because both V_D and V_E vanish in this case. The bands show the theoretical uncertainty, estimated through the expected size of higher-order contributions (From Ref. [47]).

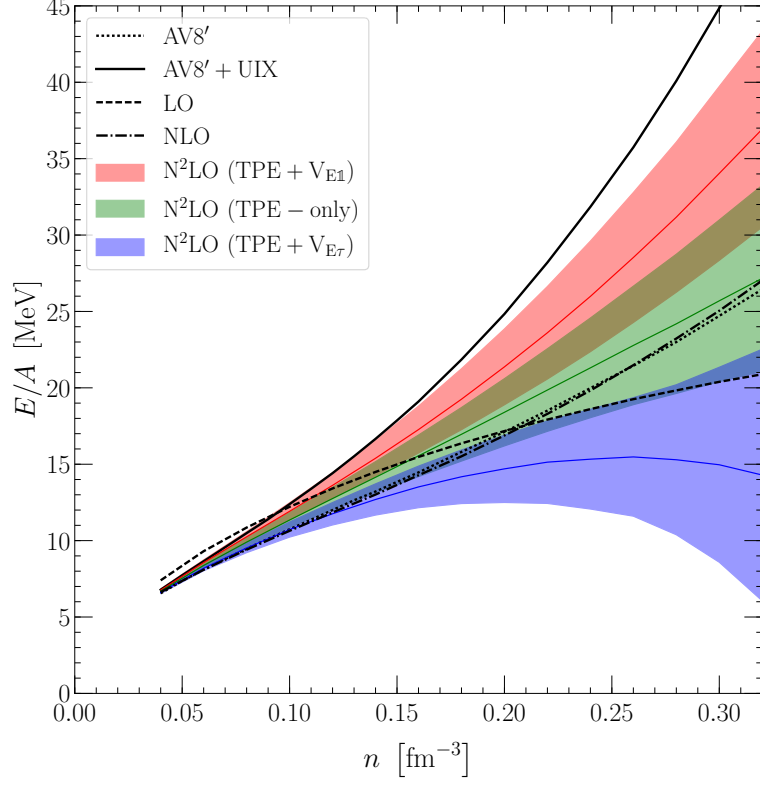


Figure 2.7: Neutron-matter EOSs. n indicates the number density according to the astrophysical notation. We show the AFDMC results for local chiral Hamiltonians with three different 3N short-range operators: TPE-only (green middle band), TPE+ V_{E1} , (red upper band), and TPE+ $V_{E\tau}$ (blue lower band), see Ref. [47] for details. For comparison, we also show results for the phenomenological AV8'+UIX interactions (black line), for AV8' (dotted line), as well as LO (dashed line) and NLO (dashed-dotted line) results for the local chiral interactions of Ref. [45] with $R_0 = 1.0$ fm (from Ref. [99]).

COMPUTATIONAL METHODS

The calculations of ground state properties have been performed using quantum Monte Carlo (QMC) methods, which we present in Section 3.1, and we compute the equation of state for spin unpolarized pure neutron matter and fully spin polarized pure neutron matter Section 4.1.

In general QMC methods model infinite systems as a finite box of fixed size with a finite number of particles, using periodic boundary conditions (PBC). Ideally, the thermodynamical limit is reached for an infinite number of particles. In practice, a finite number of particles is used. In order to reduce finite size effects, the potential is computed by a sum over the first neighbors of a given simulation cell. A further extension allowing to perform calculations with an arbitrary number of particles is to use twist-averaged boundary conditions (TABC), which are presented in Section 3.2. TABC are advantageous for two main reasons. On the one hand, the computational time of the QMC calculations scales exponentially with the number of particles (for Green's function Monte Carlo - GFMC) or polynomially (for auxiliary field diffusion Monte Carlo - AFDMC). On the other hand, with an arbitrary number of particles, we can perform calculations with an arbitrary spin polarization.

The calculations of excited states, especially the response functions for a many-body system, is technically possible. The main issue is the computational cost, which is quite expensive. We chose to treat response functions within mean field approximation, i.e., using simplified energy-density function to reproduce the QMC results. This should be a fair compromise since all the microphysics is included in the QMC calculations with realistic nuclear potentials. This work

follows previous calculations of the longitudinal and transverse response in the isospin channel [100, 101]. Following Hohenberg-Kohn theorem, it is possible to obtain this energy-density function and employing it within the Time Dependent Local Density Approximation (TDLDA, see e.g., [102]). The TDLDA is presented in Section 3.3.

3.1 QUANTUM MONTE CARLO METHODS

Quantum Monte Carlo (QMC) methods have been used over the past decades to describe properties of nuclei as well as nuclear matter [87]. QMC methods are called *ab initio*, which means that for a given potential the Schrödinger equation is solved for the many-body system with controlled approximations, which can be, in principle, systematically improved.

Variational Monte Carlo (VMC) methods were introduced for use with nuclear interactions in the early 1980s [103]. VMC provides an upper-bound of the ground state energy by minimizing the variational parameters present in the wavefunction.

Green's function Monte Carlo (GFMC) method was first introduced by Kalos [104] and then adapted to nuclear physics [42]. This method projects out the ground state with a specific set of quantum numbers. The drawback is that GFMC scales exponentially with the number of particles and thus it has been applied to describe nuclei up to $A = 12$ nucleons [87].

Another projective method is auxiliary field diffusion Monte Carlo (AFDMC), which was introduced in 1999 [105]. Instead of including the full summation of the spin-isospin states, AFDMC uses Hubbard-Stratonovich transformations to sample the spin/isospin degrees of freedom, providing a polynomial scaling. We study pure neutron matter, and we use VMC to minimize first the variational parameters and then to sample the configuration space. We project then to access ground state properties with AFDMC.

3.1.1 Variational Monte Carlo (VMC)

In VMC we have that the variational energy can be computed as the expectation value of a given Hamiltonian H on a trial wave function ψ_T as:

$$E_V = \frac{\langle \psi_T | H | \psi_T \rangle}{\langle \psi_T | \psi_T \rangle} \geq E_0, \quad (3.1)$$

where E_0 is the true ground state energy, and the equality holds only when ψ_T is the ground state wave function. The trial wave function ψ_T is a delicate object: the closer it is to true ground eigenstate, the better variational results we will get. In addition, better variational results lead to shorter imaginary time propagation required to reach the ground state in AFDMC. The trial wave function for neutron matter is usually written as:

$$\psi_T(\mathbf{R}, S) = \phi_S(\mathbf{R}) \phi_A(\mathbf{R}, S), \quad (3.2)$$

where $\mathbf{R} = \{\mathbf{r}_1, \dots, \mathbf{r}_N\}$ and $S = \{s_1, \dots, s_N\}$ stand for the Cartesian and spin coordinates respectively. The ψ_T is written as a product two terms: a symmetric part (S) and an antisymmetric part (A) under exchange of two particles. The global wavefunction is thus antisymmetric, which is the correct symmetry for a fermionic system. The symmetric part of ψ_T is also called the Jastrow factor. It contains all the parameters which have to be optimized in VMC calculations to obtain the lowest variational energy. The Jastrow factor can in general be written as:

$$\phi_S(\mathbf{R}) = \left(\mathcal{S} \prod_{i < j < k} (\mathbb{1} + F_{ijk}) \right) \left(\mathcal{S} \prod_{i < j} F_{ij} \right), \quad (3.3)$$

where \mathcal{S} is the symmetrization operator, F_{ij} is a two-body correlation, and F_{ijk} is a three-body correlation. The most general symmetric two-body correlation can be written as:

$$F_{ij} = \exp \left(\sum_p f_{ij}^p \mathcal{O}_{ij}^p \right), \quad (3.4)$$

where $f_{ij}^p \equiv f^p(r_{ij})$ are the pair correlation functions and are obtained as solution of Schrödinger-like equations in the relative coordinate distance between two particles [87]. The operators \mathcal{O}_{ij}^p are the two-body operators of the nuclear potential employed. The full expression is used in GFMC, but it has an exponential

cost with the number of particles. We approximate this expression restricting to the first six operators of the two-body interaction and expanding the two-body correlation part of Equation (3.3) as:

$$\mathcal{S} \prod_{i<j} F_{ij} \approx \prod_{i<j} f_{ij}^1 \left(\mathbb{1} + \sum_{j<k} \sum_{p=2}^6 f_{ij}^p \mathcal{O}_{ij}^p \right), \quad (3.5)$$

where f_{ij}^1 is the central part of the two-body correlation. The three-body correlation of Equation (3.3) is usually replaced with a sum ($\mathbb{1} + \sum_{i<j<k} F_{ijk}$), which is significantly faster, while variational results are almost as good as the full expression [87]. A good correlation form for spin/isospin dependent three-body correlation function (U_{ijk}) is:

$$F_{ijk} = U_{ijk} = \sum_n \epsilon_n V_{ijk}^n (\alpha_n r_{ij}, \alpha_n r_{ik}, \alpha_n r_{jk}), \quad (3.6)$$

where the terms V_{ijk}^n are the three-body interactions, ϵ_n are potential quenching factors, and α_n are coordinate scaling factors. The final form of the symmetric part of the wavefunction reads:

$$\phi_{\mathcal{S}}(\mathbf{R}) = \prod_{i<j} f_{ij}^1 \prod_{i<j<k} f_{ijk}^{3c} \times \left[\mathbb{1} + \sum_{i<j} \sum_{p=2}^6 f_{ij}^p \mathcal{O}_{ij}^p f_{ij}^{3p} + \sum_{i<j<k} U_{ijk} \right], \quad (3.7)$$

where the three-body spin/isospin independent correlations (f_{ijk}^{3c} and f_{ij}^{3p}) are introduced to reduce the strength of the pair correlation function of the spin- and isospin-dependent components when other particles are nearby. They are defined as:

$$\begin{aligned} f_{ijk}^{3c} &= 1 + q_1^c \mathbf{r}_{ij} \cdot \mathbf{r}_{ik} \mathbf{r}_{ji} \cdot \mathbf{r}_{jk} \mathbf{r}_{ki} \cdot \mathbf{r}_{kj} e^{-q_2^c (r_{ij} + r_{ik} + r_{jk})} \\ f_{ij}^{3p} &= \prod_k \left[1 - q_1^p (1 - \mathbf{r}_{ik} \cdot \mathbf{r}_{jk}) e^{-q_2^p (r_{ij} + r_{ik} + r_{jk})} \right], \end{aligned} \quad (3.8)$$

where $q_{1,2}^{p,c}$ are quenching parameters. We have ~ 40 variational parameters overall. The antisymmetric part $\phi_{\mathcal{A}}(\mathbf{R}, \mathbf{S})$ is written as a Slater determinant of plane waves for infinite neutron matter. The single particle orbitals are written as:

$$\phi_{\alpha}(\mathbf{r}_i, s_i) = e^{i\mathbf{k}_{\alpha} \cdot \mathbf{r}_i} \chi_{s, m_s}(s_i), \quad (3.9)$$

where $\mathbf{k}_{\alpha} = 2\pi/L \cdot (n_{\alpha x}, n_{\alpha y}, n_{\alpha z})$ are the momentum vectors of a system of N neutrons in a periodic box of size L . α is the quantum state, n_x, n_y and n_z are

integer numbers describing the state and $\chi_{s,m_s}(s_i)$ are spinors in general in the proton-neutron-spin up-spin down base. The variational energy can be computed as:

$$\langle H \rangle = \frac{\int d\mathbf{R} P(\mathbf{R}) \frac{H\psi_T(\mathbf{R})}{\psi_T(\mathbf{R})}}{\int d\mathbf{R} P(\mathbf{R})}, \quad (3.10)$$

where $P(\mathbf{R}) = |\psi_T(\mathbf{R})|^2$ and the sum over the spin states is omitted. $P(\mathbf{R})$ can be interpreted as a probability distribution. The integral of Equation (3.10) is evaluated in practice as:

$$\langle E \rangle = \frac{1}{A} \sum_{i=1}^A \frac{\langle \mathbf{R}_i | H | \psi_T \rangle}{\langle \mathbf{R}_i | \psi_T \rangle}, \quad (3.11)$$

where $\langle \mathbf{R} | \psi_T \rangle = \psi_T(\mathbf{R})$ and each configuration \mathbf{R}_i is sampled using Metropolis algorithm [106].

3.1.2 Auxiliary field diffusion Monte Carlo (AFDMC)

Diffusion Monte Carlo (DMC) methods rely on imaginary time propagation to project out the ground state. Starting from a trial wave function $|\psi_T\rangle$, which is usually the result of the VMC calculation, we can evolve and propagate in imaginary time τ to project to the ground state as:

$$|\psi_0\rangle \propto \lim_{\tau \rightarrow \infty} e^{-(H-E_T)\tau} |\psi_T\rangle, \quad (3.12)$$

where E_T is a parameter which controls the normalization. AFDMC methods express the spin/isospin part of the wavefunction in terms of single-particle representations in terms of spinors. Spin/isospin linear operators acting the trial wave function give just a simple rotation of the initial spinors, without generating new amplitudes. Quadratic operators can be linearized by using the Hubbard-Stratonovich transformation:

$$e^{-\frac{1}{2}\lambda\mathcal{O}^2} = \frac{1}{\sqrt{2\pi}} \int dx e^{-\frac{x^2}{2} + \sqrt{-\lambda}x\mathcal{O}}, \quad (3.13)$$

where x are called auxiliary fields. The propagation in imaginary time (for simplicity neglecting spin/isospin components) can be written as:

$$\langle \mathbf{R}' | \psi(\tau) \rangle = \int d\mathbf{R} G(\mathbf{R}', \mathbf{R}, \tau) \langle \mathbf{R} | \psi_T(0) \rangle, \quad (3.14)$$

where the propagator (or Green's function) G is defined as the matrix element between the two points \mathbf{R} and \mathbf{R}' as:

$$G(\mathbf{R}', \mathbf{R}, \tau) = \langle \mathbf{R}' | e^{-(H-E_T)\tau} | \mathbf{R} \rangle . \quad (3.15)$$

The true ground state is approached by $\langle \mathbf{R}' | \psi(\tau) \rangle$ for large imaginary time τ . The propagator $G(\mathbf{R}', \mathbf{R}, \tau)$ can not be directly computed for arbitrary τ . The calculation is tractable for small imaginary time $\delta\tau = \tau/N$, with N large, and the full propagation is then recovered as a product of short-time propagators $G(\mathbf{R}', \mathbf{R}, \delta\tau)$. The equality holds for small values of the time step $\delta\tau$, and the exact result is obtained extrapolating for $\delta\tau \rightarrow 0$. The short time propagator, using the Trotter-Suzuki expansion to order $\delta\tau^3$ [107], can be written as:

$$\begin{aligned} G(\mathbf{R}', \mathbf{R}, \delta\tau) &\equiv \langle \mathbf{R}' | e^{-(H-E_T)\delta\tau} | \mathbf{R} \rangle \\ &\approx \langle \mathbf{R}' | e^{-(V-E_T)\frac{\delta\tau}{2}} e^{-T\delta\tau} e^{-(V-E_T)\frac{\delta\tau}{2}} | \mathbf{R} \rangle , \end{aligned} \quad (3.16)$$

where T and V are the nonrelativistic kinetic energy and the nuclear potential respectively. A full review on how each term of the potentials can be included in the propagator is reported in Ref. [86] for AV8'+UIX and Ref. [108] for local chiral interactions. For the case of pure neutron systems, it is possible to include fully in AFDMC spin-orbit interactions and three-body forces [84, 90].

The sampling of the spatial and spin/isospin configurations of the propagator is usually not very efficient, so importance sampling techniques are implemented. The idea is to introduce a guidance function ψ_G and sample the modified propagator:

$$G(\mathbf{R}', \mathbf{R}, S'(X), S, \delta\tau) \frac{\langle \psi_G | \mathbf{R}' S'(X) \rangle}{\langle \psi_G | \mathbf{R} S \rangle} , \quad (3.17)$$

where X are auxiliary fields from Gaussian distributions. The four weights corresponding to the sampling of a coordinate displace $\Delta\mathbf{R}$, and of the auxiliary fields X , which are given by:

$$w_i = \frac{\langle \psi_G | \mathbf{R} \pm \Delta\mathbf{R} S'(\pm X) \rangle}{\langle \psi_G | \mathbf{R} S \rangle} \exp[-V_{SI}(\mathbf{R})\delta\tau] , \quad (3.18)$$

where V_{SI} is the spin/isospin-independent part of the interaction. The total weight W of the new configuration is given by the average of the four weights. The total weight W is used for branching as in the standard DMC method [87].

The expectation values of the observables \mathcal{O} which commute with the Hamiltonian are calculated from the sampled configurations $\mathbf{R}_i S_i$ as:

$$\langle \mathcal{O}(\tau) \rangle = \frac{\sum_i \frac{\langle \mathbf{R}_i S_i | \mathcal{O} | \psi_T \rangle}{W} \frac{W}{\langle \mathbf{R}_i S_i | \psi_T \rangle}}{\sum_i \frac{W}{\langle \mathbf{R}_i S_i | \psi_T \rangle}}. \quad (3.19)$$

For other observables the expectation values can be computed as two times the DMC expectation value minus the VMC one.

The denominator of Equation (3.19) quickly reaches zero for real weights W and complex wavefunction ψ_T . This is yet another manifestation of the well-known sign problem in DMC methods. To avoid it, we use a constrained path approximation with complex wavefunctions [109], although the calculated energy is not necessarily an upper bound to the correct ground-state energy. The idea is to limit the original propagation to regions where the propagated and trial wave functions have a positive overlap, assigning zero weight to moves that change the sign of the real part of the wavefunction.

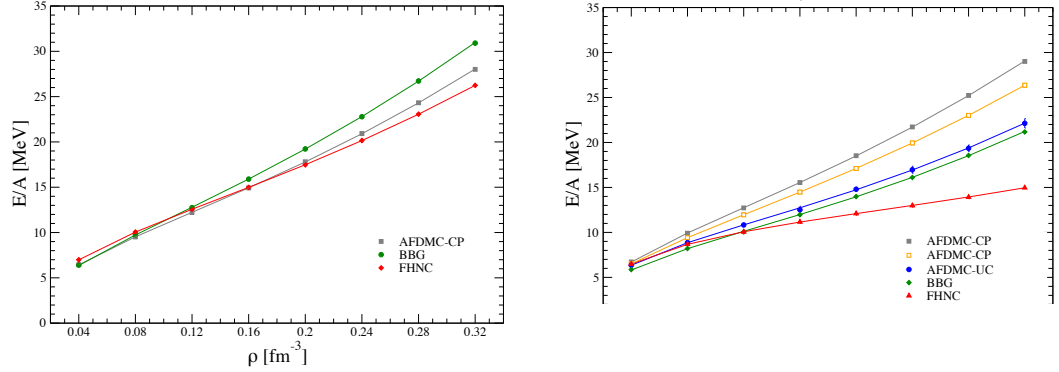


Figure 3.1: Energy per particle of PNM as a function of density for the AV6' (left) and AV8' (right) calculated with the Brueckner-Bethe-Goldstone (BBG, green diamonds), Fermi hypernetted chain/single-operator chain (FHNC/SOC, red triangles), AFDMC with constrained (AFDMC-CP, grey squares) and unconstrained evolution (AFDMC-UC, solid blue points) many-body approaches (from Ref. [110]). Results for AFDMC-CP in yellow squares refer to results of Ref. [111].

The correct ground state might still be achieved by removing the constraint on the evolution and extracting information on the unconstrained evolution before

the signal-to-noise ratio goes to zero. This procedure is quite computational time expensive, and we did not implement it in our calculations. The corrections are expected to be small in pure neutron matter, but recent findings [110] showed the importance of also doing the unconstrained evolution, as reported in Figure 3.1. The calculations have been performed only with two-body interactions for pure neutron matter for 14 and 38 neutrons with periodic boundary conditions (PBC). However, the systematic error coming from the constrained imaginary-time propagation seems to be related to the spin-orbit part of the potentials.

3.2 INFINITE MATTER AND BOUNDARY CONDITIONS

Infinite neutron matter is modeled as N neutrons in a box of fixed size L , and periodic boundary conditions (PBC) are applied at the borders. With PBC, a particle that exits the box on a given direction is reintroduced in the same box from the other side. Wavefunctions are chosen accordingly to describe such a symmetry:

$$\psi(\mathbf{r}_1 + L\hat{\mathbf{x}}, \mathbf{r}_2, \dots) = \psi(\mathbf{r}_1, \mathbf{r}_2, \dots) \quad (3.20)$$

As explained in Section 3.1 our wavefunction is a Jastrow factor, where all the information on the nuclear interacting part are encoded, multiplied by a Slater determinant of plane waves. Plane waves are the solutions of the Schrödinger equation for the system of non-interacting fermions (free Fermi gas). In general we can allow particles to pick up a phase θ when they wrap around the boundaries as:

$$\psi(\mathbf{r}_1 + L\hat{\mathbf{x}}, \mathbf{r}_2, \dots) = e^{i\theta_x} \psi(\mathbf{r}_1, \mathbf{r}_2, \dots) . \quad (3.21)$$

For a twist angle $\theta = 0$ this expression reduces to the PBC, while taking general twist angle $\theta \neq 0$ is called twisted boundary condition. Twist-averaged boundary conditions (TABC) were introduced for QMC methods by Lin *et al.* in 2001 [112]. With this trick, we reduce finite-size shell effects, averaging over the twist angle. Each dimension can have an independent twist angle, so instead of a single twist, we have a twist vector. The equilibrium properties have to be periodic in the twist

angle ($F(\theta_i + 2\pi) = F(\theta_i)$). Due to this symmetry, the values on each component of the twist angle θ_i restrict to:

$$-\pi \ll \theta_i \leq \pi . \quad (3.22)$$

In the first part of this section, we present the 2D case for non-interacting fermions, to better visualize the effects of the twist angles. To respect the twisted boundary conditions, the wave vectors \mathbf{k}_n of the plane waves have to satisfy:

$$\mathbf{k}_n = (2\pi\mathbf{n} + \theta) / L , \quad (3.23)$$

where \mathbf{n} is an integer vector.

The energy of each state is $E_n = (\hbar^2/2m)\mathbf{k}_n^2$, and the ground state of the system is obtained by filling the lowest energy states. The effect of the spin for spin 1/2 fermions is to double the degeneracy of each energy level. In Figure 3.2 we report the momentum distribution of 13 spinless particles in a 2D square of size $L = 2\pi$.

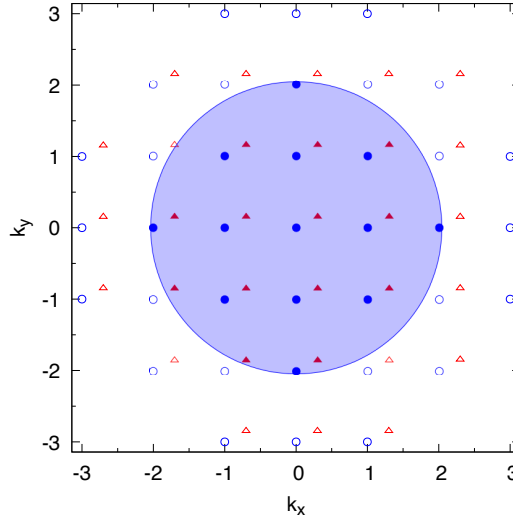


Figure 3.2: Momentum distribution for 13 spinless fermions in a 2D square with side $L = 2\pi$. The occupied states (closed symbols) and empty states (open symbols) with zero twist are shown with circles for PBC and for a twist equal to $2\pi(0.3, 0.15)$ with triangles. The circle shows the infinite system Fermi surface (readapted and modified from Ref. [112]).

The difference between the energy value of a given twist and the exact value of the free infinite system is plotted in Figure 3.3 for each twist in a non-interacting

system of spin-1/2 fermions. Even averaging over all possible twist angles, we can see that the energy contribution patterns are an intrinsic property of the system. They depend on the number of particles, the spin degeneracy, and the dimensionality of the system.

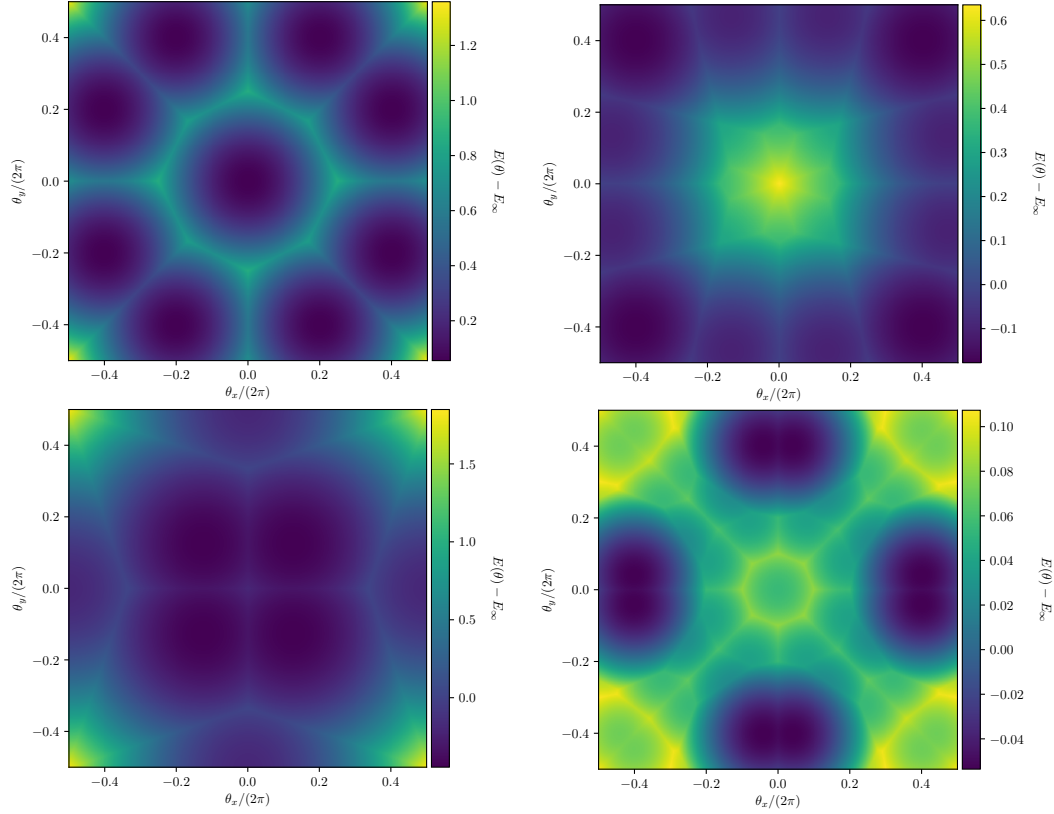


Figure 3.3: Difference between the energy of each twist and the energy of the infinite system for a 2D spin 1/2 non-interacting fermionic system at saturation density $\rho_0 = 0.16 \text{ fm}^{-3}$. The colorbar indicates the contribution of each 2D twist vector plotted in the xy plane. The number of particles is 10, 16, 30, 50 in top-left, bottom-left, top-right, and bottom-right panels respectively.

The contributions of the twist angles to the energy decrease rapidly when increasing the number of particles, indicating that the finite-size effects are less and less important, and we are approaching the thermodynamical limit. The same behavior can also be seen for the 3D case in Figure 3.4, where we plot the energy of the free Fermi gas for spin 1/2 particles at saturation density in function of the total number of particles.

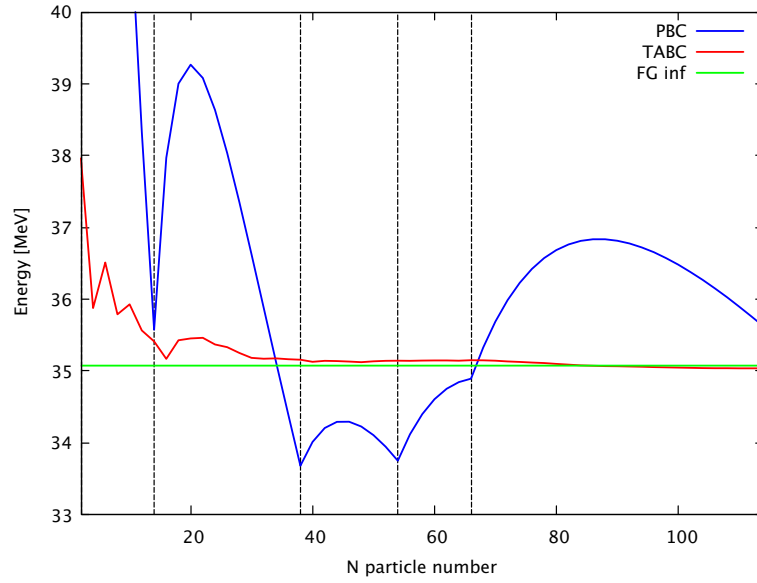


Figure 3.4: Energy per particle in function of the number of particles for the spin 1/2 non interacting 3D system at saturation $\rho = 0.16$. The dashed lines indicates the closed shell configurations, which are at $N = 14, 38, 54, 66, 114, \dots$. Blue and red solid lines indicate the results using PBC and TABC respectively.

The bumps present in the calculation of the energy with the PBC indicate the presence of a closed-shell configuration, i.e., a state that has degenerate energy levels either all filled or all empty. In contrast, the convergence to the infinite system result using TABC is much smoother, and good results are already obtained for $N \geq 30$. TABC results were computed averaging over 2×10^6 twist vectors randomly generated in the region defined by Equation (3.22). QMC calculations with PBC are performed with closed-shell states (i.e., with a good symmetry). Usually, 66 particles are taken to calculate PNM properties because this is the closed shell configuration giving the value closest to the infinite system, still with a reasonable number of particles in terms of required computational time. Using TABC, we can reduce the number of particles at the cost of sampling the twist angles. The convergence to the infinite system as a function of the number of particles is much faster and smoother. Also, an arbitrary number of spin-up and spin-down particles can be used. In principle, one would like to reach the thermodynamic limit, but the computational time required for a QMC calculation with nuclear

interaction limits the number of particles to $N \sim 100$. For pure neutron matter within the AFDMC method, TABC were already introduced in Ref. [90]. We implemented the TABC in the new code to study partially spin-polarized systems and compute the magnetic susceptibility directly, as reported in Section 4.5. For now, we report the results for the case of pure neutron matter at saturation density with the phenomenological potential AV8'+UIX in Figure 3.5.

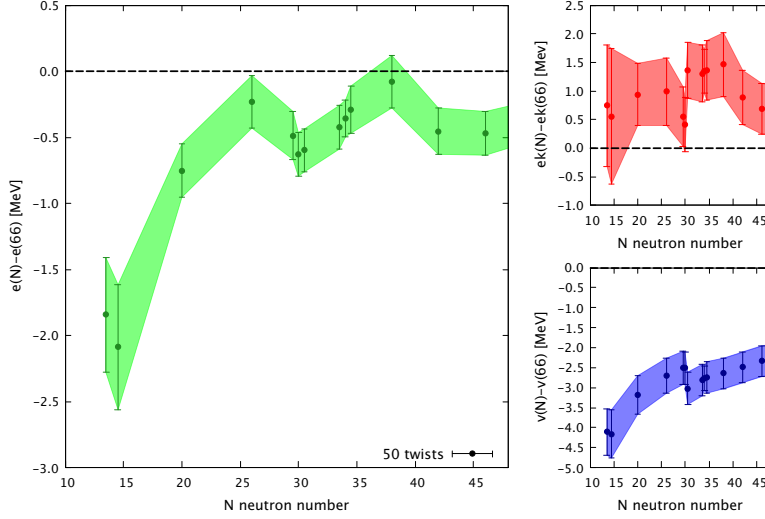


Figure 3.5: The energy per particle for a fixed number of neutrons ($e(N)$) minus the energy of system with 66 neutrons ($e(66)$, which is assumed to be the result for the infinite system) is plotted in function of the neutron number N . We performed the AFDMC calculations at saturation density for pure neutron matter interacting with the AV8'+UIX potential. More details on the calculation are given in the text.

We use 50 arbitrary twist vectors and perform independent AFDMC calculations. The results are the average on the different runs. To check the robustness of our simulation, in some cases, we perform more simulation, sampling new twist vectors for each run. The results for the same particle number but different sets of twist vectors are plotted slightly shifted with respect to the correct particle number for clarity. We performed calculations for $N = 14, 20, 26, 30, 34, 38, 42, 46, 66$. In contrast to the non-interacting system, the exact result for infinite matter is not known. We assumed that for 66 neutrons, the thermodynamical limit is already reached. We also report the results for kinetic and potential energy separately.

Since these two quantities are not observables, they depend on the specific choice of the optimized parameters of the Jastrow factor of the wavefunction. This can be seen for the different calculations performed at $N = 30$. While the total energy per particle is clearly in agreement, the kinetic and potential energy are barely within errorbars. In fact, we used the optimized parameters computed for the closed shell configurations at 14 and 38 neutrons when $14 \leq N \leq 30$ and $30 \leq N \leq 46$ respectively. For $N = 66$, the parameters are optimized for this closed-shell configuration instead.

3.3 TIME DEPENDENT LOCAL SPIN DENSITY APPROXIMATION

In this section, we present the derivation of the Time Dependent Local Spin Density Approximation (TDLSDA). Within this scheme, we compute the response functions to density and spin density excitations. The results are reported in Section 4.2. The solution of the many-body Schrödinger equation for N neutrons in a volume V , in the mean field approximation, is assumed to be the product of two Slater determinants, one for the N_\uparrow spin-up neutrons and one for the N_\downarrow spin-down neutrons:

$$\psi(\mathbf{r}_1 \dots \mathbf{r}_N) = \det[\phi_i^\uparrow(\mathbf{r}_j)] \det[\phi_i^\downarrow(\mathbf{r}_j)] , \quad (3.24)$$

where the indices i, j run from 1 to N_\uparrow and N_\downarrow respectively. The spin-up and spin-down neutron densities are defined as:

$$\rho_\sigma = \sum_i |\varphi_i^\sigma(\mathbf{r})|^2 , \quad (3.25)$$

where $\sigma = \uparrow(\downarrow)$ stands for spin-up (spin-down) neutrons, and the sum runs over all the occupied states. We recall that in the local density (mean field) approximation, the energy as a function of the density ρ and the spin polarization ξ can be generically written as:

$$E(\rho, \xi) = T_0(\rho, \xi) + \int \epsilon_V(\rho, \xi) \rho \, d\mathbf{r} , \quad (3.26)$$

where T_0 is the non-relativistic kinetic energy. By minimizing the energy functional with respect to the single particle wavefunction φ_i^σ , one obtains the set of self-consistent, stationary Kohn-Sham equations for spin-up and spin-down neutrons wave functions ($\hbar = c = 1$ hereafter):

$$\left[-\frac{1}{2m} \nabla_{\mathbf{r}}^2 + v(\rho(\mathbf{r}), \xi(\mathbf{r})) + w(\rho(\mathbf{r}), \xi(\mathbf{r})) \sigma_z + \frac{1}{2} \omega_c \sigma_z \right] \varphi_i^\sigma(\mathbf{r}) = \epsilon_{i,\sigma} \varphi_i^\sigma(\mathbf{r}) . \quad (3.27)$$

The effective potentials are defined as the derivatives of the functional with respect to the total density and the magnetization:

$$v(\mathbf{r}) = \frac{\partial \rho \epsilon_V [\rho(\mathbf{r}), \xi]}{\partial \rho(\mathbf{r})} , \quad w(\mathbf{r}) = \frac{\partial \epsilon_V [\rho(\mathbf{r}), \xi]}{\partial \xi(\mathbf{r})} . \quad (3.28)$$

The term containing ω_c is needed to induce a partial (or total) magnetization of neutrons, mimicking the presence of an external (magnetic) field. The value of ω_c is related to the desired asymmetry $\bar{\xi}$ of the system by requiring that the variation of the expectation energy with respect to ξ at $\bar{\xi}$ be zero. The result of the minimization yields:

$$\omega_c = \bar{\xi} \frac{1 + \frac{3}{2\epsilon_F} \left. \frac{\partial w}{\partial \xi} \right|_{\bar{\xi}}}{\frac{3N}{4\epsilon_F}} , \quad (3.29)$$

where $\epsilon_F = k_F^2/2m$ is the Fermi energy, with the Fermi momentum k_F and the spin-up and spin-down neutron momenta given by $k_F^\uparrow = k_F(1 + \xi)^{1/3}$ and $k_F^\downarrow = k_F(1 - \xi)^{1/3}$, respectively. We briefly review the derivation of the TDLSDA in the longitudinal and in the transverse channels.

3.3.1 Longitudinal channel

The longitudinal channel describes the response to a time-dependent field along the \mathbf{r} direction:

$$F^z = \sum_{k=1}^N f(\mathbf{r}_k) \lambda_\sigma^k , \quad (3.30)$$

where:

$$f(\mathbf{r}) = \exp [i(\mathbf{q} \cdot \mathbf{r} - \omega t)] + \exp [-i(\mathbf{q} \cdot \mathbf{r} - \omega t)] ,$$

and $\lambda_\sigma^k = \lambda$ for a *density excitation* and $\lambda_\sigma^k = \lambda \eta_\sigma$, η_σ is the eigenvalue of the σ_z operator ($\eta = 1$ for spin-up and $\eta = -1$ for spin down neutrons) for *vector-*

density excitations, q is the momentum and ω is the energy. The corresponding time dependent Kohn-Sham equations reads:

$$i \frac{\partial}{\partial t} \varphi_i^\sigma(\mathbf{r}, t) = \left\{ -\frac{1}{2m} \nabla_{\mathbf{r}}^2 + v[\rho_\uparrow(\mathbf{r}, t), \rho_\downarrow(\mathbf{r}, t)] + w[\rho_\uparrow(\mathbf{r}, t), \rho_\downarrow(\mathbf{r}, t)] \eta_\sigma + \lambda_\sigma \left[e^{i(\mathbf{q}\cdot\mathbf{r}-\omega t)} + e^{-i(\mathbf{q}\cdot\mathbf{r}-\omega t)} \right] \right\} \varphi_i^\sigma(\mathbf{r}, t). \quad (3.31)$$

For this case we use $\omega_c = 0$, since longitudinal excitations are not directly coupled to the neutron spin. The solutions linearized in the neutron density oscillations induced by external fields are given by:

$$\begin{aligned} \rho_\uparrow(\mathbf{r}, t) &= \rho_\uparrow + \delta\rho_\uparrow(\mathbf{r}, t), \\ \rho_\downarrow(\mathbf{r}, t) &= \rho_\downarrow + \delta\rho_\downarrow(\mathbf{r}, t), \end{aligned} \quad (3.32)$$

where the time dependent density is assumed to be proportional to the external perturbation:

$$\begin{aligned} \delta\rho_\uparrow(\mathbf{r}, t) &= \delta\rho_\uparrow(e^{i(\mathbf{q}\cdot\mathbf{r}-\omega t)} + e^{-i(\mathbf{q}\cdot\mathbf{r}-\omega t)}), \\ \delta\rho_\downarrow(\mathbf{r}, t) &= \delta\rho_\downarrow(e^{i(\mathbf{q}\cdot\mathbf{r}-\omega t)} + e^{-i(\mathbf{q}\cdot\mathbf{r}-\omega t)}). \end{aligned} \quad (3.33)$$

Following the derivation in Ref. [100], the density-density response (per unit volume) is then given by:

$$\frac{\chi^s(q, \omega)}{V} = \frac{(\delta\rho_\uparrow + \delta\rho_\downarrow)}{\lambda} \equiv \frac{\chi^\uparrow(q, \omega) + \chi^\downarrow(q, \omega)}{V}, \quad (3.34)$$

and the vector density-vector density response is:

$$\frac{\chi^v(q, \omega)}{V} = \frac{(\delta\rho_\uparrow - \delta\rho_\downarrow)}{\lambda} \equiv \frac{\chi^\uparrow(q, \omega) - \chi^\downarrow(q, \omega)}{V}. \quad (3.35)$$

In order to determine the expression of the response function, we can explicitly compute the total self-consistent potentials in the Kohn-Sham equations. At first order in $\delta\rho_\sigma$ this is given by:

$$\begin{aligned} V_{KS}[\rho_\uparrow(\mathbf{r}, t), \rho_\downarrow(\mathbf{r}, t)] &\equiv v[\rho_\uparrow, \rho_\downarrow] + w[\rho_\uparrow, \rho_\downarrow] = \\ &= V_{KS}(\rho_\uparrow, \rho_\downarrow) + \left. \frac{\partial V_{KS}}{\partial \rho(\mathbf{r}, t)} \right|_{\rho_\uparrow, \rho_\downarrow} \delta\rho_\uparrow(\mathbf{r}, t) + \left. \frac{\partial V_{KS}}{\partial \rho(\mathbf{r}, t)} \right|_{\rho_\uparrow, \rho_\downarrow} \delta\rho_\downarrow(\mathbf{r}, t), \end{aligned} \quad (3.36)$$

which gives the following expression for the Kohn-Sham equations:

$$i \frac{\partial}{\partial t} \varphi_i^\uparrow(\mathbf{r}, t) = \left\{ -\frac{1}{2m} \nabla_{\mathbf{r}}^2 + \text{const.} + [\delta\rho_\uparrow V_{\uparrow,\uparrow} + \delta\rho_\downarrow V_{\uparrow,\downarrow} + \lambda] \right. \\ \left. \times (e^{i(\mathbf{q}\cdot\mathbf{r}-\omega t)} + e^{-i(\mathbf{q}\cdot\mathbf{r}-\omega t)}) \right\} \varphi_i^\uparrow(\mathbf{r}, t), \quad (3.37)$$

$$i \frac{\partial}{\partial t} \varphi_i^\downarrow(\mathbf{r}, t) = \left\{ -\frac{1}{2m} \nabla_{\mathbf{r}}^2 + \text{const.} + [\delta\rho_\uparrow V_{\uparrow,\downarrow} + \delta\rho_\downarrow V_{\downarrow,\uparrow} \pm \lambda] \right. \\ \left. \times (e^{i(\mathbf{q}\cdot\mathbf{r}-\omega t)} + e^{-i(\mathbf{q}\cdot\mathbf{r}-\omega t)}) \right\} \varphi_i^\downarrow(\mathbf{r}, t),$$

where the constant term is the Kohn-Sham potential evaluated at the density and magnetization of the homogeneous neutron matter under consideration. Note that the \pm in the second equation of Equation (3.37) comes from the different channels: plus for density excitations, while minus for vector-density excitations. This fact makes the solutions of the linearized dynamic equations formally equal to those of the free Fermi gas. As a consequence, the response function of the system will be the one for the free system $\chi_0(q, \omega) = \chi_0^\uparrow(q, \omega) + \chi_0^\downarrow(q, \omega)$, where:

$$\chi_0^\uparrow(q, \omega) = \frac{V \delta\rho_\uparrow}{\lambda'_\uparrow}, \quad (3.38) \\ \chi_0^\downarrow(q, \omega) = \frac{V \delta\rho_\downarrow}{\lambda'_\downarrow}.$$

The effective strength $\lambda'_{\sigma'}$, defined as:

$$\lambda'_\uparrow = \delta\rho_\uparrow V_{\uparrow,\uparrow} + \delta\rho_\downarrow V_{\uparrow,\downarrow} + \lambda, \quad (3.39) \\ \lambda'_\downarrow = \delta\rho_\uparrow V_{\downarrow,\uparrow} + \delta\rho_\downarrow V_{\downarrow,\downarrow} \pm \lambda$$

includes terms depending on the interaction. The mean field potentials $V_{\sigma,\sigma'}$ are obtained through the derivatives of $v + \eta_\sigma w$ with respect to ρ_σ :

$$V_{\uparrow,\uparrow} = \left. \frac{\partial(v+w)}{\partial\rho_\uparrow(\mathbf{r},t)} \right|_{\rho_\uparrow,\rho_\downarrow} = \left(\frac{\partial}{\partial\rho} + \frac{1}{\rho} \frac{\partial}{\partial\xi} \right) (v+w) \Big|_{\rho,\xi}, \\ V_{\uparrow,\downarrow} = \left. \frac{\partial(v+w)}{\partial\rho_\downarrow(\mathbf{r},t)} \right|_{\rho_\uparrow,\rho_\downarrow} = \left(\frac{\partial}{\partial\rho} - \frac{1}{\rho} \frac{\partial}{\partial\xi} \right) (v+w) \Big|_{\rho,\xi}, \\ V_{\downarrow,\uparrow} = \left. \frac{\partial(v-w)}{\partial\rho_\uparrow(\mathbf{r},t)} \right|_{\rho_\uparrow,\rho_\downarrow} = \left(\frac{\partial}{\partial\rho} + \frac{1}{\rho} \frac{\partial}{\partial\xi} \right) (v-w) \Big|_{\rho,\xi}, \\ V_{\downarrow,\downarrow} = \left. \frac{\partial(v-w)}{\partial\rho_\downarrow(\mathbf{r},t)} \right|_{\rho_\uparrow,\rho_\downarrow} = \left(\frac{\partial}{\partial\rho} - \frac{1}{\rho} \frac{\partial}{\partial\xi} \right) (v-w) \Big|_{\rho,\xi}.$$

Comparing Equations (3.34) and (3.35), and Equation (3.38) we see that:

$$\begin{aligned}\lambda\chi^\uparrow(q, \omega) &= \lambda'_\uparrow\chi_0^\uparrow(q, \omega) = V\delta\rho_\uparrow, \\ \lambda\chi^\downarrow(q, \omega) &= \lambda'_\downarrow\chi_0^\downarrow(q, \omega) = V\delta\rho_\downarrow.\end{aligned}\quad (3.40)$$

The solution of these equations, finally gives the TDLSDA response functions in the longitudinal channel:

$$\begin{aligned}\chi^s(q, \omega) &= V\frac{\chi_0^\uparrow[V - (V_{\downarrow\downarrow} - V_{\uparrow\downarrow})\chi_0^\downarrow] + \chi_0^\downarrow[V - (V_{\uparrow\uparrow} - V_{\downarrow\uparrow})\chi_0^\uparrow]}{(V - V_{\downarrow\downarrow}\chi_0^\downarrow)(V - V_{\uparrow\uparrow}\chi_0^\uparrow) - V_{\uparrow\downarrow}\chi_0^\uparrow V_{\downarrow\uparrow}\chi_0^\downarrow}, \\ \chi^v(q, \omega) &= V\frac{\chi_0^\uparrow[V - (V_{\downarrow\downarrow} + V_{\uparrow\downarrow})\chi_0^\downarrow] + \chi_0^\downarrow[V - (V_{\uparrow\uparrow} + V_{\downarrow\uparrow})\chi_0^\uparrow]}{(V - V_{\downarrow\downarrow}\chi_0^\downarrow)(V - V_{\uparrow\uparrow}\chi_0^\uparrow) - V_{\uparrow\downarrow}\chi_0^\uparrow V_{\downarrow\uparrow}\chi_0^\downarrow}.\end{aligned}\quad (3.41)$$

We should keep in mind that the TDLSDA is valid only in the low- q , low- ω limits. For consistency, we use the expressions of the free response functions χ_0^\uparrow and χ_0^\downarrow in the same regime. Their explicit form, which holds for $q \rightarrow 0$ and $s = \omega/(qv_F)$ fixed, is:

$$\chi_0^{\uparrow,\downarrow}(\mathbf{q}, \omega) = -V\nu^{\uparrow,\downarrow} \left[1 + \frac{s}{2(1 \pm \xi)^{1/3}} \ln \frac{s - (1 \pm \xi)^{1/3}}{s + (1 \pm \xi)^{1/3}} \right], \quad (3.42)$$

where \uparrow (\downarrow) reads with $+$ ($-$), $\nu^{\uparrow,\downarrow} = mk_F^{\uparrow,\downarrow}/(2\pi^2) = mk_F(1 \pm \xi)^{1/3}/(2\pi^2)$, $k_F = (3\pi^2\rho)^{1/3}$ and $s = \omega/(qv_F)$. By defining:

$$\Omega^{\uparrow,\downarrow} = \left[1 + \frac{s}{2(1 \pm \xi)^{1/3}} \ln \frac{s - (1 \pm \xi)^{1/3}}{s + (1 \pm \xi)^{1/3}} \right], \quad (3.43)$$

we can rewrite the density-density and vector-density/vector-density response functions as:

$$\frac{\chi^{s,v}}{Nm/(2k_F^2)} = -3 \frac{(1+\xi)^{1/3}\Omega^\uparrow [1+(G_{\downarrow\uparrow}(\frac{1-\xi}{1+\xi})^{1/6}G_{\uparrow\downarrow})\Omega^\downarrow] + (1-\xi)^{1/3}\Omega^\downarrow [1+(G_{\uparrow\downarrow}(\frac{1+\xi}{1-\xi})^{1/6}G_{\downarrow\uparrow})\Omega^\uparrow]}{(1+G_{\downarrow\downarrow}\Omega^\downarrow)(1+G_{\uparrow\uparrow}\Omega^\uparrow) - G_{\uparrow\downarrow}^2\Omega^\uparrow\Omega^\downarrow}, \quad (3.44)$$

where $G_\uparrow = \nu_\uparrow V_{\uparrow,\uparrow}$, $G_\downarrow = \nu_\downarrow V_{\downarrow,\downarrow}$ and $G_{\uparrow\downarrow} = \sqrt{\nu_\uparrow\nu_\downarrow} V_{\uparrow,\downarrow}$. The G parameters can be related to the F_0 Landau parameters, since they share the same derivation, but considering the fact that multiple excitation channels are now possible. Simplifying Equation (3.44) in the fully polarized and unpolarized neutron matter limits,

this link is even more evident. The response functions for the unpolarized system ($\chi_0^\uparrow = \chi_0^\downarrow = \chi_0$) read:

$$\chi^s(q, \omega) = \frac{\chi_0(q, \omega)}{1 - \left. \frac{\partial v}{\partial \rho} \right|_{\rho, \xi=0} \frac{\chi_0(q, \omega)}{V}} \quad \chi^v(q, \omega) = \frac{\chi_0(q, \omega)}{1 - \left. \frac{1}{\rho} \frac{\partial w}{\partial \xi} \right|_{\rho, \xi=0} \frac{\chi_0(q, \omega)}{V}}, \quad (3.45)$$

while for the fully polarized system, where $\chi_0^\downarrow = 0$, we obtain:

$$\chi^s(q, \omega) = \chi^v(q, \omega) = \frac{\chi_0^\uparrow(q, \omega)}{1 - V_{\uparrow, \uparrow} \frac{\chi_0^\uparrow(q, \omega)}{V}}, \quad (3.46)$$

The resulting expressions of Equations (3.45) and (3.46) are equivalent to those that could be derived by the Landau Fermi liquids theory considering as quasi-particles spin and density elementary excitations (as combinations of $\delta\rho_\uparrow$ and $\delta\rho_\downarrow$). The expressions for the response functions obtained in Equations (3.45) and (3.46) are also analogous to the ones derived within the Random Phase Approximation (RPA). The difference is the nature of the potential term entering in these equations. Within TDLSDA the potential is obtained in an effective way from an energy-density functional fitted to the EOS, while in the RPA approach it is obtained as the Fourier transform of the bare potential.

An additional comment regarding the choice of potential form is needed. While in approximations such as RPA and Landau Fermi liquid theory, the potential reflects the standard terms present in the nuclear interaction, these features are mainly captured by the density functional in an effective way within TDLSDA. As an example, the tensor term is not explicitly expressed in TDLSDA. However, its nature is still partially captured by the simple choice of the energy-density functional, since it is fitted to EOSs obtained from ab initio calculations with realistic nuclear interactions (including the tensor force).

The imaginary part of Equation (3.44) provides the strength of the single particle excitations:

$$S(q, \omega) = -\frac{1}{\pi} \text{Im}[\chi^{s,v}(q, \omega)]. \quad (3.47)$$

3.3.2 Transverse channel

The derivation of the response function in the transverse channel was first done by Rajagopal [113]. It is similar to that used in the longitudinal channel, and it has also been applied to quantum dots [114, 115]. The excitation operator has the same structure as that of Equation (3.30), but the constraint now is that $\Delta S_z = \pm 1$, thereby defining:

$$F^\pm = \sum_k f(\mathbf{r}_k) \sigma_k^\pm. \quad (3.48)$$

In the $\Delta S_z = \pm 1$ channel, given the magnetization m of the system ($\xi = m/\rho$), the static local spin density approximation (LSDA) equations (3.27) can be rewritten as:

$$\left[-\frac{1}{2} \nabla_{\mathbf{r}}^2 + \frac{1}{2} \omega_c \sigma_z + v(\mathbf{r}) + \mathcal{W} \mathbf{m} \cdot \boldsymbol{\sigma} \right] \varphi_i^\sigma(\mathbf{r}) = \varepsilon_{i,\sigma} \varphi_i^\sigma(\mathbf{r}), \quad (3.49)$$

where \mathbf{m} is the *spin polarization vector*. The interaction/correlation energy only depends on ρ and $|\mathbf{m}|$, i.e. $\epsilon_V = \epsilon_V[\rho, |\mathbf{m}|]$ so that the spin-dependent interaction/correlation potential w in equation (3.28) can be written as:

$$\mathcal{W} \mathbf{m} = w[\rho, |\mathbf{m}|] \mathbf{m}/|\mathbf{m}|, \quad (3.50)$$

where:

$$w[\rho, |\mathbf{m}|] = \partial \epsilon_V[\rho, |\mathbf{m}|] / \partial |\mathbf{m}|, \quad (3.51)$$

and $\mathcal{W}[\rho, |\mathbf{m}|] \equiv w[\rho, |\mathbf{m}|] / |\mathbf{m}|$. Defining the spherical components \pm of the vectors \mathbf{m} and $\boldsymbol{\sigma}$, it is possible to express the z component of the magnetization dependent potential as:

$$w \sigma_z \rightarrow \mathcal{W}[\rho, |\mathbf{m}|] [m_z \sigma_z + 2(m_+ \sigma_- + m_- \sigma_+)]. \quad (3.52)$$

In the static case, the inclusion of the densities m_+ and m_- makes no difference since they vanish identically. The situation is different when the system interacts with a time-dependent field that couples to the nucleon spin through the general term:

$$\mathbf{F} \cdot \boldsymbol{\sigma} = F_z \sigma_z + 2(F_+ \sigma_- + F_- \sigma_+). \quad (3.53)$$

As a consequence, the interaction Hamiltonian causing transverse spin excitations, may be written as:

$$H_{\text{int}} \sim \sigma_f^- e^{-i\omega t} + \sigma_f^+ e^{i\omega t}. \quad (3.54)$$

H_{int} causes non-vanishing variations in the magnetization components δm_+ and δm_- which, in turn, generate at first-order perturbation theory a variation in the mean field potential. Following the steps described in Ref. [101] the TDLSDA response function is given by (once again V is the volume):

$$\chi_t(q, \omega) = \frac{\chi_t^0(q, \omega)}{1 - \frac{2}{V} \mathcal{W}(\rho, m) \chi_t^0(q, \omega)}, \quad (3.55)$$

where $\chi_t^0(q, \omega)$ is the free transverse linear response. In the $qv_F \ll \epsilon_F$ limit, where $v_F = k_F/m$ is the Fermi velocity, it is given by:

$$\frac{\chi_t^0(q, \omega)}{V} = -\frac{3}{4} \frac{\rho}{\epsilon_F} \left(1 + \frac{\omega}{2qv_F} \ln \frac{\omega - \omega_a - qv_F}{\omega - \omega_a + qv_F} \right), \quad (3.56)$$

where:

$$\omega_a = \frac{\omega_c}{\left(1 + \frac{3\rho \mathcal{W}(\rho, m)}{2\epsilon_F} \right)} = \frac{2}{3} \frac{k_F^2}{m} \xi,$$

and the last step has been obtained by using relation (3.29).

The imaginary part of Equation (3.55) provides the excitations strengths $S^\pm(q, \omega) = \sum_n |\langle n | \tau_f^\pm | 0 \rangle|^2 \delta(\omega - \omega_{no})$ corresponding to the $\Delta S_z = \pm 1$ channels, respectively, through the relation:

$$S^-(q, \omega) - S^+(q, -\omega) = -\frac{1}{\pi} \text{Im}(\chi_t). \quad (3.57)$$

As we did for Equations (3.42) and (3.43), Equations (3.55) and (3.56) can then be recast in the following way using the dimensionless variables $s = \omega/(qv_F)$ and $z = 3q/(2k_F\xi)$:

$$\frac{\chi_t^0(q, \omega)}{V\nu} \equiv \frac{\chi_t^0(s, z)}{V\nu} = \Omega_\pm(s, z), \quad (3.58)$$

with

$$\nu = mk_F/\pi^2,$$

$$\Omega_\pm(s, z) = -\left(1 + \frac{s}{2} \ln \frac{s-1-1/z}{s+1-1/z} \right),$$

and

$$\frac{\chi_t(q, \omega)}{V\nu} \equiv \frac{\chi_t(s, z)}{V\nu} = \frac{\Omega_\pm(s, z)}{1 - 2\nu \mathcal{W}(\rho, m) \Omega_\pm(s, z)}. \quad (3.59)$$

The \pm sign in the definition of Ω indicates that it includes both the $\Delta S = +1$ and $\Delta S = -1$ channels.

RESULTS

We now present the main results of our research. First, the calculations for the equation of state (EOS) computed employing auxiliary field diffusion Monte Carlo (AFDMC) methods are reported. From the EOS, we compute the response functions within the time-dependent local spin density approximation (TDLSDA) in Section 4.2 and the evaluation of the neutrino mean free path in partially spin-polarized neutron matter in Section 4.3. The compressibility and the magnetic susceptibility of pure neutron matter are computed in the last two sections.

4.1 EQUATION OF STATE

The key ingredient of any calculation of pure neutron matter properties is the computation of the equation of state. This is achieved by means of Auxiliary Field Diffusion Monte Carlo Methods [90, 105]. Two different nucleon-nucleon interaction schemes, which have been presented in Chapter 2, have been used. The first EOS is derived from the phenomenological potential presented in Section 2.1, i.e., the Argonne AV8' potential for the two-body interaction, plus the Urbana UIX interaction for the three-body channel. The second EOS is based on potentials derived within chiral effective field theory (EFT). Among different implementations of the effective chiral potential which have been recently developed, we chose a local formulation up to N2LO, which have been derived by A. Gezerlis *et al.* [44, 45] as explained in Section 2.2.

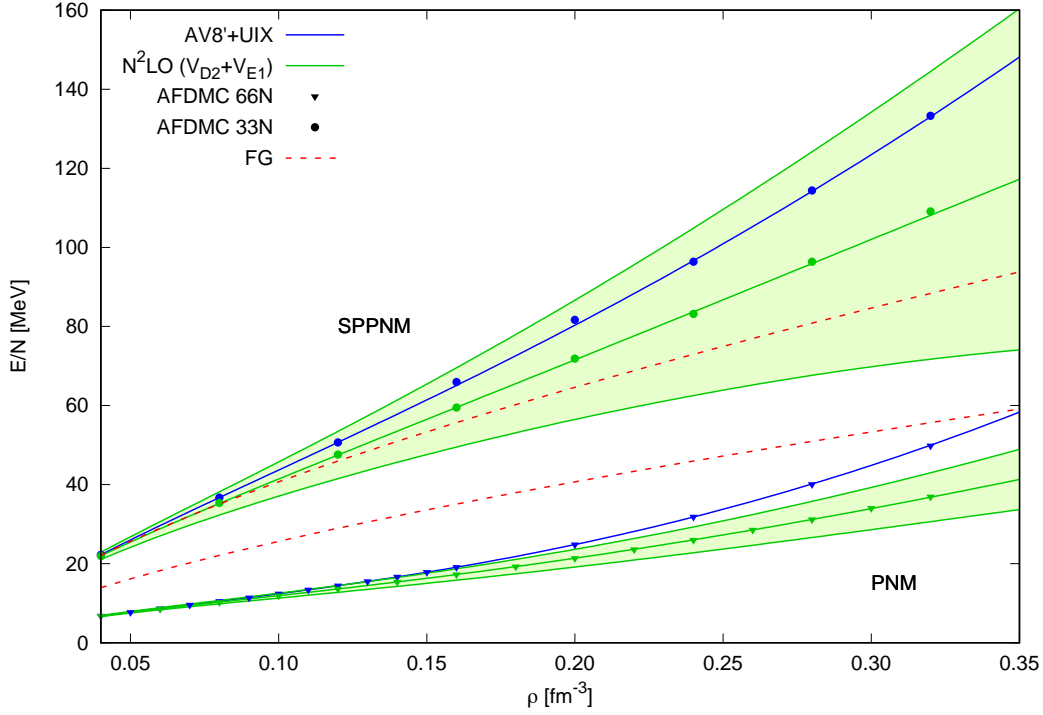


Figure 4.1: Equation of state for pure neutron matter (PNM - lower set) and for fully spin-polarized pure neutron matter (SPPNM - upper set). The blue curves are the AFDMC calculations with AV8'+UIX, while the green bands are the results with the chiral local potential up to N2LO. Errorbars for the chiral effective interaction have been computed according to Epelbaum et al. [116]. We also report the corresponding curves for a free Fermi gas at the thermodynamic limit (red dotted curves), from Ref. [117].

In Figure 4.1 we report the results obtained from our calculations of fully spin-polarized pure neutron matter (SPPNM) for densities ranging from $\rho_0/4$ up to $2\rho_0$, where $\rho_0 = 0.16 \text{ fm}^{-3}$ is the nuclear saturation density. The results for pure neutron matter (PNM) are those obtained by Gandolfi et al. [111] and Tews et al. [46] for the phenomenological and the chiral interaction, respectively. As indicated in Section 2.2 we chose a local formulation of the chiral potential at N2LO (D2,E1) with cutoff $R_0 = 1.0 \text{ fm}$, $c_E = 0.62$, and $c_D = 0.5$. This specific choice of the parameterization provides a realistic EOS, and it is similar to that of AVX potentials. Comparing the two different choices of the potentials allows us to analyze the sensitivity of the systematic uncertainties of the observ-

ables. The calculations for the SPPNM EOS were performed for $N = 33$ neutrons (closed-shell configuration), all with the same spin in a periodic box. Although the fully spin-polarized system is never the ground state of the system, we can use QMC calculations to compute the energy of such a state. The energy is projected starting from a state of given symmetry (in this case equivalent to a fully polarized liquid), and no orthogonal components are acquired during the projection to the ground state. In this way, we can simulate the polarized phase. As discussed in Section 3.1, the fermion sign problem is taken under control with the constrained-path approximation. The calculations for fully spin-polarized phases are not a novelty in the field. In fact, they have been performed for the electron gas [118] and atomic ${}^3\text{He}$ [119] several years ago. The potential was computed by a sum over the first neighbors of a given simulation cell, to reduce the impact of finite size effects. The statistical errors of the AFDMC calculations, reported in Figure 4.1, are of the size of the symbols. The bands relative to the chiral potential results refer to the theoretical error coming from the truncation in the chiral expansion. They have been obtained using the prescription of Epelbaum et al. [116]. According to Ref. [116] the theoretical uncertainties bands for an observable X can be estimated as:

$$\begin{aligned}\Delta X^{\text{NLO}} &= \max(Q^3 \times |X^{\text{LO}}|, Q \times |X^{\text{LO}} - X^{\text{NLO}}|) \\ \Delta X^{\text{N2LO}} &= \max(Q^4 \times |X^{\text{LO}}|, Q^2 \times |X^{\text{LO}} - X^{\text{NLO}}|, \\ &\quad Q \times |X^{\text{NLO}} - X^{\text{N2LO}}|),\end{aligned}\tag{4.1}$$

where $Q = \max(p/\Lambda, m_\pi/\Lambda)$, with Λ (normally $\simeq 1$ GeV) defining the breakdown scale, m_π is the pion mass, and p is the typical exchanged momentum. Besides, there is a further constraint for theoretical uncertainties at NLO and N2LO, i.e., they must have at least the size of the actual higher-order contribution. Higher-order contributions can be estimated as $Q^2 \times X^{\text{LO}}$ and $Q^3 \times X^{\text{NLO}}$ for the NLO and N2LO respectively. The dominant terms for PNM and SPPNM are the higher-order contribution. In principle, all orders of the expansion need to be calculated to estimate the uncertainty, but we can estimate the theoretical error as $Q^3 \times X^{\text{N2LO}}$. This approach is an approximation, but it provides a reasonable estimate (within 5 – 10%) compared to the full analysis. As an example, we report in Figure 4.2 the full analysis of the order by order expansion for the fully

spin-polarized case. We chose a breakdown scale $\Lambda = 600$ MeV (in accordance to Ref. [108]) and we computed the typical exchanged momentum as:

$$p \sim \sqrt{2m \frac{3k_F^+{}^2}{5 \cdot 2m}}, \quad (4.2)$$

where k_F^+ is the Fermi momentum of the polarized system at a given density ρ and m is the neutron mass. While at saturation density, the theoretical uncertainties decrease, as predicted by the perturbative expansion, at $\rho = 2\rho_0$ the theoretical uncertainties remain of the same order between NLO and N2LO. This feature indicates that we are close to the limit of applicability of the perturbative approach, and the chiral effective field theory is well-defined. The EOS for

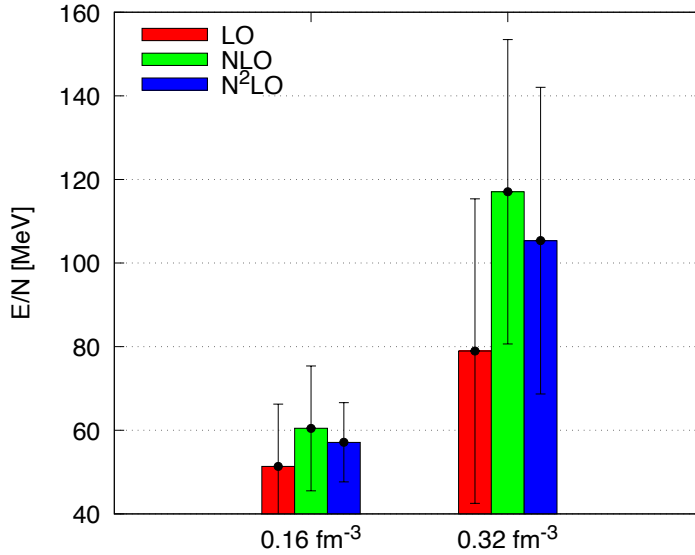


Figure 4.2: The histograms show the AFDMC calculation, with the local chiral potential described in the text, at saturation and twice saturation density for the fully spin-polarized system. Order by order estimate of the theoretical uncertainties at LO (red), NLO (green), and N2LO (blue) are provided. Statistical uncertainties from AFDMC are smaller than the size of the points (adapted from Ref. [117]).

the polarized system obtained from chiral potential is in reasonable agreement with the one obtained by Krüger et al. [120], at least up to saturation density. The EOS derived using the AV8'+UIX interaction is in very good agreement with

those obtained in previous works for Brueckner-Hartree-Fock calculations with AV18+UIX [121, 122]. To remove the bias of the constrained-path approximation, we should do an unconstrained evolution. The effects have just been recently explored, though, for the two-body part of the interaction only [110]. We think that including the three-body forces, the relative effects of performing the unconstrained evolution are even smaller, at least for PNM. The reason might just be that the three-body forces are much stronger than the spin-orbit term, and thus the error becomes relatively small. The AFDMC results are fitted in order to derive the energy density functional to be used in the TDLSDA response function. In the local density (mean field) approximation, as explained in Section 3.3, the energy as a function of the density ρ and the spin polarization ξ can be generically written as:

$$E(\rho, \xi) = T_0(\rho, \xi) + \int \epsilon_V(\rho, \xi) \rho \, d\mathbf{r}. \quad (4.3)$$

The kinetic energy T_0 as been computed using the bare neutron mass. The quantities ρ and ξ are related to the density of particles with spin up ρ_\uparrow and the density of particle with spin down ρ_\downarrow in the following way:

$$\rho = \rho_\uparrow + \rho_\downarrow; \quad \xi = \frac{\rho_\uparrow - \rho_\downarrow}{\rho}. \quad (4.4)$$

We define the function $\epsilon_V(\rho, \xi)$ using the common assumption of a quadratic dependence on the spin polarization:

$$\epsilon_V(\rho, \xi) = \epsilon_0(\rho) + \xi^2 [\epsilon_1(\rho) - \epsilon_0(\rho)] , \quad (4.5)$$

where the functions ϵ_i are defined as polynomials in the neutron density:

$$\epsilon_i(\rho) = \epsilon_i^0 + a_i \left(\frac{\rho - \rho_0}{\rho_0} \right) + b_i \left(\frac{\rho - \rho_0}{\rho_0} \right)^2 + c_i \left(\frac{\rho - \rho_0}{\rho_0} \right)^3. \quad (4.6)$$

Such functions contain the whole information about the interaction, i.e. all the terms that in ordinary local density approximation theory for Coulombic systems are separately referred to as "direct", "exchange", and "correlation" terms [123]. The index $i = 0, 1$ indicates the spin unpolarized and polarized neutron matter ($\xi = 0, 1$) respectively. The expansions of the energy density functional in integer powers of the density can be directly related to the presence of some external field (first power) that stabilizes the asymmetric spin and/or isospin phase of matter, a

two-body interaction, a three-body interaction, and so on. Another choice for the energy-density functional would be to consider non-integer exponents, but we are not going to consider it in this work. In addition, we do not consider the explicit dependence on the momentum (i.e., derivatives of the density). These terms are usually related to the tensor parts of the interaction. We think that the features are still captured by our simpler choice, even not including them explicitly, since we fit AFDMC calculations with realistic potential, which also includes tensor terms. As usual, we assume the value of the saturation density to be $\rho_0 = 0.16 \text{ fm}^{-3}$. Despite there is no implicit or explicit expectation of a hierarchical ordering in our expansion of the density functional, the coefficients fitted on the numerical AFDMC results for EOS-A (AV8+UIX) and EOS- χ (EFT), reported in Table 4.1, show some prevalence of the first and second-order expansion terms (apart for EOS- χ_l for SPPNM, which has b_i and c_i of the same order).

EOSA		ϵ_i^0	a_i	b_i	c_i
(SPPNM)	$i=1$	9.411	21.997	13.032	0.262
(PNM)	$i=0$	-15.97	-2.689	12.435	0.521
EOS χ		ϵ_i^0	a_i	b_i	c_i
(SPPNM)	$i=1$	3.85	10.975	6.433	-1.506
(PNM)	$i=0$	-17.81	-7.865	7.746	-0.934
EOS χ_u		ϵ_0	a_i	b_i	c_i
(SPPNM)	$i=1$	13.87	29.206	14.573	-1.502
(PNM)	$i=0$	-16.36	-5.117	9.367	-0.565
EOS χ_l		ϵ_i^0	a_i	b_i	c_i
(SPPNM)	$i=1$	-6.18	-7.256	-1.707	-1.510
(PNM)	$i=0$	-19.26	-10.614	6.126	-1.303

Table 4.1: Coefficient fitting the density functional of Equation (4.6) to the EOS computed by means of the AFDMC method. EOSA refers to the EOS from the AV8'+UIX potential, while the EOS χ are relative to the Hamiltonian with the local N2LO(D2,E1) chiral interaction. The three tables refer to the center, upper limit and lower limit of the uncertainty band respectively.

4.1.1 Effective mass

In our approach, the kinetic energy term T_0 of the energy density function of Equation (4.3) does not include an effective mass. On the other hand, different many-body methods use an effective mass. They claim inconsistent results in the response functions, and neutrino mean free paths, either using the effective or the bare mass. Within our approach, we have the constraint that the total energy of the bulk always has to reproduce the AFDMC results. Since we are working within a mean field approach, multipair contributions are neglected. This reflects in the fact that the collective modes should not change their energy, while the strengths of the particle-hole excitations might differ. In principle, this is not true, but one has to include all multipair contributions. In some systems, these contributions are not negligible and can dramatically change the prediction of the model [124]. In our case, we limit our analysis to the low- q , and low- ω plane, where our mean field approximation holds and multipair excitations give a really small contribution.

It is possible to predict the effective mass emerging from the quantum Monte Carlo calculations from the diffusion of a neutron during the simulation. For instance, a quick estimate of the effective mass ratio at saturation density obtained using a potential of the form $AV6'$ gives a value of $m^* \sim 0.92$. This result is in agreement with the results obtained from the study of excited states of the system [125]. The effective mass ratio can be directly estimated from the self-diffusion coefficient of a particle in a DMC calculation. We computed the effective mass for a system of 14 neutrons in which periodic boundary conditions have been turned off. The diffusion coefficient was computed for the Fermi gas and for an interacting system of neutrons interacting with the two-body $AV6'$ potential, which includes the tensor term, at saturation density. First, we computed the averaged squared distance $\langle r^2 \rangle$ traveled by a neutron in a random walk as a

function of the diffusion time as shown in Figure 4.3. This quantity is strictly related to the kinetic part of the imaginary time propagator:

$$\begin{aligned} G_0(R', R) &= \langle R' | e^{-T\delta\tau} | R \rangle. \\ &= \left(\frac{m}{2\pi\hbar^2\delta\tau} \right)^{\frac{3N}{2}} e^{-\frac{m(R-R')^2}{2\hbar^2\delta\tau}}, \end{aligned} \quad (4.7)$$

which is formally equivalent to the Green's function of a diffusion equation in which the diffusion constant $\tilde{D} \propto \hbar^2(m_n/\tilde{m})$, where m_n is the bare neutron mass. To estimate the effective mass ratio m^* one just needs to compute the ratios:

$$m^* = \frac{\tilde{m}}{m} = \frac{D}{\tilde{D}}, \quad (4.8)$$

where D and m are the diffusion coefficient and the mass respectively in the case of the FG.

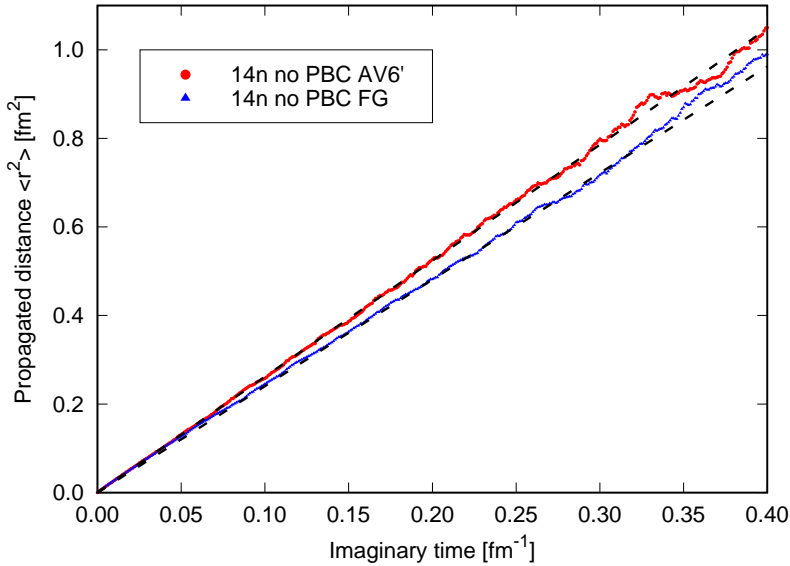


Figure 4.3: Calculation of the diffusion coefficient for the case of the Fermi gas (FG) and for a system interacting with the two-body potential $AV6'$ at saturation density $\rho_0 = 0.16 \text{ fm}^{-3}$. The dashed line represents the fit to the two data-sets (see text for details), from Ref. [117].

In order to estimate D and \tilde{D} , we performed two fits on two different time windows on each data set to check the accuracy of our fit. The first fit has been performed in the time interval $(0.1 - 0.3) \text{ fm}^{-1}$ and the other in the range $(0.1 - 0.2)$

fm^{-1} . The two fits give essentially the same effective mass ratios ($m_1^* = 0.918$ and $m_2^* = 0.923$). Only the larger time interval fit is plotted in Figure 4.3. Comparing our result to the one obtained with the calculation of the effective mass ratio derived from non-perturbative calculations of the single-particle excitation spectrum of Ref. [125], we see a good agreement. The results are consistent even if we only employed the two-body potential $AV6'$ rather than the full two- plus three-body interaction $AV8'+UIX$.

However, in this approach, the equation of state is inclusive of all the correlation effects leading, among the others, to the correction to the kinetic energy accounted by the effective mass itself, even if our convention is to assume the neutron mass equal to the bare mass. In order to compare the difference between using the bare mass or the effective mass, we evaluated response functions, and neutrino mean free paths at saturation energy with the effective mass. We assumed the effective mass to be constant over the density range $\rho_0/4 \leq \rho \leq 2\rho_0$. To build a new effective potential consistent with the effective mass, we refit the constants of the energy-density function of Equation (4.5) to our AFDMC calculations. While the response in the longitudinal and transverse channel might be different between the two cases, due to the reshuffling contributions from particle-hole and collective modes (see Figure 4.4, Figure 4.5 and Figure 4.6), the neutrino mean free path results are qualitatively independent on the choice of either the effective mass or the bare mass (see Figure 4.8).

4.2 RESPONSE FUNCTIONS

The numerical evaluation of the longitudinal and transverse response functions gives access to information about the neutron dynamics. The derivation of the response functions within the TDLSDA has been presented in Section 3.3. The single particle excitations strengths are computed using Equations (3.47) and (3.57). On the other hand, the poles of Equations (3.44) and (3.59) are the energies of the collective modes of the system. Naming $N(s)$ and $D(s)$ the numerators and the

denominators of Equations (3.44) and (3.59), respectively, we expand around the poles at $s = \bar{s}$ to evaluate the strength as:

$$\frac{S(s)}{V\nu} = \frac{N(s)}{\partial D/\partial s} \delta(s - \bar{s}), \quad \text{and} \quad \frac{S(s)}{Nm/(2k_F^2)} = \frac{N(s)}{\partial D/\partial s} \delta(s - \bar{s}) \quad (4.9)$$

for the longitudinal and the transverse channel respectively. The collective modes are indicated by arrows in Figures 4.4–4.6. In the longitudinal channel the strength of the collective modes have been rescaled: longer arrows correspond to dominant scalar or vector contribution (their strength would be too small compared to the particle-hole contribution). In the transverse channel the correct strength has been plotted instead.

We report in Figure 4.4 the results obtained from the calculation of the longitudinal response functions for the two different potentials used, i.e., the phenomenological AV8'+UIX interaction and the local chiral potential at N2LO. The plots are made as functions of the dimensionless quantity $s = \omega/(qv_F)$ for a fixed value of the spin polarization $\xi = 0.2$ and for three different values of the density which are characteristic of the outer core of a neutron star ($\rho = 0.08, 0.16,$ and 0.32 fm^{-3}).

In Figure 4.5 the same quantity is reported for spin unpolarized neutron matter. The percentages reported in the graphs show the fraction of the total strength relative to the particle-hole contribution. Arrows represent the presence of collective modes (the size is not proportional to the strength). For the response computed using the N2LO potential, we propagated the theoretical uncertainty. As expected, at the lowest density considered, the results are qualitatively and quantitatively very insensitive to the specific interaction used. At saturation density and above, the theoretical uncertainty on the pressure is reflected in a more pronounced difference in the characterization of the single-particle spectrum. In particular, this can be observed in the scalar channel in the region around $\omega = qv_F$. At least qualitatively, the vector channel is somewhat less affected by the theoretical uncertainty.

A similar behavior is visible in the collective modes. The energy of the collective modes strongly depends on the stiffness of the equation of state. A consequence is that the energy of the collective modes, at larger densities, becomes signifi-

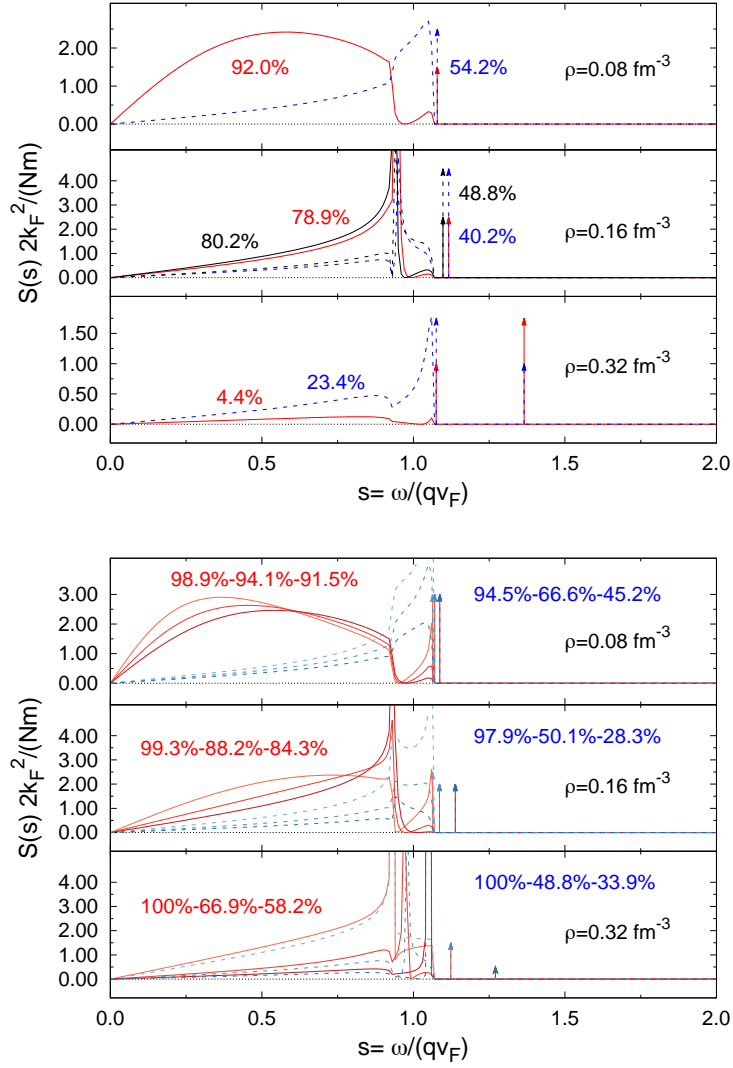


Figure 4.4: Longitudinal response function at spin polarization $\xi = 0.2$ for AV8'+UIX (upper) and chiral potential at N2LO (lower). The solid red lines and blue dashed lines stand for density and spin density Dynamical Structure Factors (DSFs), respectively. Arrows indicate the presence of a collective mode. The percentages in the plot show the fraction of the total strength pertinent to the particle-hole excitations. The black lines at saturation density for the phenomenological potential (upper) show the results using the effective mass instead of the bare mass. Note that the effective mass enters in the definition of the variable s . On the lower panel, the three lines for each DSF keep track of the theoretical uncertainties obtained using chiral effective interaction. Lighter to darker curves stand for lower-central-higher EOS $_{\chi}$ of Figure 4.1 and Table 4.1. The same color scheme holds for Figure 4.5 (from Ref. [117]).

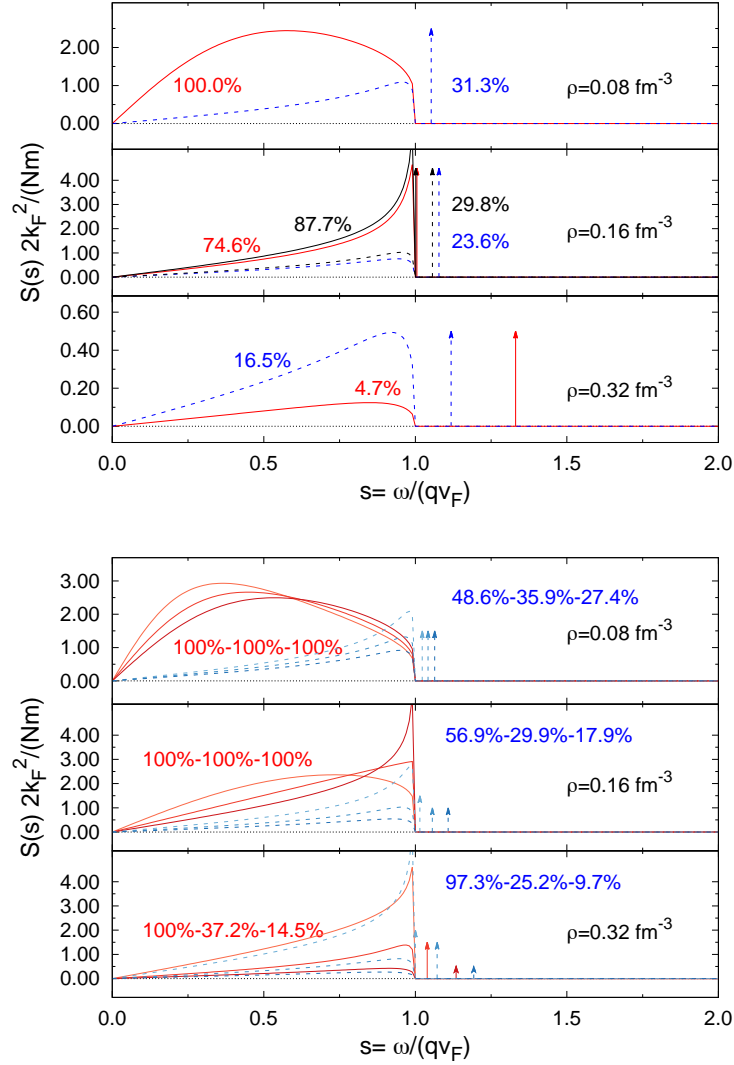


Figure 4.5: Longitudinal response function for AV8'+UIX (upper) and chiral potential at N²LO (lower) at spin polarization $\xi = 0.0$, i.e. PNM. The color scheme is described in Figure 4.4 (from Ref. [117]).

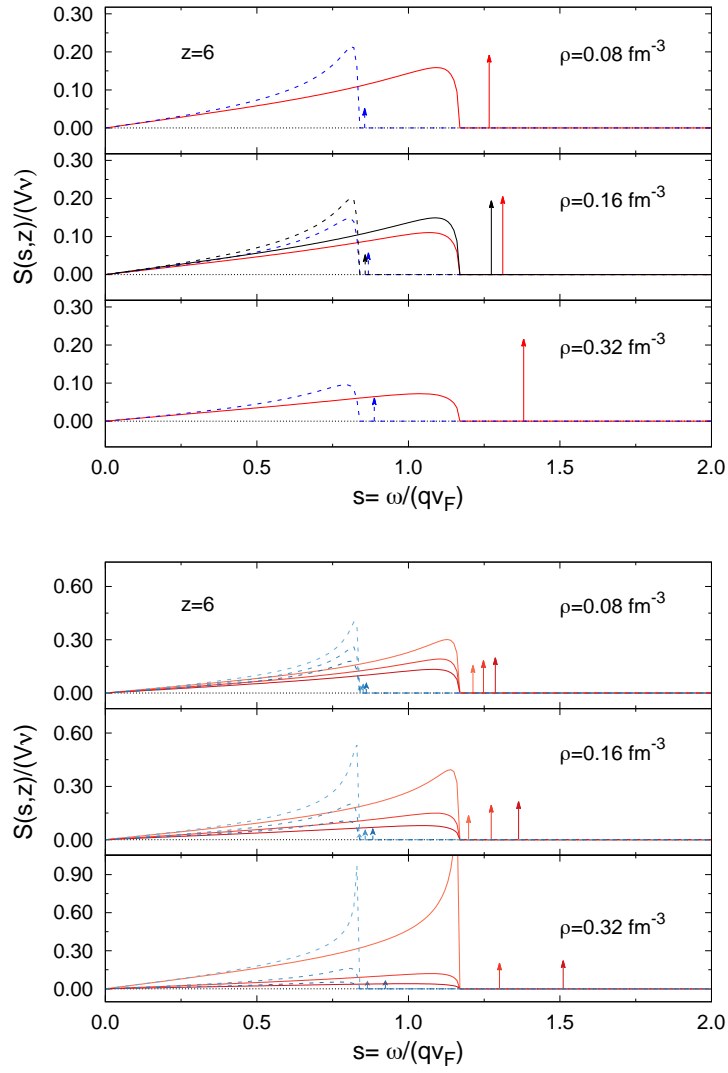


Figure 4.6: Transverse response function at low spin polarization ($z = 6$) for AV8'+UIX (upper) and for chiral potential at N2LO (lower). Recall that $z = \frac{3q}{2k_F\xi}$, so $z > 1$ means small ξ . The full and dashed lines indicate the particle/hole and collective strengths in the $\Delta S_z = -1$ ($s > 0$ - red) and $\Delta S_z = +1$ ($s < 0$ - blue, which has been plotted flipped and in the $s > 0$ region) channels respectively. The black lines at saturation density for the phenomenological potential (upper) show the results using the effective mass instead of the bare mass. Note that the effective mass enters in the definition of the variable s . On the lower panel the three lines for each DSF keep track of the theoretical uncertainties obtained using chiral effective interaction. Lighter to darker curves stand for lower-central-higher EOS $_{\chi}$ of Figure 4.1 and Table 4.1 (from Ref. [117]).

cantly higher in the AV8'+UIX case. It should be noticed that in pure neutron matter, collective modes are not present for the lowest density considered in the scalar channel. On the contrary, at $\xi = 0.2$ one always sees the presence of a collective mode. There are some further systematics to be noticed in the behavior of the collective modes. At $\xi = 0$, the spin mode appears with a dispersion for $q \sim 0$ more or less independent of the density, whose strength is only slightly increasing with ρ . This is in contrast with the density mode that begins to have significant strength only at densities around saturation and quickly increases its dispersion coefficient. This fact points to a substantially different nature of these excitations. In particular, the spin mode appears to be similar to a spin-density wave in neutron matter. The polarization of the medium induces a coupling between the spin and the density modes due to the spin imbalance. This translates into the appearance of a low strength density mode at the same energy of the spin one for low densities. At higher densities, the two collective excitations separate in energy mostly in the same way as in the $\xi = 0$ case, although the mixing is still visible in the presence of a second, low strength peak for both modes.

For the transverse response, positive values of s describe the excited states in the $\Delta S_z = -1$ channel, while for negative values of s , the excited states in the $\Delta S_z = +1$ channel. In Figure 4.6, we show the results for the transverse response function.

In this case, instead of fixing the polarization, we fixed the value $z = 3q/(2k_F\xi) = 6$, still corresponding to a case of low magnetization. The results are qualitatively very close to those obtained for the longitudinal channel. In contrast, the dependence on the specific choice of the interaction is weaker, both for the particle-hole and the collective part of the spectrum. Contrary to what happens in the longitudinal channel, both collective modes do not show a significant variation of the linear dispersion coefficient with the density. It is interesting to observe, however, that the coefficient is very different between the $\Delta S_z = -1$ and the $\Delta S_z = 1$ excitations. This means that the two modes have a gap that is proportional to the neutron matter polarization.

4.3 NEUTRINO MEAN FREE PATH

The neutrino processes considered in order to determine the neutrino mean free path (NMFP) are the neutral-current scattering $n + \nu \rightarrow n + \nu$, since TDLSA includes only single-pair excitations. Neutron bremsstrahlung $n + n \rightarrow n + n + \nu + \bar{\nu}$ processes and its inverse $n + n + \nu + \bar{\nu} \rightarrow n + n$, as well as the inelastic scattering process $\nu + n + n \rightarrow n + n + \nu$, are intrinsically two-pair excitations and are not included in this calculation [126, 127]. Note that we are working with PNM, so we are not considering β -decay processes or any other process involving protons.

Another important remark is that we are computing response functions and neutrino mean free paths at zero temperature. In principle, temperature effects are not negligible, since in proto-neutron stars temperatures are around a few tens of MeV. At finite temperature also negative values of the transferred energies are accessible, and the dynamic structure factors are damped increasing with temperature. The corresponding neutrino mean free paths should scale as T^{-2} [128], where T is temperature, but this is the case only at very low temperature [129]. In addition, at high temperatures the neutrino mean free paths approach the free Fermi gas results.

The NMFP can be computed by integrating the total excitation strength $S(q, \omega)$ (in both the longitudinal and transverse channels), to first obtain the total neutrino cross section σ [130, 131]:

$$\sigma = \frac{G_F^2}{2} \frac{1}{E} \int dq \int d\omega (E - \omega) q \left[1 + \frac{E^2 + (E - \omega)^2 - q^2}{2E(E - \omega)} \right] S(q, \omega), \quad (4.10)$$

where E is the incident neutrino energy, and $G_F = 1.166 \times 10^{-5} \text{ GeV}^{-2}$. The integration must be performed on the kinematically accessible region of q and ω compatible with the scattering kinematics, as discussed in Ref. [130]. By defining $k^\mu = (k^0, \vec{k})$ and $k'^\mu = (k'^0, \vec{k}')$ as the incoming and outgoing 4-momenta of the neutrino and $q^\mu = (\omega, \vec{q})$ is the transferred 4-momentum. We assume that neutrinos are ultra-relativistic. The limits on ω and q are obtained from the form the region in which the factors $S(q, \omega)$ are non zero, i.e., $-qv_F < \omega < qv_F$

corresponding to the continuum of single-particle excitations and $\omega = \pm c_s q$ for collective mode. For the single-pair continuum we can rewrite the condition in terms of initial neutrino momentum as $|\omega| < cq < |\omega - 2ck|$ and this implies $\omega < c(2k - q)$. The accessible region is shown in Figure 4.7, and this region has to be intersected with the region allowed by the dynamical structure factor $S(q, \omega)$ to get the in integration domain.

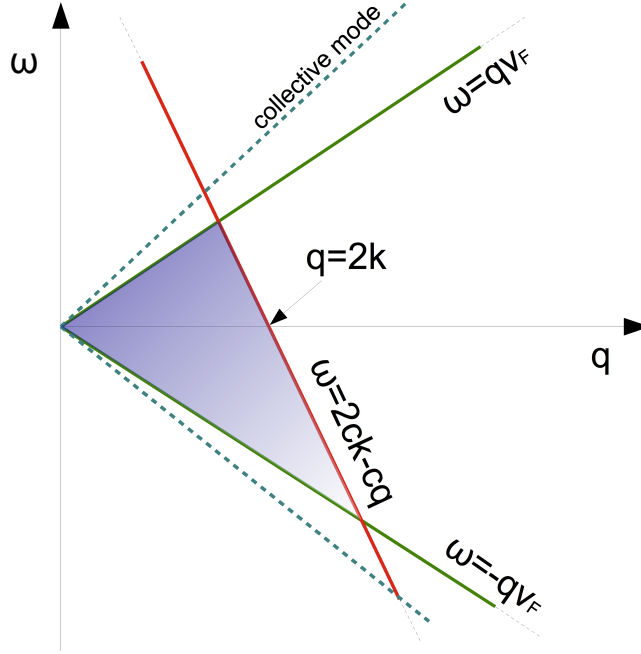


Figure 4.7: Integration region of q and ω for ultra-relativistic and non-degenerate neutrinos.

This holds for non-degenerate neutrinos.

We will assume neutrinos to be ultra-relativistic and non-degenerate. The NMFP λ can be derived from the total neutrino cross section σ from the relation $\lambda = 1/(\sigma\rho)$.

From existing estimates of neutron spin susceptibility [132], we expect the induced spin polarization to be low even in the presence of strong magnetic fields. We could estimate the order of magnitude of the spin polarization ξ as:

$$2\xi\Delta E = \mu_n B, \quad (4.11)$$

where μ_n is analogous of the Bohr magneton for the neutron, and B is the external magnetic field. ΔE is the energy difference between the fully spin-polarized and the spin unpolarized system. The maximum superficial magnetic field observed for a magnetar is $B_{\text{surf}} \sim 10^{10} - 10^{11}$ T. This would lead to expected spin polarization of the order of $10^{-5} - 10^{-4}$ at saturation density. Internal dynamo effects might power up the magnetic field by a factor $10^2 - 10^3$, which leads to an expected spin polarization $\xi \sim 10^{-3} - 10^{-1}$.

In Figure 4.8, we report the results we obtained at saturation density for spin polarization $\xi = 0.0$ and $\xi = 0.1$ and compared them with the result obtained for PNM with a more refined method [133] using the correlated Tamm-Dancoff approximation (CTDA). Within the CTDA [131] the states are expressed as a basis of correlated 1p-1h excitations.

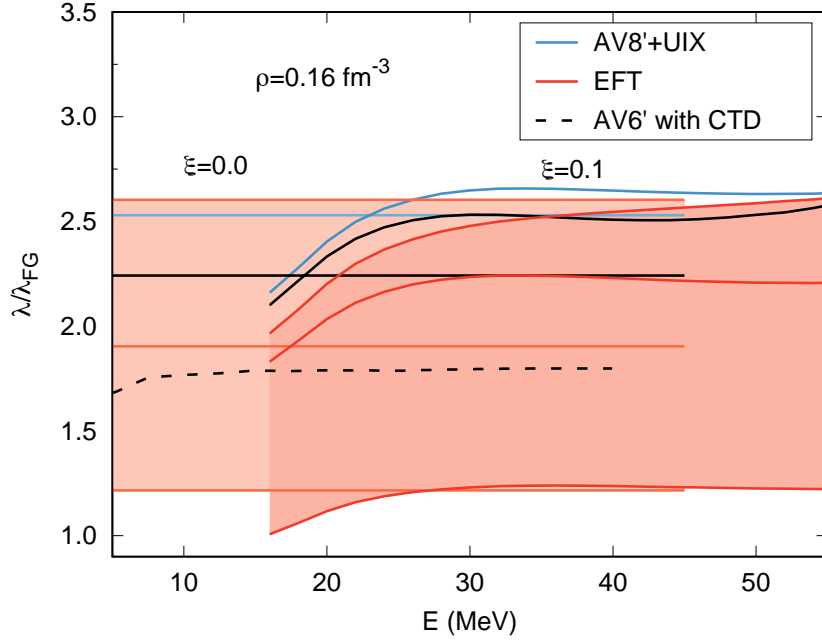


Figure 4.8: Neutrino mean free path ratio with respect to the free Fermi gas at saturation density $\rho_0 = 0.16 \text{ fm}^{-3}$ for spin polarization $\xi = 0.1$ and for PNM ($\xi = 0$). Top-middle-bottom lines for EFT refer to higher-central-lower EOS_χ of Figure 4.1 and Table 4.1. The results for the phenomenological potential with the effective mass are plotted in black full lines (from Ref. [117]).

The correlations are then encoded into effective operators acting on $1p-1h$ states. The NMFP for spin unpolarized pure neutron matter is essentially independent of the incident energy of the neutrinos. The presence of a small spin-asymmetry shows non-trivial patterns instead, significantly increasing the neutron matter opacity for low neutrino energies.

The estimated theoretical uncertainty on the results computed from the chiral interaction is quite significant. Nevertheless, the prediction obtained making use of the phenomenological interaction differ of about 20% from that of the N2LO potential, close to the upper limit predicted by the propagated uncertainty.

In Figure 4.9, we compare our results for the NMFP ratio at saturation density to those of Pastore et al. [134] and to those of Lovato et al. [133].

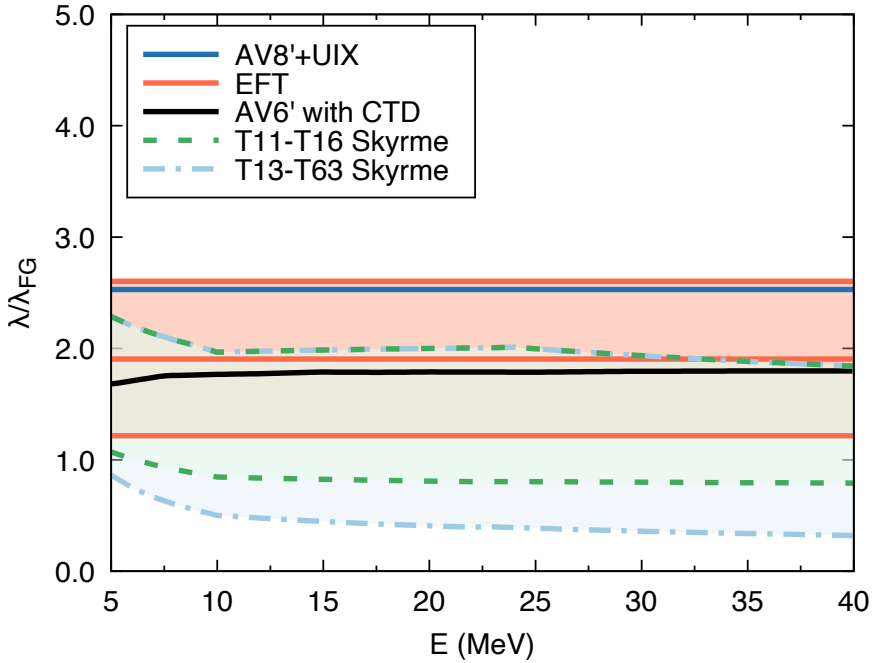


Figure 4.9: NMFP for PNM at saturation density from the present work compared to those obtained by Lovato et al. [133] and by Pastore et al. [134]. In the latter case different bands correspond to different choices of the tensor term of the Skyrme potential. Top-middle-bottom lines for EFT refer to higher-central-lower EOS $_{\chi}$ of Figure 4.1 and Table 4.1 (from Ref. [117]).

The first paper presents computations using a Skyrme force explicitly, including tensor contributions, which we instead do not address with specific terms. The

second case also includes explicit correlations introduced via the Tamm-Dancoff approximation. All results tend to overlap in a region around $\lambda/\lambda_{FG} \sim 2$. Skyrme results, however, tend to predict a lower value of NMFP. This might be due to the different treatment of correlations. A similar effect is also visible in the comparison of the Tamm-Dancoff results and our results for the Argonne potential. It should be remarked, however, that all these results start from different neutron-neutron interaction schemes, and it is not very easy to attribute the differences either to the potential used or to the degree of approximation of the functional employed. In Figure 4.10, we show the contribution of the different channels to the total neutrino mean free path. As an example, we report the results for the phenomenological potential AV8'+UIX at spin polarization $\xi = 0.1$.

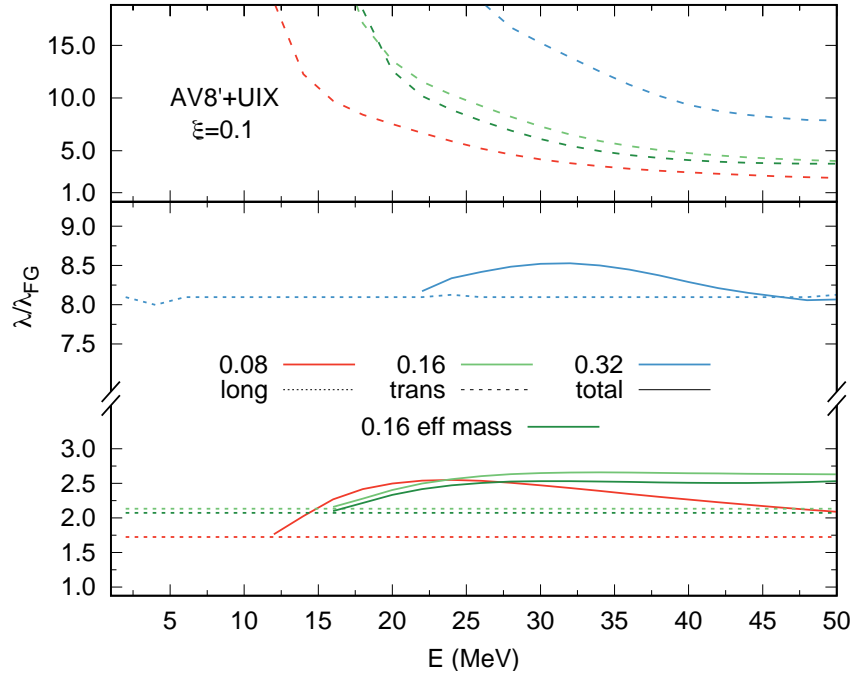


Figure 4.10: Neutrino mean free path ratio with respect to the free FG for spin polarization $\xi = 0.1$ as a function of density. Dotted lines are the contributions coming from the longitudinal channels, dashed lines from the transverse part, while solid lines show the total mean free path. The results for the effective mass are plotted in dark green (from Ref. [117]).

Results are plotted at saturation density $\rho_0 = 0.16 \text{ fm}^{-3}$, half, and twice saturation density. We observe that at all densities, the contribution coming from the

longitudinal part is almost constant as a function of the energy of the incident neutrino. We observe that for both channels, NMFP increases with the density. However, since the relative weight of the two contributions is different for each density, the result gives a total NMFP with non-trivial density dependence.

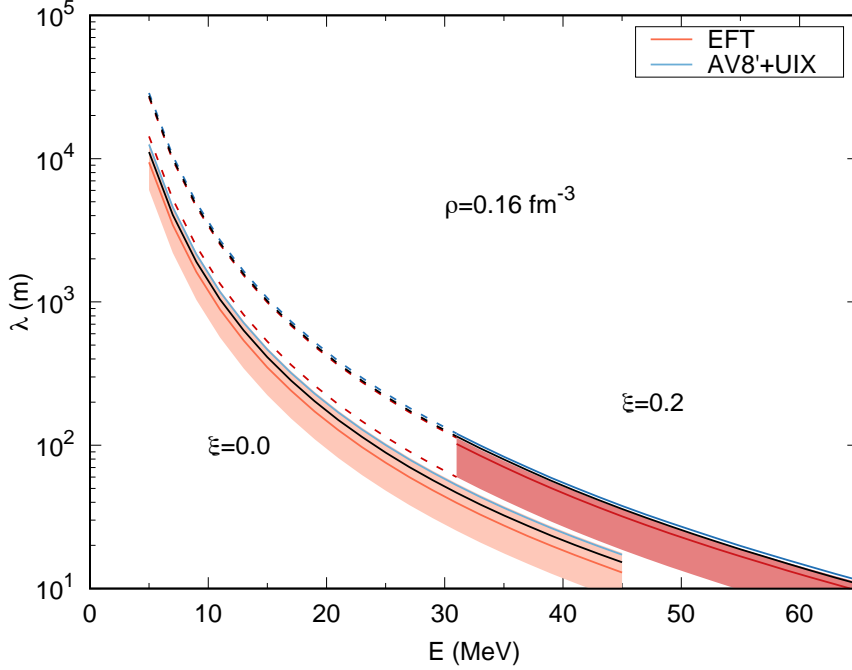


Figure 4.11: Neutrino mean free path for PNM and for spin polarization $\xi = 0.2$ as a function of incident neutrino energy. In PNM the longitudinal and transverse channel contribute equally to the total NMFP, while as soon as there is some spin polarization we can observe an energy threshold under which the NMFP is entirely determined by the longitudinal response (dashed lines). The same behavior can be seen also in Figure 4.10 at various densities. Top-middle-bottom lines for EFT refer to higher-central-lower EOS_χ of Figure 4.1 and Table 4.1. The results for the phenomenological potential with effective mass are plotted in black (from Ref. [117]).

To understand the implication of spin-polarization to the NMFP, we show in Figure 4.11 the NMFP as a function of the energy of the incident neutrino. The NMFP has to be compared to the radius of the neutron star ($\approx 1.0 - 1.3 \cdot 10^4$ m): above this value matter is substantially transparent to neutrinos. On the other

hand, the typical energies of the neutrinos of astrophysical interest are in the range of 0.1 – 50 MeV [135, 136].

4.4 COMPRESSIBILITY

In order to make an even more direct comparison between our approach and other microscopical models, useful to assess its validity, we will discuss here the compressibility of PNM. The compressibility is a parameter that directly influences NMFP and other properties of astrophysical interest, in particular, the structure of neutron stars.

Given a fit of the equation of state as the one in Equation (4.5), it is possible to directly extract the compressibility from the definition:

$$K = -\frac{1}{V} \frac{\partial V}{\partial P}, \quad (4.12)$$

by rewriting it as a function of the energy per nucleon:

$$\frac{1}{K} = \rho^2 \left(\rho \frac{\partial^2 E/N}{\partial \rho^2} + 2 \frac{\partial E/N}{\partial \rho} \right). \quad (4.13)$$

However, the quantity that is usually reported is the compression modulus or incompressibility, which is defined as:

$$K_\infty = k_F^2 \frac{d^2 E/A}{dk_F^2}, \quad (4.14)$$

The two quantities are directly related by the following expression:

$$K_\infty = \frac{9}{\rho} \frac{1}{K}. \quad (4.15)$$

In this case we can check the consistency of our results using two independent ways to estimate the compressibility of PNM: 1) starting from the energy-density function using Equation (4.13), and 2) using the inverse energy weighted sum rule m_{-1} . As an example, in the scalar and vector longitudinal channels, m_{-1} reads [100]:

$$m_{-1}^{s,v} = \frac{V}{2} \frac{\nu_\uparrow(1 + G_\downarrow) + \nu_\downarrow(1 + G_\uparrow) \mp 2\sqrt{\nu_\downarrow\nu_\uparrow}G_{\uparrow\downarrow}}{(1 + G_\downarrow)(1 + G_\uparrow) - G_{\uparrow\downarrow}^2}, \quad (4.16)$$

where the minus sign is for the scalar case, while the plus sign holds for the vector case. In the case of spin-unpolarized PNM ($\xi = 0.0$) we have that $\nu_{\uparrow} = \nu_{\downarrow} = \nu$ and $G_{\uparrow} = G_{\downarrow} = G$ and we can write:

$$\frac{m_{-1}^s}{m_{-1}^0} = \frac{K}{K_0} = \frac{1}{1 + G + G_{\uparrow\downarrow}^2}, \quad (4.17)$$

where $m_{-1}^0 = V\nu/2$ and $K_0 = 9\pi^2 m/k_F^5$ respectively are the Fermi gas static polarizability and compressibility. The values we estimate within our approach using the two methods are always numerically indistinguishable.

Equation (4.17) shows once more the relationship between this approach and the Landau theory. The parameter G can, in principle, be identified with F_0 . This means, however, that the TDLSDA estimate of the compressibility also includes an order G^2 correction.

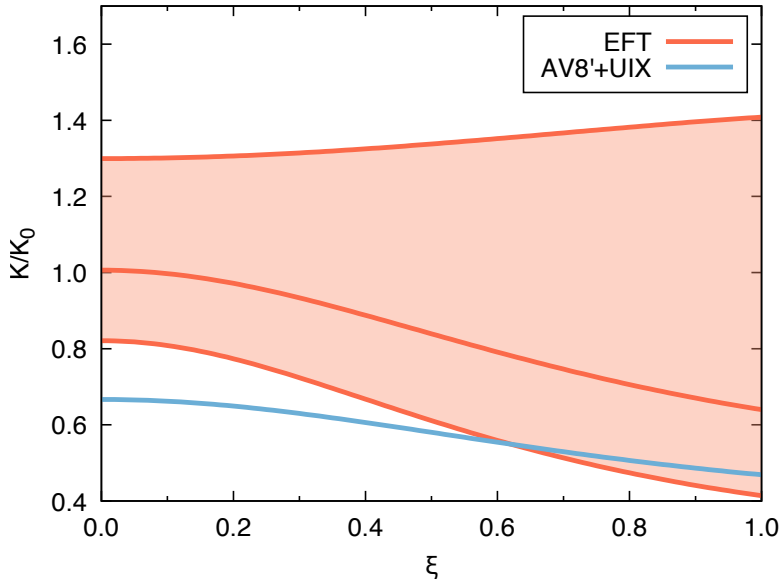


Figure 4.12: Compressibility ratio for PNM at saturation density as a function of the spin asymmetry. Top-middle-bottom lines for EFT refer to lower-central-higher EOS_{χ} of Figure 4.1 and Table 4.1 (from Ref. [117]).

The compressibility computed at saturation density as a function of the spin asymmetry ξ for the two different potentials used in this work is shown in Figure 4.12.

Interestingly enough, the chiral EFT potential would predict a compressibility ratio decreasing with ξ . However, at the lower limit of the predicted theoretical errorbar, this behavior is inverted. In this case, the Argonne-Urbana potential gives a substantially different value at $\xi = 0$ but tends to close the gap with the EFT potential for the fully spin-polarized case. In Figure 4.13 we show the compressibility ratio as a function of the density for the spin unpolarized PNM. As expected, the compressibility decreases as a function of the density. Chiral

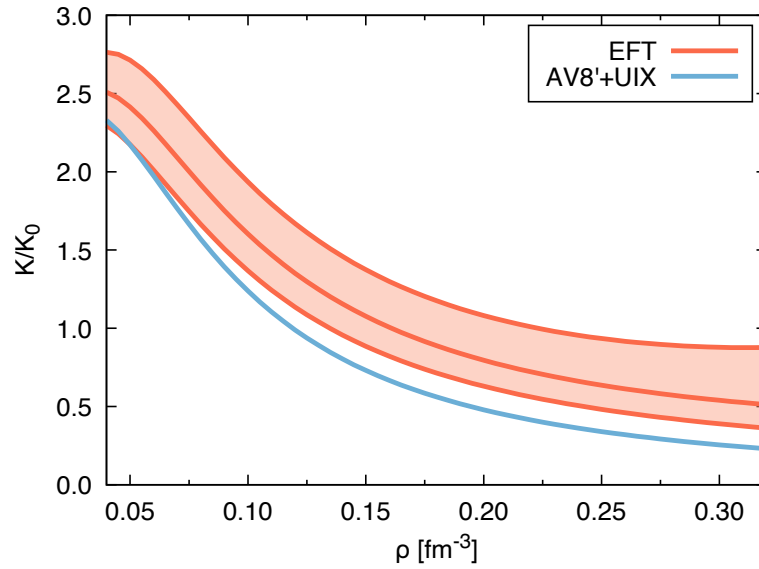


Figure 4.13: Compressibility ratio for spin unpolarized PNM in function of the density. Top-middle-bottom lines for EFT refer to lower-central-higher EOS_χ of Figure 4.1 and Table 4.1 (from Ref. [117]).

EFT potential systematically yields an higher value as a direct consequence of the fact the EOS for PNM is softer than the one obtained using the phenomenological AV8'+UIX potential.

We report in Table 4.2 a comparison of our prediction for the compressibility and the compression modulus to other results available in the literature. Our results are in agreement with previous results obtained by Fantoni *et al.* [132] with a similar potential within the same method. In contrast to AV8', AV6' has no spin-orbit terms. Even in this case, our approach tends to emphasize the effects of the stiffness of the EOS compared to other methods. In particular, it is in-

$\rho = 0.032 \text{ fm}^{-3}$	K/K ₀	K/ $\hbar c$ [fm ⁴]
AV8'+UIX	2.38	1103
EFT	2.51	1162
BHF [137]	2.54	1176
Skyrme [137]	2.57	1191
QHD [137]	3.17	1467
$\rho = 0.16 \text{ fm}^{-3}$	K/K ₀	($\hbar c$) ² ·K _∞ [MeV]
AV8'+UIX	0.67	526.1
EFT	1.01	348.6
AV18 (CBF) [138]	1.08	324.7
BKR $\rho < 0.182 \text{ fm}^{-3}$ [139]	2.83	123.8
BKR $\rho > 0.182 \text{ fm}^{-3}$ [139]	1.09	320.8
$\rho = 0.20 \text{ fm}^{-3}$	K/K ₀	($\hbar c$) ² ·K _∞ [MeV]
AV8'+UIX	0.48	849.3
EFT	0.80	511.3
AV6'+UIX (AFDMC) [132]	0.47(3)	865.8(55.3)
AV18+UIX (FHNC) [26, 138]	0.69	589.8
AV18 (CBF) [138]	0.88	462.4

Table 4.2: Compressibility in PNM. The results of this work are denoted as AV8'+UIX and EFT for the Argonne-Urbana and chiral EFT interactions, respectively. AV6' calculation is the result obtained by Fantoni *et al.* [132] with AFDMC in previous work. BKR is the result obtained fitting Brueckner-HF calculations employing the Bressel-Kerman-Rouben potential, as reported by J.W. Clark *et al.* in Ref. [139]. AV18 (CBF) is the Correlated Basis Functions of Benhar *et al.* from Ref. [138]. AV18+UIX (FHNC) is the Fermi Hyper-Netted Chain of Akmal and Pandharipande [26]. BHF, Skyrme, and QHD are Brueckner-Hartree-Fock, Skyrme force-based Hartree-Fock (HF) and Quantum Hydrodynamical calculations respectively as reported in the paper from Aguirre *et al.* in Ref. [137].

interesting to compare the values obtained by the Correlated Basis Function (CBF) calculations of Benhar *et al.* [138], employing a two-body interaction only, to our results obtained with the Argonne-Urbana potential. The latter results are higher of about a factor of 2. However, this discrepancy is substantially reduced when

comparing to the Fermi Hyper-Netted Chain (FHNC) results of Akmal and Pandharipande [26], essentially employing the same potential. Results obtained with chiral EFT tend instead to be closer to the other values reported in the literature, and in particular, to the results coming from HF or Brueckner-HF calculations. All these discrepancies point to the fact that a more systematic and homogeneous comparison between different approaches is definitely in order.

4.5 MAGNETIC SUSCEPTIBILITY

A quantity, which is especially relevant for supernovae explosions and neutron star mergers, is the magnetic susceptibility. This quantity can be directly computed from AFDMC calculations.

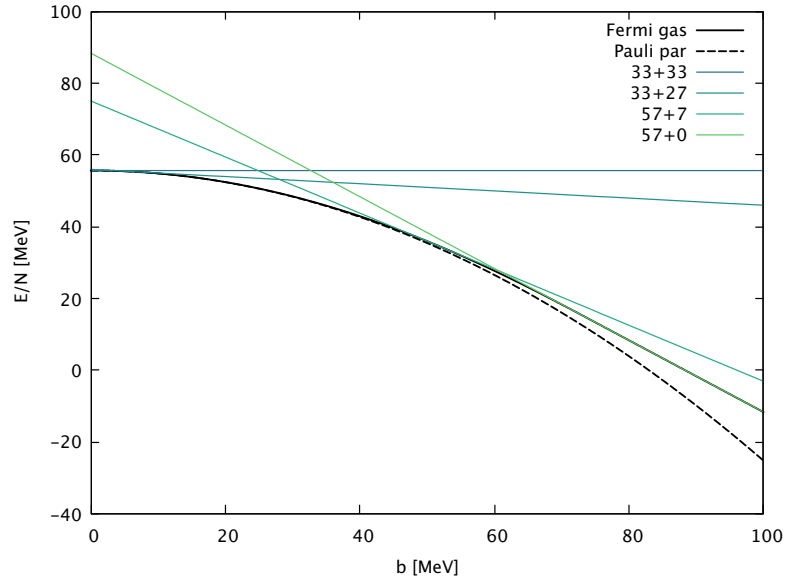


Figure 4.14: Energy per particle for the free system as a function of the external magnetic field b at two times saturation density $\rho = 0.32 \text{ fm}^{-3}$. The results for different closed-shell configurations with a total neutron number of ~ 60 are plotted in solid lines. The analytic result for the free Fermi gas is plotted in full black line. The approximation of the Pauli parabola is displayed in dashed lines.

These kind calculations were already performed by Fantoni et al. [132]. In their calculations PBC were implemented, and therefore only closed-shell configurations could be used, as explained in Section 3.2 and reported in Figure 4.14.

For a given external magnetic field b , the intersection between the analytic solution of the free Fermi gas and the solution of the closed-shell configuration gives the ground state spin asymmetry for the free system. In principle, the same ground-state spin asymmetry cannot be assumed for the interacting system, but it was the best possible guess. In addition, only a very limited number of spin asymmetries with a similar total number of particles could be analyzed. The main difference from this previous work is that we fixed an external magnetic field and then studied the energy per particle of the interacting system with different spin polarization, keeping the total number of particles fixed. This is achieved using twist-averaged boundary conditions (TABC). The Hamiltonian of the system with an external magnetic field can be written as:

$$H = H_0 - \sum_i \vec{\sigma}_i \cdot \vec{b}, \quad (4.18)$$

where $\vec{b} = \mu \vec{B}$ is the external field, $\vec{\sigma}_i$ is the spin of the i -th particle, and $\mu = 6.030774 \times 10^{-18}$ MeV/G is the Bohr magneton. H_0 is the Hamiltonian of the interacting system without the external magnetic field. Following the steps of Ref. [132], the magnetic susceptibility is defined as:

$$\chi = -\rho \mu^2 \left. \frac{\partial^2 E_0(b)}{\partial b^2} \right|_{b=0}, \quad (4.19)$$

where ρ is the density and $E_0(b)$ is the ground state energy for a given external field b . To evaluate the second derivative, we use the Pauli expansion as a function of spin polarization ξ , which is defined as:

$$\xi = -\partial E_0(b) / \partial b|_{b=0}, \quad (4.20)$$

and we obtain:

$$E(\xi) = E(0) - b\xi + \frac{1}{2}\xi^2 E''(0). \quad (4.21)$$

The magnetic susceptibility is obtained first minimizing $E(\xi)$ with respect to ξ as:

$$\chi = \mu^2 \rho \frac{1}{E''(0)}, \quad (4.22)$$

and, using the chain rule, rewriting the second derivative of the energy as:

$$E''(0) = \left[\frac{\partial \xi}{\partial J_z} \right]^{-2} \left\{ \frac{\partial^2 E_0}{\partial J_z^2} - \frac{\partial E_0}{\partial J_z} \left[\frac{\partial \xi}{\partial J_z} \right]^{-1} \frac{\partial^2 \xi}{\partial J_z^2} \right\}. \quad (4.23)$$

This expression can be further simplified recalling that $\partial E_0 / \partial J_z = 0$, since we are looking at the ground state (i.e. the minimum of the energy), with respect to the spin asymmetry J_z , obtaining:

$$E''(0) = \left[\frac{\partial \xi}{\partial J_z} \right]^{-2} \frac{\partial^2 E_0}{\partial J_z^2} \quad (4.24)$$

The derivatives can be expanded and computed in terms of AFDMC energies as:

$$\frac{\partial \xi}{\partial J_z} \approx \frac{E_0(J_z = J_{z0}, b = 0) - E_0(J_z = J_{z0}, b = b_0)}{J_{z0} b_0}, \quad (4.25)$$

where $E_0(J_z = J_{z0}, b = 0)$ and $E_0(J_z = J_{z0}, b = b_0)$ are the ground state energies for the system with no external magnetic field and with a fixed external magnetic field b_0 respectively. The spin asymmetry J_{z0} is the spin asymmetry of the ground state of the system for a given external magnetic field b_0 . The second derivative can be written as:

$$\frac{\partial^2 E_0}{\partial J_z^2} \approx 2 \frac{E_0(J_z = J_{z0}, b = 0) - E_0(J_z = 0, b = 0)}{J_{z0}^2}, \quad (4.26)$$

where $E_0(J_z = 0, b = 0)$ is the ground state energy of the unpolarized system with no magnetic field. The validity of these expressions relies on the following assumptions:

- (i) for $b = 0$, $E_0(J_z, b)$ is quadratic in J_z (see Figure 4.15);
- (ii) for a fixed J_z , $E_0(J_z, b)$ is linear in b (see Figure 4.16);
- (iii) the polarization is linear in J_z .

These assumptions become exact in the limit of an infinite system with J_z and b small. We tested the validity of these assumptions and the results are reported in Figure 4.15 and Figure 4.16. As an example, we report the results for the phenomenological potential AV8'+UIX.

The AFDMC calculations have been carried out with 38 neutrons in a periodic box using TABC over seven different spin polarizations ξ .

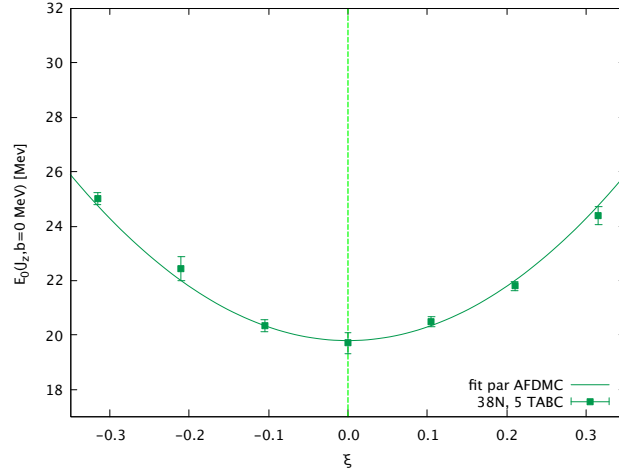


Figure 4.15: AFDMC results of the energy per particle for PNM $E_0(J_z, b)$ at saturation density with seven different spin polarization ξ with no external magnetic field. The errorbar represents the statistical errors of the AFDMC calculations. The vertical dashed line shows the polarization of the ground state obtained from the analytic result for the free Fermi gas. The solid line is a parabolic fit to the AFDMC results.

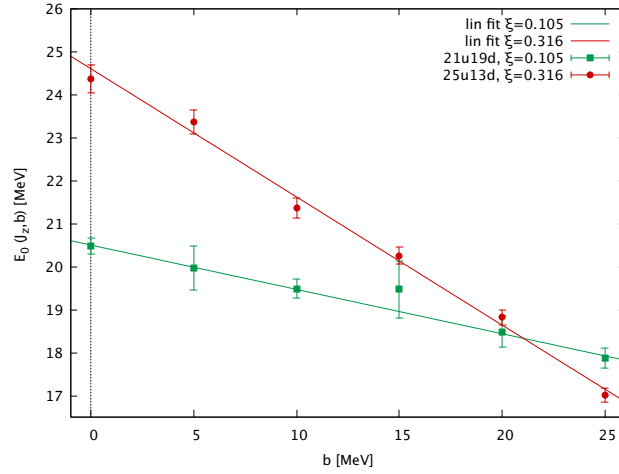


Figure 4.16: Energy per particle $E_0(J_z, b)$ at saturation density at fixed spin asymmetry J_z as a function of the external magnetic field b in two different cases: in red 21 neutrons with spin up N_\uparrow (u in the legend) and 19 neutrons with spin down N_\downarrow (d in the legend) and in green 25 N_\uparrow and 13 N_\downarrow , which corresponds to a spin asymmetry of $\xi \sim 0.105$ and $\xi \sim 0.316$ respectively. Solid lines are the linear fits to show the validity of assumption (ii).

For each spin asymmetry, we choose 5 different twist vectors, and we average on the results of the different runs.

In Figure 4.17 we report the results of the energy per particle as a function of the spin asymmetry for a given external magnetic field at saturation density.

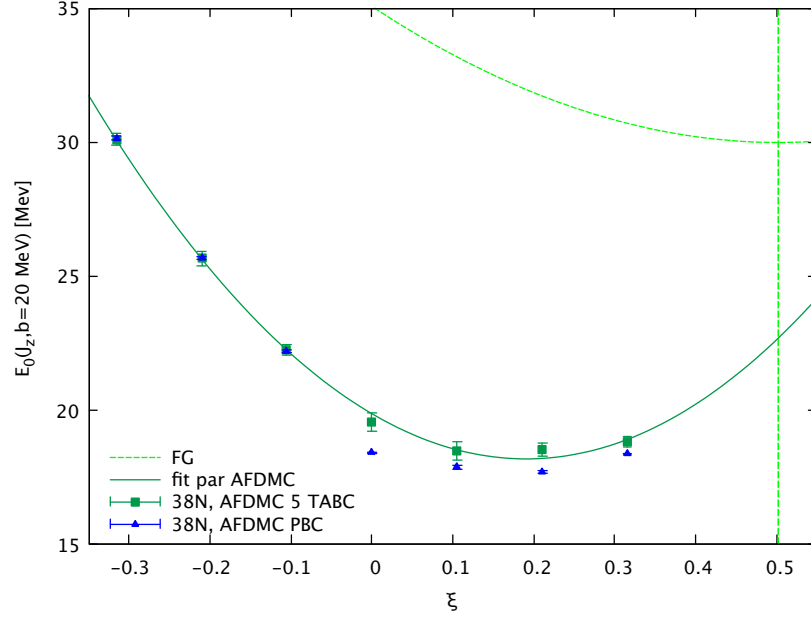


Figure 4.17: AFDMC results of the energy per particle for PNM $E_0(J_z, b)$ at saturation density with seven different spin polarization ξ with external magnetic field $b = 20$ MeV. The errorbars represent the statistical errors of the AFDMC calculations. Green squares and blue triangles indicate the AFDMC results using twist-averaged boundary conditions (TABC) and periodic boundary conditions (PBC), respectively. The dashed line shows the analytic result for the free Fermi gas and the predicted ground state spin polarization. The solid line is a parabolic fit to the AFDMC results.

As an example, we report the case of the phenomenological AV8'+UIX potential, though the chiral potentials share the same features. The AFDMC results are fitted to a parabola in order to determine ground state spin polarization and energy. It is interesting to point out that the ground state spin polarization is reduced with respect to the one predicted by the non-interacting case. The same behavior can also be seen at higher magnetic fields. It is clear from Figure 4.17

that calculations with PBC are not sufficient to determine the correct ground state energy and spin polarization.

We used two different approaches to derive the magnetic susceptibility:

- (i) we perform a parabolic fit on the energy per particle $E_0(J_z, b)$ as a function of the spin polarization ξ (as shown in Figures 4.15 and 4.17) for any chosen external magnetic field. We compute the magnetic susceptibility from the approximate expressions of Equation (4.25) and Equation (4.26). The ground state spin asymmetry J_{z0} and energies entering Equation (4.25) and Equation (4.26) are derived from the parabolic fits;
- (ii) we compute the ground state J_{z0} as in approach (i) and perform a linear fit of ξ_0 as a function of the external magnetic field B , relying on the fact that for small spin polarization they are proportional. The magnetic susceptibility is directly computed from Equation (4.19).

The results are obtained both from the phenomenological potential and the local chiral potential.

Approach (i). For each density and for each external field we compute the spin polarization of the ground state as shown in Figure 4.15 and Figure 4.17. For each density, we choose five non-zero external magnetic fields in a region where the ground state spin polarization as a function of the external magnetic field is linear for the analytic result of the non-interacting system. An example with three different densities is shown in Figure 4.18.

In addition, we also perform a calculation with no external magnetic field. The results obtained from the fits are inserted in Equation (4.25) and Equation (4.26), and for each external magnetic field, we obtain a value for the magnetic susceptibility of the system. We propagate the uncertainties on the parameters from the fitting procedures, and the final result for the magnetic susceptibility is the average of the different values we obtain from the external magnetic fields. As an example, we report in Figure 4.19 the results for the case of the phenomenological potential AV8'+UIX at 0.08, 0.16 and 0.32 fm⁻³.

In principle, each magnetic field, unless not too high, should give the correct value of the magnetic susceptibility. The uncertainties on the parameters from

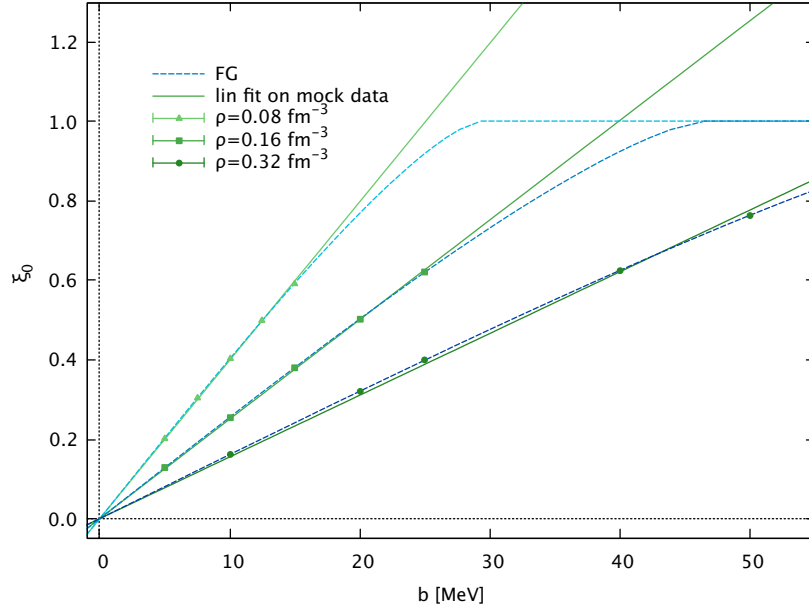


Figure 4.18: Ground state spin polarization ξ_0 as a function of the external magnetic field b for the free Fermi gas. Blue dashed lines are the analytic result for three different densities. Green full lines are the results of the linear fit on the chosen five external magnetic fields indicated by triangles, squares, and circles, labeled as "mock data". Low to high densities are in light to dark colors.

the fitting procedure are not small, so we decided to average on five different magnetic fields to obtain an accurate estimate for the magnetic susceptibility.

Within this approach, VMC and AFDMC calculations give very similar results. In fact, in Equation (4.25) and Equation (4.26) we compute differences of energies. If we compare VMC and AFDMC results, these differences are almost the same, because AFDMC results are systematically lower by some fixed amount than VMC calculations. The results are similar to the ones obtained by Fantoni *et al.* [132] but not always compatible. On the other hand, we are computing the energies entering Equation (4.25) and Equation (4.26) in the correct ground state spin polarization of the interacting system. As a consistency check, we take our results and compute the magnetic susceptibility starting from the ground state spin polarization predicted by the analytical result for the free Fermi gas. It is remarkable that in this way, we recover the same results of Ref. [132]. The results are reported in Table 4.3.

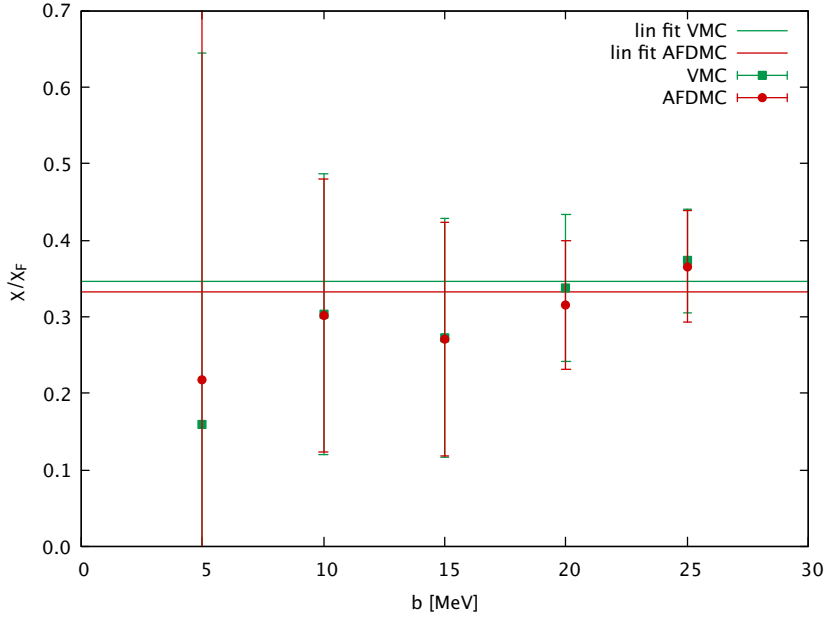


Figure 4.19: Magnetic susceptibility ratio with respect to the free Fermi gas result at saturation density for five different external magnetic fields. For a noninteracting Fermi gas the spin susceptibility is $\chi_F = \mu^2 m k_F / (\hbar^2 \pi^2)$. The results are obtained with the approach (i) described in the text. AFDMC results are plotted in red. We also report the results obtained from the VMC calculations in green. Uncertainties on the parameters from the parabolic fits have been propagated and are shown as errorbars.

ρ/ρ_0	AV6'+UIX [132]	AV8'+UIX [132]	AV8'+UIX (*)	AV8'+UIX
0.50			0.40(2)	0.45(2)
0.75	0.40(1)		0.42(3)	0.45(3)
1.00			0.39(2)	0.33(2)
1.25	0.37(1)	0.39(1)	0.36(2)	0.38(1)
2.00	0.33(1)	0.35(1)	0.34(2)	0.31(1)
2.50	0.30(1)		0.29(2)	0.30(1)

Table 4.3: Magnetic susceptibility ratio χ/χ_F for pure neutron matter interacting with the phenomenological potential AV8'+UIX. For a noninteracting Fermi gas the spin susceptibility is $\chi_F = \mu^2 m k_F / (\hbar^2 \pi^2)$. AV8'+UIX (*) are the results taking as spin polarization of the ground state ξ_0 the free Fermi gas prediction. We compare our results to the results of Ref. [132].

Approach (ii). Instead of using the approximate expression of approach (i) to compute the magnetic susceptibility, we can now also directly compute it from Equation (4.19). As an example to explain the procedure, we report in Figure 4.20 the case of the phenomenological potential $AV8'+UIX$ at three different densities. We perform a linear fit of the ground state spin polarization ξ_0 as a

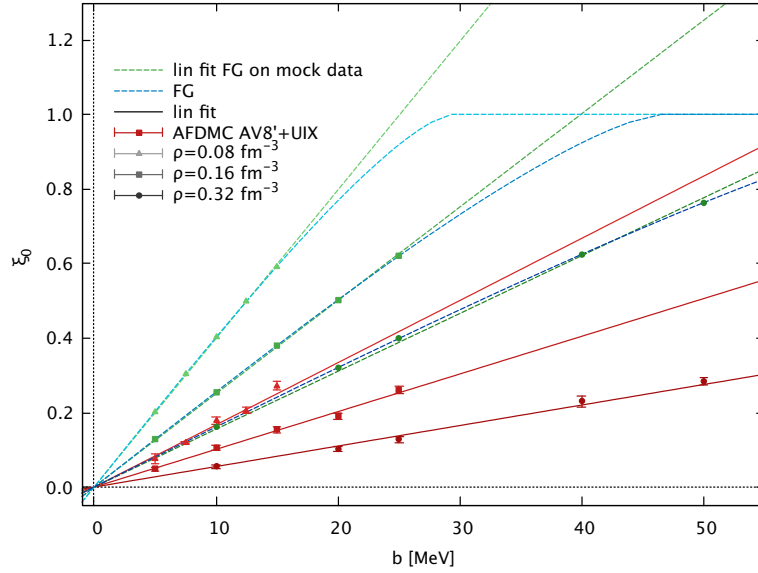


Figure 4.20: Ground state spin polarization ξ_0 as a function of the external magnetic field b for the free Fermi gas. Blue dashed lines are the analytic result for three different densities. Green dashed lines are the results of the linear fit on the chosen five external magnetic fields indicated by triangles, squares, and circles, labeled as "mock data". Low to high densities are in light to dark colors. This is analogous to what is reported in Figure 4.18. In addition, we report in red the AFDMC results for the interacting system in the case of the phenomenological potential $AV8'+UIX$ and the respective linear fits.

function of the external magnetic field b . The values of ξ_0 are obtained from the parabolic fits explained in the approach (i). Using Equation (4.20) and inserting it in Equation (4.19), we can directly compute the magnetic susceptibility.

In Figure 4.21 we report a summary of the results for the magnetic susceptibility of the interacting system obtained in the case of the phenomenological $AV8'+UIX$ and the local chiral effective field theory potential EFT. The calculations of the phenomenological potential are also compared between the two approaches. Al-

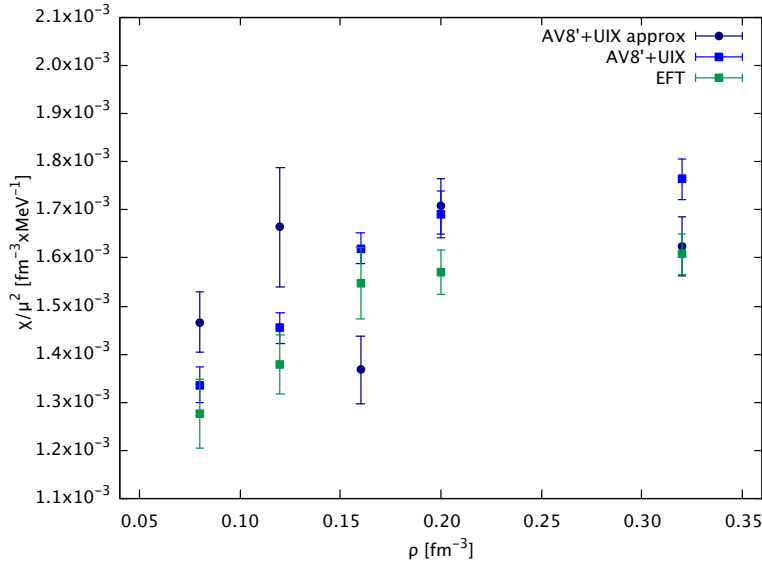


Figure 4.21: Magnetic susceptibility as a function of the density ρ . Results for the phenomenological potential (AV8'+UIX) and the local chiral potential (EFT) are plotted with blue and green symbols, respectively. The results of the approach (i) are denoted with circles and labeled as "approx". Uncertainties on the parameters from the fits have been propagated and are shown as error bars.

though not significantly different, the two approaches are not always compatible. The reason might be related to the approximations of approach (i), while in approach (ii), the only source of uncertainty is directly connected to the linear fit. The approximation of approach (ii) is investigated in Figure 4.22.

In Figure 4.22, the magnetic susceptibility of the interacting system is compared to the analytical solution of the free Fermi gas. We also compare the linear fit results for the non-interacting case to the correct analytical result. At low densities, the linear fit reproduces the full result correctly, while at high densities, the predicted magnetic susceptibilities slightly underestimate the correct results. There is no reason to expect different behavior in the case of the interacting system, although the correct result is unknown.

In Figure 4.23 we compare the magnetic susceptibility ratio with respect to the free Fermi gas that we obtained within the approach (ii) to the results available in the literature. The calculations have been performed with another microscop-

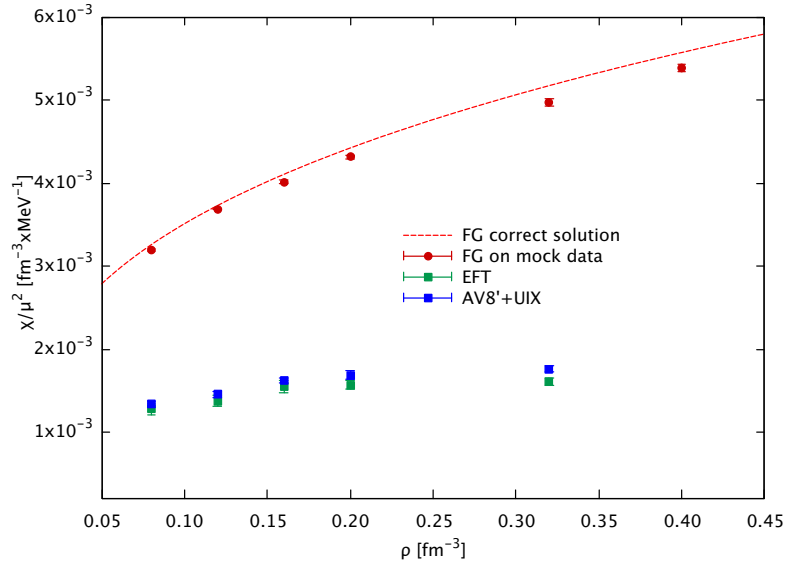


Figure 4.22: Magnetic susceptibility as a function of the density ρ . Results from the approach (ii) for the phenomenological potential (AV8'+UIX) and the local chiral potential (EFT) are plotted with blue and green symbols, respectively. The analytic solution for the non-interacting system (red-dashed lines) is compared to the linear fit on the "mock data" (red circles), as explained in the text. Uncertainties on the parameters from the fits have been propagated and are shown as errorbars.

ical method used in nuclear physics, which is Brueckner-Hartree Fock (BHF). In black, we report the calculations by Bombaci *et al.* [121] for the two-body potential AV18. The results of Vidaña *et al.* [140] were obtained using again AV18 for the two-body interaction, but with the addition of the UIX three-body force and are plotted with two different bands. The results from Ref. [140] are shown as bands to represent the uncertainty from the extrapolation procedure. The orange band shows the result, where a new parameterization has been performed when large values of spin polarization are considered, as explained in Ref. [140]. The new parameterization gives results which are in agreement with the results of Ref. [132] and the results of this work, as reported in Figure 4.23. A comparison between the two microscopical methods was already done in Ref. [141], but only for the case of the Nijmegen II and Reid93 potentials.

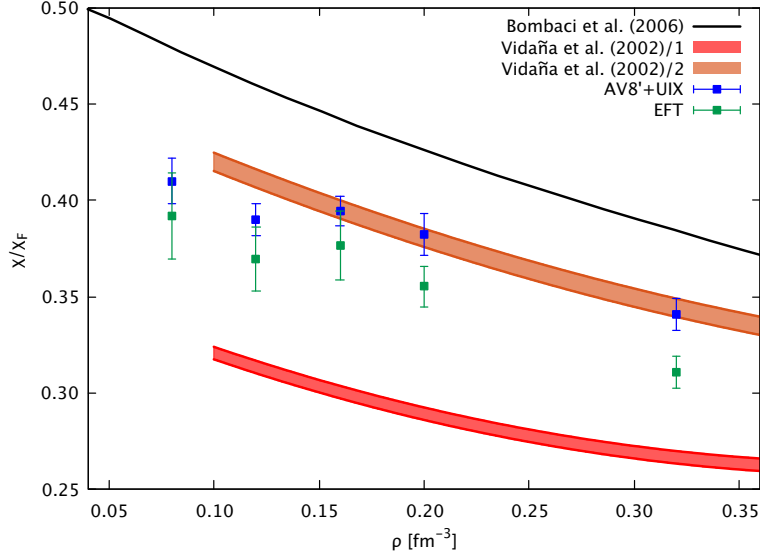


Figure 4.23: χ/χ_F as a function of the density. For a noninteracting Fermi gas the spin susceptibility is $\chi_F = \mu^2 m k_F / (\hbar^2 \pi^2)$. Results for the phenomenological (AV8'+UIX) and local chiral effective field theory (EFT) potential obtained with approach (ii) are plotted in blue and green, respectively. The solid black line shows the calculations of Ref. [121] for the two-body interaction AV18. Results from Ref. [140] with AV18 plus UIX three-body force with Brueckner Hartree Fock (BHF) methods are plotted as bands. The original result is plotted with a red band, while the orange band shows the calculation with a new parameterization, which has been done in Ref. [140], when high spin polarizations are considered.

4.5.1 Spin-symmetry energy

Apart from the two approaches described up to now, we can estimate the magnetic susceptibility also starting from the EOS of the fully polarized and fully unpolarized system, which we reported in Figure 4.1. In analogy to the symmetry energy, we can introduce the spin-symmetry energy (SSE), which is defined as the difference between the energy of the fully spin-polarized system and the spin unpolarized system. If we employ the energy functional described in Equation (4.5), the second derivative of the energy with respect to the spin polarization in the definition of the magnetic susceptibility of Equation (4.19) reduces to two times the spin-symmetry energy. Within this new approach, we report the spin-symmetry energy for the phenomenological and the chiral potential in Figure 4.24. The AFDMC calculations of the EOS for the fully spin-polarized and unpolarized system are those presented in Figure 4.1.

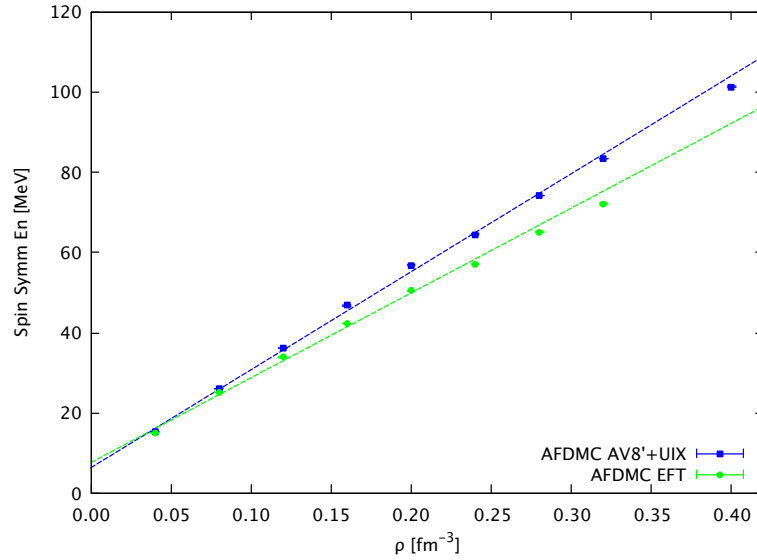


Figure 4.24: AFDMC results for spin-symmetry energy (SSE). The results for the phenomenological AV8'+UIX and the local chiral effective field theory (EFT) potential are plotted in blue and green, respectively. The dashed lines represent a linear fit to the AFDMC calculations.

The SSE is slightly higher for the phenomenological potential than the local chiral potential. Although this is a very simplified approach, the results for the

spin-symmetry energy reported in Figure 4.25 are not far from the results obtained from approach (ii). The magnetic susceptibility for the free Fermi gas is roughly a factor ~ 3 higher than for the interacting case. In contrast, the rough estimate from the spin-symmetry energy gives results closer to the full analysis of approach (ii).

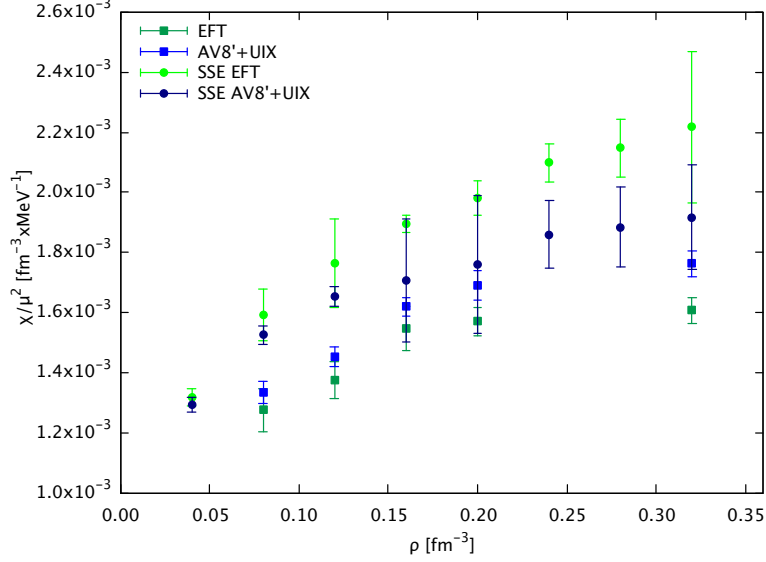


Figure 4.25: Comparison of the magnetic susceptibility obtained from approach (ii) (squares) and the spin-symmetry energy (circles). Phenomenological (AV8'+UIX) and local chiral effective field theory (EFT) potential are plotted in blue and green respectively.

CONCLUSIONS

*I*n this thesis, we focused on the main properties of spin-polarized pure neutron matter. The expected spin polarization of dense neutron matter, although low, might have effects and implications in high energy phenomena such as neutron star mergers and supernovae explosions. Starting from realistic and modern many-body interactions, we used AFDMC to study the EOS for both fully spin-polarized and fully spin unpolarized systems. We considered the phenomenological potential AV8'+UIX and a local chiral effective field theory potential up to N2LO. For the chiral potential, we evaluate theoretical uncertainties estimates, and they have been propagated to the evaluation of the neutrino mean free paths and the compressibilities. Since the evaluation of the response function at the moment is not feasible within quantum Monte Carlo (QMC) methods, we relied on a mean-field approximation, namely time-dependent local spin density approximation (TDLSDA). We showed that this approximation is reliable, and we computed the neutrino mean free paths in partially spin-polarized dense neutron matter. The robustness of the mean-field approach has also been checked. We compute the compressibility of partially spin-polarized PNM and compare our results to the ones available in the literature with different approaches. In addition, the implications of the use of effective mass have been discussed.

At the moment, the calculations have been performed only at $T = 0$. In principle, temperature effects are not negligible to study supernovae explosions, and neutron star mergers and the inclusion of these effects should be taken into account. A first attempt and straightforward extension would be to include the temperature-dependence in the response functions of the free Fermi gas, within

the TDLSDA. A comprehensive treatment would be starting from a temperature-dependent EOS and thus the inclusion of the temperature in the AFDMC calculations. Up to now, only a few attempts to include temperature-effects within QMC methods have been made. Another extension of this work would be to include also protons. Although only a small fraction of protons is present in the outer core of neutron stars, the presence of protons allows more responses of the system. It would be interesting to extend the formalism of the local density approximation to study responses in partially polarized systems both in spin and isospin channels simultaneously. A future hope would be to study response functions consistently, including also temperature effects, directly within the AFDMC method.

In addition, we successfully applied the twist-averaged boundary conditions (TABC) to reduce finite-size effects. We applied TABC to the study of partially spin-polarized systems, and the magnetic susceptibility of PNM has been computed. We showed that for a given external magnetic field, the ground state polarization of the interacting system is lower than the one predicted by the analytic solution for the free system. We found good agreement with previous calculation with AFDMC, even if, in principle, previous calculations used the as ground-state polarization the one predicted from the free Fermi gas. The results for the phenomenological potential are in agreement with previous results obtained from different microscopical methods. The magnetic susceptibility has also been computed for the recent local chiral effective field theory interactions. It would be interesting to look at the effects and the impact of these studies on the spin polarization of pure neutron matter in neutron star merger and supernovae explosions simulations.

BIBLIOGRAPHY

- [1] Cromartie H.T. *et al.*, Relativistic Shapiro delay measurements of an extremely massive millisecond pulsar, *Nature Astronomy* (2019), **doi:** 0.1038/s41550-019-0880-2
- [2] Abbot B.P. *et al.*, Observation of Gravitational Waves from a Binary Black Hole Merger, *Phys. Rev. Lett.* (2016), **116** 061102
- [3] Einstein A., Näherungsweise Integration der Feldgleichungen der Gravitation, *Sitzungsberichte der Königlich Preussischen Akademie der Wissenschaften zu Berlin* (1916), **link:** <https://archive.org/details/sitzungsberichte1916deutsch>
- [4] Abbot B.P. *et al.*, GW170817: Observation of Gravitational Waves from a Binary Neutron Star Inspiral, *Phys. Rev. Lett.* (2017), **119** 161101
- [5] Abbot B.P. *et al.*, GW190425: Observation of a Compact Binary Coalescence with Total Mass $\sim 3.4M_{\odot}$, (2019), arXiv:2001.017616
- [6] Baade W. and Zwicky F., Remarks on Super-Novae and Cosmic Rays, *Phys. Rev.* (1934), **46** 76
- [7] Baade W. and Zwicky F., Cosmic Rays from Super-Novae, *Proceedings of the National Academy of Sciences* (1934), **20** (5) 259
- [8] Chadwick J., Possible Existence of a Neutron, *Nature* (1932), **129** 312
- [9] Chadwick J., The Existence of a Neutron, *Proceedings of the Royal Society A: Mathematical, Physical and Engineering Sciences* (1932), **136** 632
- [10] Tolman R.C., Static Solutions of Einstein's Field Equations for Spheres of Fluid, *Phys. Rev.* (1939), **55** 364

Bibliography

- [11] Oppenheimer J.R. and Volkoff G.M., On Massive Neutron Core, *Phys. Rev.* (1939), **55** 374
- [12] D’Aì A. *et al.*, Evidence for the magnetar nature of 1E 161348–5055 in RCW 103, *Monthly Notices of the Royal Astronomical Society* (2016), **463** 2394
- [13] Hessels J.W.T. *et al.*, A Radio Pulsar Spinning at 716 Hz, *Science* (2006), **311** 1901
- [14] Woods P.M. *et al.*, The Prelude to and Aftermath of the Giant Flare of 2004 December 27: Persistent and Pulsed X-Ray Properties of SGR 1806-20 from 1993 to 2005, *The Astrophysical Journal* (2007), **654** 470
- [15] Karako-Argaman C. *et al.*, DISCOVERY AND FOLLOW-UP OF ROTATING RADIO TRANSIENTS WITH THE GREEN BANK AND LOFAR TELESCOPES, *The Astrophysical Journal* (2007), **809** 67
- [16] Steiner A.W., Lattimer J.M. and Brown E.F., Neutron star radii, universal relations, and the role of prior distributions, *The European Physical Journal A* (2016), **52** 18
- [17] Steiner A.W., Gandolfi S., Fattoyev, F.J. and Newton W.G., Neutron star radii, universal relations, and the role of prior distributions, *Phys. Rev. C* (2015), **91** 015804
- [18] Gandolfi S. *et al.*, From the microscopic to the macroscopic world: from nucleons to neutron stars, *Journal of Physics G: Nuclear and Particle Physics* (2019), **46** 103001
- [19] Manchester R.N., Hobbs G.B., Teoh A. and Hobbs M., The Australia Telescope National Facility Pulsar Catalogue, *The Astronomical Journal* (2005), **129** 1993
- [20] Lattimer J.M., The Nuclear Equation of State and Neutron Star Masses, *Annual Review of Nuclear and Particle Science* (2012), **62** 485
- [21] Riley T.E. *et al.*, A NICER View of PSR J0030+0451: Millisecond Pulsar Parameter Estimation, *The Astrophysical Journal Letters* (2019), **887** L21

- [22] Raaijmakers G. *et al.*, A Nicer View of PSR J0030+0451: Implications for the Dense Matter Equation of State, *The Astrophysical Journal Letters* (2019), **887** L22
- [23] Miller M.C. *et al.*, PSR J0030+0451 Mass and Radius from NICER Data and Implications for the Properties of Neutron Star Matter, *The Astrophysical Journal Letters* (2019), **887** L24
- [24] Prakash M., Ainsworth T.L. and Lattimer J.M., Equation of State and the Maximum Mass of Neutron Stars, *Phys. Rev. Lett.* (1988), **61** 2518
- [25] Douchin F. and Haensel P., A unified equation of state of dense matter and neutron star structure, *Phys. Rev. Lett.* (2001), **380** 151
- [26] Akmal A., Pandharipande V.R. and Ravenhall D.G., Equation of state of nucleon matter and neutron star structure, *Phys. Rev. C* (1998), **58** 1804
- [27] Wiringa R.B., Fiks V. and Fabrocini A., Equation of state for dense nucleon matter, *Phys. Rev. C* (1988), **38** 1010
- [28] Engvik L., Osnes E., Hjorth-Jensen M., Bao G. and Ostgaard E., Asymmetric Nuclear Matter and Neutron Star Properties, *The Astrophysical Journal* (1996), **469** 794
- [29] Mütter H., Prakash M. and Ainsworth T.L., The nuclear symmetry energy in relativistic Brueckner-Hartree-Fock calculations, *Physics Letters B* (1987), **199** 469
- [30] Fattoyev F.J., Horowitz C.J., Piekarewicz J. and Shen G., Relativistic effective interaction for nuclei, giant resonances, and neutron stars, *Phys. Rev. C* (2010), **82** 055803
- [31] Müller H. and Serot B.D., Relativistic mean-field theory and the high-density nuclear equation of state, *Nuclear Physics A* (1996), **606** 508
- [32] Lackey B.D., Nayyar M. and Owen B.J., Observational constraints on hyperons in neutron stars, *Phys. Rev. D* (2006), **73** 024021

Bibliography

- [33] Glendenning N.K. and Moszkowski S.A., Reconciliation of neutron-star masses and binding of the Λ in hypernuclei, *Phys. Rev. Lett.* (1991), **67** 2414
- [34] Glendenning N.K. and Schaffner-Bielich J., First order kaon condensate, *Phys. Rev. C* (1999), **60** 025803
- [35] Prakash M., Cooke J.R. and Lattimer J.M., Quark-hadron phase transition in protoneutron stars, *Phys. Rev. D* (1995), **52** 661
- [36] Lattimer J.M. and Prakash M., Neutron Star Structure and the Equation of State, *The Astrophysical Journal* (2001), **550** 426
- [37] Demorest P.B. *et al.*, A two-solar-mass neutron star measured using Shapiro delay, *Nature* (2010), **467** 1081
- [38] Fonseca E. *et al.*, THE NANO GRAV NINE-YEAR DATA SET: MASS AND GEOMETRIC MEASUREMENTS OF BINARY MILLISECOND PULSARS, *The Astrophysical Journal* (2016), **832** 167
- [39] Arzoumanian Z. *et al.*, The NANOGrav 11-year Data Set: High-precision Timing of 45 Millisecond Pulsars, *The Astrophysical Journal Supplement Series* (2018), **235** 37
- [40] Antoniadis J. *et al.*, A Massive Pulsar in a Compact Relativistic Binary, *Science* (2013), **340** 6131
- [41] Wiringa R.B., Stoks V.G.J. and Schiavilla R., Accurate nucleon-nucleon potential with charge-independence breaking, *Phys. Rev. C* (1995), **51** 38
- [42] Pudliner B.S. *et al.*, Quantum Monte Carlo calculations of nuclei with $A \lesssim 7$, *Phys. Rev. C* (1997), **56** 1720
- [43] Wiringa R. B. and Pieper S.C., Evolution of Nuclear Spectra with Nuclear Forces, *Phys. Rev. Lett.* (2002), **89** 182501
- [44] Gezerlis A. *et al.*, Quantum Monte Carlo Calculations with Chiral Effective Field Theory Interactions, *Phys. Rev. Lett.* (2013), **111** 032501

- [45] Gezerlis A. *et al.*, Local chiral effective field theory interactions and quantum Monte Carlo applications, *Phys. Rev. C* (2014), **90** 054323
- [46] Tews I., Gandolfi S., Gezerlis A. and Schwenk A., Quantum Monte Carlo calculations of neutron matter with chiral three-body forces, *Phys. Rev. C* (2016), **93** 024305
- [47] Lynn J.E. *et al.*, Chiral Three-Nucleon Interactions in Light Nuclei, Neutron- α Scattering, and Neutron Matter, *Phys. Rev. Lett.* (2016), **116** 062501
- [48] Gandolfi S. *et al.*, Microscopic calculation of the equation of state of nuclear matter and neutron star structure, *Monthly Notices of the Royal Astronomical Society: Letters* (2010), **404** L30
- [49] Lonardonì D., Lovato A., Gandolfi S. and Pederiva F., Hyperon Puzzle: Hints from Quantum Monte Carlo Calculations, *Phys. Rev. Lett.* (2015), **114** 092301
- [50] Gandolfi S., Gezerlis A. and Carlson J., Neutron Matter from Low to High Density, *Annual Review of Nuclear and Particle Science* (2015), **65** 303
- [51] Møller P., Nix J.R., Myers W.D. and Swiatecki W.J., Nuclear Ground-State Masses and Deformations, *Atomic Data and Nuclear Data Tables* (1995), **59** 185
- [52] Raithel C.A., Özel F. and Psaltis D., Tidal Deformability from GW170817 as a Direct Probe of the Neutron Star Radius, *The Astrophysical Journal* (2018), **857** L23
- [53] Abbott B.P. *et al.* Properties of the Binary Neutron Star Merger GW170817, *Phys. Rev. X.* (2019), **9** 011001
- [54] Coughlin M. W., Dietrich T., Margalit B. and Metzger B.D. Multimessenger Bayesian parameter inference of a binary neutron star merger, *Monthly Notices of the Royal Astronomical Society: Letters* (2019), **489** L91
- [55] Lattimer J.M. and Steiner A.W., Constraints on the symmetry energy using the mass-radius relation of neutron stars, *The European Physical Journal A* (2014), **50** 40

Bibliography

- [56] Lattimer J.M. and Lim Y., CONSTRAINING THE SYMMETRY PARAMETERS OF THE NUCLEAR INTERACTION, *The Astrophysical Journal* (2013), **771** 51
- [57] Tews I., Lattimer J.M., Ohnishi A. and Kolomeitsev E.E., Symmetry Parameter Constraints from a Lower Bound on Neutron-matter Energy, *The Astrophysical Journal* (2017), **848** 105
- [58] Oertel M., Hempel M., Klähn T. and Typel S., Equations of state for supernovae and compact stars, *Rev. Mod. Phys.* (2017), **89** 015007
- [59] Carson Z., Steiner A.W. and Yagi K., Constraining nuclear matter parameters with GW170817, *Phys. Rev. D* (2019), **99** 043010
- [60] Raithel C.A., Özel F. and Psaltis D., Measurement of the Nuclear Symmetry Energy Parameters from Gravitational-wave Events, *The Astrophysical Journal* (2019), **885** 121
- [61] Bauswein A., Just O., Janka H.-T., Stergioulas N., Neutron-star Radius Constraints from GW170817 and Future Detections, *The Astrophysical Journal Letters* (2017), **850** L34
- [62] Fattoyev J., Piekarewicz J. and Horowitz C.J., Neutron Skins and Neutron Stars in the Multimessenger Era, *Phys. Rev. Lett.* (2018), **120** 172702
- [63] Most E.R., Weih L.R., Rezzolla L. and Schaffner-Bielich J., New Constraints on Radii and Tidal Deformabilities of Neutron Stars from GW170817, *Phys. Rev. Lett.* (2018), **120** 26110
- [64] Lim Y. and Holt J.W., Neutron Star Tidal Deformabilities Constrained by Nuclear Theory and Experiment, *Phys. Rev. Lett.* (2018), **121** 062701
- [65] De S. *et al.* Tidal Deformabilities and Radii of Neutron Stars from the Observation of GW170817 *Phys. Rev. Lett.* (2018), **121** 091102
- [66] Malik T. *et al.* GW170817: Constraining the nuclear matter equation of state from the neutron star tidal deformability *Phys. Rev. C* (2018), **98** 035804

- [67] Abbot B.P. *et al.* GW170817: Measurements of Neutron Star Radii and Equation of State *Phys. Rev. Lett.* (2018), **121** 161101
- [68] Tews I., Margueron J. and Reddy S., Critical examination of constraints on the equation of state of dense matter obtained from GW170817 *Phys. Rev. C* (2018), **98** 045804
- [69] Köppel S., Bovard L. and Rezzolla L., A General-relativistic Determination of the Threshold Mass to Prompt Collapse in Binary Neutron Star Mergers *The Astrophysical Journal Letters* (2019), **872** L16
- [70] Raithel C.A., Constraints on the neutron star equation of state from GW170817 *The European Physical Journal A* (2019), **55** 80
- [71] Annala E., Gorda T., Kurkela A. and Vuorinen A., Gravitational-Wave Constraints on the Neutron-Star-Matter Equation of State *Phys. Rev. Lett.* (2018), **120** 172703
- [72] Montaña G., Tolós L., Hanauske M. and Rezzolla L., Constraining twin stars with GW170817 *Phys. Rev. D* (2019), **99** 103009
- [73] Radice D. and Dai L., Multimessenger parameter estimation of GW170817 *The European Physical Journal A* (2019), **55** 50
- [74] Kumar B. and Landry P., Inferring neutron star properties from GW170817 with universal relations *Phys. Rev. D* (2019), **99** 123026
- [75] Baiotti L., Gravitational waves from neutron star mergers and their relation to the nuclear equation of state, *Progress in Particle and Nuclear Physics* (2019), **109** 103714
- [76] Mazets E.P., Golenetskij S.V. and Guryan Y.A., Soft gamma-ray bursts from the source B1900+14, *Soviet Astronomy Letters* (1979), **5** 641
- [77] Mazets E.P. *et al.*, Observations of a flaring X-ray pulsar in Dorado, *Nature* (1979), **282** 587

Bibliography

- [78] Mazets E.P. and Golenetskij S.V., Recent results from the gamma-ray burst studies in the KONUS experiment, *Astrophysics and Space Science volume* (1981), **75** 47
- [79] Olausen S.A. and Kaspi V.M., THE MCGILL MAGNETAR CATALOG, *The Astrophysical Journal Supplement Series* (2014), **212** 6, and the **online catalog**: <http://www.physics.mcgill.ca/pulsar/magnetar/main.html>
- [80] Bilous A.V. *et al.*, A NICER View of PSR J0030+0451: Evidence for a Global-scale Multipolar Magnetic Field, *The Astrophysical Journal Letters* (2019) **887** L23
- [81] Fujisawa K. and Kisaka S., Magnetic field configurations of a magnetar throughout its interior and exterior – core, crust and magnetosphere, *Monthly Notices of the Royal Astronomical Society* (2014), **445** 2777
- [82] Krüger T., Tews I., Hebeler K. and Schwenk A., Neutron matter from chiral effective field theory interactions, *Phys. Rev. C* (2013), **88** 025802
- [83] Stoks V.G.J., Klomp R.A.M., Rentmeester M.C.M., and de Swart J.J., Partial-wave analysis of all nucleon-nucleon scattering data below 350 MeV, *Phys. Rev. C* (1993), **48** 792
- [84] Sarsa A., Fantoni S., Schmidt K.E. and Pederiva F., Neutron matter at zero temperature with an auxiliary field diffusion Monte Carlo method, *Phys. Rev. C* (2003), **68** 024308
- [85] Fantoni S., Gandolfi S., Pederiva and F. Schmidt K. E., QUANTUM MONTE CARLO CALCULATIONS FOR NUCLEI AND NUCLEAR MATTER, in Boronat J. Astrakharchik G. Mazzanti T., eds, World Scientific Series on Advances in Quantum Many-Body Theory, Vol. 11, Recent Progress in Many-Body Theories (2007) World Scientific, Singapore, p. 23
- [86] Gandolfi S., The Auxiliary Field Diffusion Monte Carlo Method for Nuclear Physics and Nuclear Astrophysics, *Ph.D. Thesis* (2007), arXiv:0712.1364
- [87] Carlson J. *et al.*, Quantum Monte Carlo methods for nuclear physics, *Rev. Mod. Phys.* (2015), **87** 1067

- [88] Stoks V., Timmermans R. and de Swart J.J., Pion-nucleon coupling constant, *Phys. Rev. C* (1993), **47** 512
- [89] Gandolfi S., Carlson J. and Pieper S. C., Cold Neutrons Trapped in External Fields, *Phys. Rev. Lett.* (2011), **106** 012501
- [90] Gandolfi S. *et al.*, Quantum Monte Carlo calculation of the equation of state of neutron matter, *Phys. Rev. C* (2009), **79** 054005
- [91] Pieper S.C., Pandharipande V.R., Wiringa R.B. and Carlson J., Realistic models of pion-exchange three-nucleon interactions, *Phys. Rev. C* (2001), **64** 014001
- [92] Maris P. *et al.*, Properties of trapped neutrons interacting with realistic nuclear Hamiltonians, *Phys. Rev. C* (2013), **87** 054318
- [93] Maris P. *et al.*, Quantum Monte Carlo Calculations of $A \leq 6$ Nuclei, *Phys. Rev. Lett.* (1995), **74** 4396
- [94] Carlson J., Pandharipande V.R. and Wiringa R.B., Three-nucleon interaction in 3-, 4- and ∞ -body systems, *Nuclear Physics A* (1983), **401** 59
- [95] Fujita J. and Miyazawa H., Pion Theory of Three-Body Forces, *Progress of Theoretical Physics* (2015), **17** 360
- [96] Hebeler K., Holt J.D., Menéndez J. and Schwenk A., Nuclear Forces and Their Impact on Neutron-Rich Nuclei and Neutron-Rich Matter, *Annual Review of Nuclear and Particle Science* (2015), **65** 457
- [97] Bernard V., Kaiser N. and Meissner U.-G., CHIRAL DYNAMICS IN NUCLEONS AND NUCLEI, *International Journal of Modern Physics E* (1995), **04** 193
- [98] Weinberg S., Effective chiral lagrangians for nucleon-pion interactions and nuclear forces, *Nuclear Physics B* (1991), **363** 3
- [99] Tews I., Carlson J., Gandolfi S. and Reddy S., Constraining the Speed of Sound inside Neutron Stars with Chiral Effective Field Theory Interactions and Observations, *The Astrophysical Journal* (2018), **860** 062501

Bibliography

- [100] Lipparini E. and Pederiva F., Asymmetric nuclear matter studied by time-dependent local isospin density approximation, *Phys. Rev. C* (2013), **88** 024318
- [101] Lipparini E. and Pederiva F., Transverse isospin response function of asymmetric nuclear matter from a local isospin density functional, *Phys. Rev. C* (2016), **94** 024323
- [102] Lipparini E., *Modern Many-Particle Physics*, *World Scientific* (2008), **doi:** 10.1142/6551
- [103] Lomnitz-Adler J., Pandharipande V.R. and Smith R.A., Monte Carlo calculations of triton and ^4He nuclei with the Reid potential, *Nuclear Physics A* (1981) **361** 399
- [104] Kalos M.H., Monte Carlo Calculations of the Ground State of Three- and Four-Body Nuclei, *Phys. Rev.* (1962) **128** 1791
- [105] Schmidt K. and Fantoni S., A quantum Monte Carlo method for nucleon systems., *Physics Letters B* (1999) **446** 99
- [106] Metropolis N. *et al.*, Equation of State Calculations by Fast Computing Machines, *The Journal of Chemical Physics* (1953), **21**, 1087
- [107] Trotter H.F., On the product of semi-groups of operators, *Proceedings of the American Mathematical Society* (1959), **10**, 54
- [108] Lonardonì D. *et al.* Auxiliary field diffusion Monte Carlo calculations of light and medium-mass nuclei with local chiral interactions, *Phys. Rev. C* (2018), **97** 044318
- [109] Zhang S. and Krakauer H., Quantum Monte Carlo Method using Phase-Free Random Walks with Slater Determinants, *Phys. Rev. Lett.* (2003), **90** 136401
- [110] Piarulli M. *et al.*, Benchmark calculations of pure neutron matter with realistic nucleon-nucleon interactions, (2019), arXiv:1908.04426

- [111] Gandolfi S. *et al.*, The equation of state of neutron matter, symmetry energy and neutron star structure, *The European Physical Journal A* (2014), **50** 10
- [112] Lin C., Zong F.H. and Ceperley D.M., Twist-averaged boundary conditions in continuum quantum Monte Carlo algorithms, *Phys. Rev. E* (2001), **64** 016702
- [113] Rajagopal A. K., Linear-response functions in spin-density-functional theory, *Phys. Rev. B* (1978), **17** 2980
- [114] Lipparini E. and Serra L., Spin-wave excitations in quantum dots *Phys. Rev. B* (1998), **57** R6830
- [115] Lipparini E., Barranco M., Emperador A., Pi M. and Serra L., Transverse dipole spin modes in quantum dots, *Phys. Rev. B* (1999), **60** 8734
- [116] Epelbaum E., Krebs H. and Meissner U.-G., Improved chiral nucleon-nucleon potential up to next-to-next-to-next-to-leading order, *The European Physical Journal A* (2015), **51** 53
- [117] Riz L., Gandolfi S. and Pederiva F., Spin response and neutrino mean free path in neutron matter *Journal of Physics G: Nuclear and Particle Physics* (2020) **47** 045106
- [118] Ceperley D.M. and Alder B.J., Ground State of the Electron Gas by a Stochastic Method, *Phys. Rev. Lett.* (1980), **45** 566
- [119] Zong F.H., Ceperley D.M., Moroni S. and Fantoni S. The polarization energy of normal liquid ^3He , *Molecular Physics* (2003), **101** 1705
- [120] Krüger T., Hebeler K. and Schwenk A. To which densities is spin-polarized neutron matter a weakly interacting Fermi gas?, *Phys. Lett. B* (2015), **744** 18
- [121] Bombaci I. *et al.* Microscopic calculations of spin polarized neutron matter at finite temperature *Phys. Lett. B* (2006), **632** 638
- [122] Vidaña I., Polls A. and Durant V., Role of correlations in spin-polarized neutron matter *Phys. Rev. C* (2016), **94** 054006

Bibliography

- [123] Hohenberg P. and Kohn W., Inhomogeneous Electron Gas, *Phys. Rev.* (1964), **136** B864
- [124] Lipparini E., Stringari S. and Takayanagi K., Density dependence of the plasmon dispersion in alkali metals, *J. Phys.: Condensed. Matter* (1994), **6** 2025
- [125] Buraczynski M., Ismail N. and Gezerlis A., Nonperturbative Extraction of the Effective Mass in Neutron Matter, *Phys. Rev. Lett.* (2019), **122** 152701
- [126] Hannestad S. and Raffelt G., Supernova Neutrino Opacity from Nucleon-Nucleon Bremsstrahlung and Related Processes, *The Astrophysical Journal* (1998), **507** 339
- [127] Lykasow G. I., Olsson E. and Pethick C. J., Long-wavelength spin- and spin-isospin correlations in nucleon matter, *Phys. Rev. C* (2005), 025805
- [128] Reddy S., Prakash M. and Lattimer J. M. Neutrino interactions in hot and dense matter, *Phys. Rev. D* (1998), **58** 013009
- [129] Margueron J., Navarro J., Van Giai N. and Jiang W., Neutrino Propagation in Neutron Matter and the Nuclear Equation of State, *The Nuclear Many-Body Problem 2001* (2002), **53** 329
- [130] Iwamoto N. and Pethick C.J., Effects of nucleon-nucleon interactions on scattering of neutrinos in neutron matter, *Phys. Rev. D* (1982), **25** 313
- [131] Cowell S. and Pandharipande V.R., Neutrino mean free paths in cold symmetric nuclear matter, *Phys. Rev. C* (2004), **70** 035801
- [132] Fantoni S., Sarsa A. and Schmidt K.E., Spin Susceptibility of Neutron Matter at Zero Temperature, *Phys. Rev. Lett.* (2001), **87** 181101
- [133] Lovato A., Benhar O., Gandolfi S. and Losa C., Neutral-current interactions of low-energy neutrinos in dense neutron matter, *Phys. Rev. C* (2014), **89** 025804

- [134] Pastore A. *et al.*, Nuclear response for the Skyrme effective interaction with zero-range tensor terms. III. Neutron matter and neutrino propagation, *Phys. Rev. C* (2012), **86** 044308
- [135] Reddy S., Prakash M., Lattimer J.M. and Pons J.A., Effects of strong and electromagnetic correlations on neutrino interactions in dense matter, *Phys. Rev. C* (1999), **59** 2888
- [136] Ejiri H., Nuclear spin isospin responses for low-energy neutrinos, *Physics Reports* (2000), **338** 265
- [137] Aguirre R., Bauer E. and Vidaña I., Neutron matter under strong magnetic fields: A comparison of models, *Phys. Rev. C* (2014) **89** 035809
- [138] Benhar O., Cipollone A. and Loreti A., Weak response of neutron matter at low momentum transfer, *Phys. Rev. C* (2013), **87** 014601
- [139] Clark J.W., Heintzmann H., Hillebrandt W. and Grewing M., Nuclear Forces, Compressibility of Neutron Matter and the Maximum Mass of Neutron Stars, *Astrophysical Letters* (1972), **10** 21
- [140] Vidaña I. and Bombaci I. Equation of state and magnetic susceptibility of spin polarized isospin asymmetric nuclear matter, *Phys. Rev. C* (2002) **66** 045801
- [141] Vidaña I., Polls A. and Ramos A. Spin polarized neutron matter and magnetic susceptibility within the Brueckner-Hartree-Fock approximation, *Phys. Rev. C* (2002) **65** 035804

ACKNOWLEDGMENTS

All that I have done in this thesis would not have been possible without the guidance of my advisor, Francesco Pederiva. He has been more than a simple advisor to me. He taught me a lot during these years with his amazing patience, kindness, and vast knowledge on different fields of physics. I will always be grateful to him for the time and the opportunities he has given me in the past years. I found in him a fantastic reference point both on a scientific and personal level.

I would also like to express a special thanks to Stefano Gandolfi. Since I was an undergraduate, he explained to me a lot about the AFDMC code. Francesco and Stefano allowed me to spend some time at LANL, where I had the occasion to work in an excellent scientific community. During my period at LANL, I had the chance to meet Joe Carlson and discuss with him part of my work. He gave me some new insights into my research and raised interesting remarks on the work I was doing. At LANL, I also started a collaboration with Diego Lonardonì on twist-averaged boundary conditions. I am grateful to him for the useful discussions and the hospitality he gave me when I was in Los Alamos and Santa Fe.

Francesco encouraged and allowed me to spend also some time at INT, during a Programme on QMC methods, at ANL, with the support of Alessandro Lovato, and even at LLNL, discovering a bit of the quantum computing world, with the support of Sofia Quaglioni. I am thankful to all the people I met there.

Among them, I need to mention Robert B. Wiringa and Malvin H. Kalos. Meeting and talking with these two incredible scientists has been a unique experience, and I am grateful to them for the time they spent with me. I also have to thank Eric T. Holland: he gave me the chance to visit the experimental setup of the quantum computer at LLNL. I will keep all these experiences in my head and my heart for the rest of my life.

Bibliography

During my time in Trento, I had the opportunity to talk with Kevin Schmidt. I want to thank him for the useful discussion on the twist-averaged boundary conditions and on the magnetic susceptibility in neutron matter.

Finally, I would like to thank the referees Omar Benhar and Sanjay Reddy, who carefully read my thesis and gave me useful suggestions that improved its final version.

RINGRAZIAMENTI

Vorrei concludere questa tesi con degli ulteriori ringraziamenti alle persone care della mia vita.

Al termine di questo percorso vorrei ringraziare la mia famiglia che mi ha sempre sostenuto in questo percorso del dottorato. Mi sono stati vicini, mi hanno sostenuto e mi hanno trasmesso i loro valori e i loro ideali. Un grazie particolare va quindi a mia mamma Maria, mio papà Carlo e alle mie sorelle Chiara e Francesca che hanno condiviso con me questo periodo della mia vita.

Durante il dottorato una persona speciale è entrata a far parte della mia vita: la mia ragazza, Jenny. Con la sua curiosità per quello che stavo studiando e la sua voglia di capire mi ha spronato a cercare di spiegarle quello che stavo facendo. La ringrazio di cuore perché mi è sempre stata vicina e nelle difficoltà di questa esperienza mi ha sempre sostenuto e incoraggiato.

Un altro ringraziamento va all'Istituto Salesiano Maria Ausiliatrice di Trento, che in questi anni mi ha accolto e che è diventato la mia casa. Ringrazio i responsabili don Carlo e don Eugenio e tutti i ragazzi che in questi anni ho conosciuto perché mi hanno reso la persona che sono oggi. In particolare ringrazio i miei amici più cari per esserci sempre: Matteo, Emanuele e Marco.

Per concludere vorrei lasciare anche un pensiero ai miei compagni di corso della magistrale, specialmente a Lorenzo, Ruggero, Mattia, Mirko e Fabrizio. È anche grazie a loro che ho scelto di proseguire gli studi con un dottorato e sono felice di aver fatto questa scelta.

Inoltre vorrei ringraziare Lorenzo e Lucas per lo scambio di idee e discussioni su QMC e fisica nucleare. Oltre all'ambito scientifico, ringrazio Lorenzo per avermi guidato alla scoperta di Santa Fe durante la mia permanenza al LANL e Lucas che mi ha ospitato per un weekend a Phoenix.

Infine vorrei ringraziare le segretarie del dipartimento di Fisica per la loro pa-

Bibliography

zienza e il loro lavoro, spesso invisibile, ma indispensabile.

Ringrazio tutti, anche chi non è stato nominato esplicitamente, per aver creduto in me e avermi supportato durante il dottorato.